Interaction of the Wake and Boundary Layer in a Multielement Airfoil System

by

Ernest Spevak

B.S. Aeronautical and Astronautical Engineering
University of Illinois at Urbana-Champaign, 1994

Submitted to the Department of Aeronautics and Astronautics
in partial fulfillment of the requirements for the degree of

Master of Science in Aeronautics and Astronautics

at the

MASSACHUSETTS INSTITUTE OF TECHNOLOGY

February 1997

Author .....
Department of Aeronautics and Astronautics
September 10, 1996

Certified by .....
Kenneth S. Breuer
Associate Professor
Thesis Supervisor

Certified by .....
Mark Drela
Associate Professor
Thesis Supervisor

Accepted by .....
Professor Jaime Perarie
Chairman, Department Graduate Committee

Interaction of the Wake and Boundary Layer in a Multielement Airfoil System

by

Ernest Spevak

Submitted to the Department of Aeronautics and Astronautics
on September 10, 1996, in partial fulfillment of the
requirements for the degree of
Master of Science in Aeronautics and Astronautics

Abstract

The interaction between the wake of a leading airfoil element and the boundary layer of a trailing airfoil element is investigated for improvement of computational fluid dynamics models. Velocity profiles are presented and discussed for seven streamwise locations along the upper surface of a multi-element airfoil system at two Reynolds numbers ($\Re = 1.4 \times 10^5$ and $\Re = 1.8 \times 10^5$) using a newly developed multi-element airfoil testing rig in a low-turbulence wind tunnel. Preliminary measurements of mean and fluctuating components of streamwise and normal velocities and the Reynolds shear stress compare well qualitatively with general streamline curvature theory as well as with several previous experimental studies. Comparisons to MSES, a viscous-inviscid, design/analysis code, are also encouraging though suggest several shortcomings in the current CFD model. Reynolds shear stress coefficient approximations at transition locations appear to be overestimated while the degree of wake asymmetry is not adequately represented. The presence of low-Reynolds number effects is also discussed. Suggestions for experimental database construction are presented with improved data collection quality and efficiency at additional testing conditions.

Thesis Supervisor: Kenneth S. Breuer
Title: Associate Professor

Thesis Supervisor: Mark Drela
Title: Associate Professor

Acknowledgments

I consider myself fortunate to have been able to participate in the research presented in this thesis. I am grateful to the Department of the Army Research Office and their participation in the NDSEG Fellowship Program without which I may not have had this invaluable experience.

I would also like to thank Professors Kenny Breuer and Mark Drela for allowing me the opportunity to pursue this research avenue. I truly appreciate their helpful insights and their refrain from several much deserved "I-told-you-so" 's. Their exceptional guidance allowed me to learn from my own mistakes while not being discouraged by them.

Finally, I would like to thank all of my family and friends for reminding me of who I am. To all of my friends in FDRL, SSL, and the lab formerly known as CASL: thank you for not only providing me with the necessary distractions to maintain my sanity and to have a good time doing it but also for wonderful insights into the aerospace field. A special thanks goes out to my roommates, Lou and Randy, without whom my time here would not have been nearly as enjoyable. And to my friends and family back home: thank you for staying close during my extended absences. I feel blessed for knowing all of you.

Contents

List of Tables

List of Figures

Chapter 1

Introduction

1.1 Motivation

The performance of modern transport aircraft at takeoff and landing conditions depends heavily on the high-lift capability of multi-element airfoil systems. In the 20 years since A.M.O. Smith's Wright Brothers Lecture[21] considerable progress has been made in the study and computational analysis of high-lift aerodynamics and airfoil systems. However, the design of multi-element airfoil systems still relies on extensive wind tunnel testing even though single element airfoil designs are primarily created using computational methods and often times only validated in the wind tunnel[7]. This discrepancy in design methodology is caused by the much more complicated viscous flow physics involved in the multi-element cases suggesting the continuing development of computational fluid dynamics (CFD) with increased attention to fundamental fluid mechanics[16].

Flow phenomena such as streamline curvature, non-equilibrium turbulence, shear layer interactions, and asymmetric wakes occurring in multi-element airfoil systems are currently neither well modeled for computational solution[7] nor fully understood. This lack of proper modeling is due in part to limited experimental data detailing these complex flow interactions[2]. The purpose of the current research is to provide a facility capable of producing the type of data required for a comprehensive database for the modeling of such flow phenomena as well as to obtain preliminary data on the

interaction of the wake from a leading element and the boundary layer of the trailing element in a two-element airfoil system.

1.2 Previous Investigations

Before proceeding to a discussion of the present work, a brief summary of the theory applicable to qualitative analysis of streamline curvature which leads to the observed wake asymmetry is included. Also provided is a brief survey of historically significant experiments as well as present and ongoing studies.

1.2.1 Theoretical Contributions

The primary qualitative conclusion of streamline curvature theory is the destabilizing (greater turbulence producing) nature of concave curvature and the stabilizing (lesser turbulence producing) nature of convex curvature. This conclusion comes from an inviscid analysis of curved flows. Since curved flow may be considered rotation about the local center of curvature, we can apply Rayleigh's circulation criterion as presented by Drazin and Reid[6]. For stability, the Rayleigh discriminant, Φ,

$$\Phi \equiv \frac{1}{r^3}\frac{d}{dr}(rU)^2 \tag{1.1}$$

$$= 2\left[\left(\frac{U}{r}\right)^2 + \frac{U}{r}\frac{dU}{dr}\right] \tag{1.2}$$

must be greater than zero everywhere. Since r and U denote the radial distance measured from the center of curvature and the velocity magnitude, respectively, and since both are positive, dU/dr must also be positive for stability implying that the flow velocity must increase with increasing distance from the center of curvature. Therefore, convex curvature is stabilizing while concave curvature is destabilizing.

Bradshaw[4] contended that the effects of curvature may be modeled as an extra rate of strain e on the fluid in addition to the mean shear. This additional strain rate would then change the characteristic turbulence mixing length by a factor F. Approximating streamwise curvature as $-U/R$, Bradshaw maintained that the turbulent

dissipation length change could be approximated by:

$$\frac{L}{L_o} \approx F = 1 + \alpha \frac{\left(\frac{U}{R}\right)}{\left(\frac{\partial U}{\partial y}\right)} \tag{1.3}$$

where $\alpha \approx 14$ for mild convex curvature and $\alpha \approx -9$ for mild concave curvature. Equation 1.3 not only resembles the Monin-Oboukov formula but it also hints at Prandtl's mixing length concepts, a detailed discussion of which may be found in Schlichting[20]. As will be apparent in Section 1.2.2, however, simply adjusting the mixing length model does not account for all of the phenomena involved in streamline curvature flow fields. Also, the above theory assumed local equilibrium for the turbulent energy equation which is not applicable due to the presence of non-equilibrium turbulence in the multi-element airfoil flows.

1.2.2 Previous and Current Experiments

Several historically significant experimental studies on curved walls are applicable in the present context of flow with streamline curvature. The work of both Muck et al.[17] and of Gillis and Johnston[10] on convex boundary layer flow support the notion of increased stability and decreasing turbulence intensities with convex streamline curvature. The work of Hoffmann et al.[13] on concave boundary layer flow, however, suggests not only an increase in turbulent intensity but also a flow re-organization in concave streamwise curvature cases. The resulting re-organized flow contains coherent structures resembling Görtler vortices but in turbulent flow. This re-organization implies not only that Bradshaw's simple mixing length adjustment model is not adequate but that concavely curved flows tend to react in longer time scales than convex flows since scaling of flow parameters is not the only phenomenon present. Also, the above experiments suggest that concave curvature flows depend heavily on the upstream turbulence history while the convex curvature flow exhibits asymptotic behavior as data sets at various flow conditions appear to collapse onto a single curve during flat plate redevelopment. The experimental works on boundary layer flows imply that Bradshaw's theory should only be used for qualitative analysis rather than anything

quantitative. This conclusion, in turn, implies that empirical relationships obtained from a comprehensive database is likely the best alternative for CFD applications.

Several experiments have been performed or are currently being performed in the study of the complex physics of mutli-element airfoil flows. Agoropoulos and Squire[3] examined two-dimensional turbulent wakes from a leading edge slat mixing with the boundary layer of the main airfoil element. The slat – main element combination was chosen because it typically exhibits stronger wake – boundary layer interactions that main element – flap configurations[3]. At approximately the same time, Ramjee et al.[19] examined the development of the wake of a single-element airfoil in a curved duct as an approximation of the imposed streamline curvature due to a second airfoil element. Also at approximately the same time, Adair and Horne[2] studied the shear layer interaction of a main element – flap configuration. These three experimental studies along with Weygandt and Mehta's [23] examination of initial condition effects on curved wake development may be used to obtain an overall picture of wake – boundary layer interaction. The general case of trailing edge flow such as the study of Absil and Passchier[1] may also be useful in understanding the near-wake flow field.

Two high-lift studies of note currently being performed (both at realistic Reynolds numbers) include the work of Sullivan et al.[22] and Nelson et al.[18]. While Sullivan et al. is focusing on a main element – flap configuration, Nelson et al. is examining the leading edge slat – main element interaction.

1.3 Present Work

The present research involves the design, development and preliminary testing of a multi-element airfoil wind tunnel testing system. The testing system employs load cells for lift measurement, wake profiles for drag measurement and a cross-wire hot-wire probe for shear layer velocity profile measurement along both element surfaces. Experiments are conducted in the Low-Turbulence Wind Tunnel facility in the Department of Aeronautics and Astronautics at the Massachusetts Institute of Technology.

After the experimental equipment and techniques are described in detail, preliminary results of lift and drag and of shear layer velocity profiles at seven streamwise locations are presented and compared to the computational predictions of MSES. Due to the limited flow Reynolds numbers ($\Re < 2 \times 10^5$) and the dearth of experimental data, clear suggestions for computational model modifications cannot be made although several interesting observations are possible. It appears that the computational model has difficulty in predicting the Reynolds shear stress coefficient immediately at the transition location along the top surface of the leading airfoil element. Also, the model does not appear to adequately represent the wake asymmetry present in the experimental flow. Since the present research has only produced preliminary results, the study concludes with suggestions of future work and experimental equipment and method modifications for data improvement and database expansion.

Chapter 2

Experimental Equipment and Procedures

The experiments performed to support this research relied heavily on the Low Turbulence Wind Tunnel and its many supporting systems, both pre-existing and newly created, in the Department of Aeronautics and Astronautics at the Massachusetts Institute of Technology. Likewise, several experimental methods, both pre-existing and newly created, were implemented in the execution of the experiments. This chapter focuses on the experimental setup (hardware) involved in the research including the wind tunnel itself, the multi-element airfoil model, the model support systems, and the crosswire velocity measurement system. Also, calibration techniques for the systems and experimental procedures are presented.

2.1 Low Turbulence Wind Tunnel

All of the experiments discussed in this work were performed in an open circuit, low turbulence wind tunnel shown in Figure 2-1 [11] and described in greater detail by M.E. Grimaldi [11]. The wind tunnel consists of a 16 : 1 contraction section employing a $0.10\,m$ honeycomb and four screens to reduce streamwise freestream turbulence to 0.08% at $12.5\,m/s$ [11]. The contraction section is followed by a $0.61\,m \times 0.91\,m \times 3.66\,m$ test section with three vertical doors along each side. The wind tunnel motor

is controlled by the system described in Section 2.2 and may be set according to nominal velocities which may then be converted to freestream velocities using the method described in Appendix B.

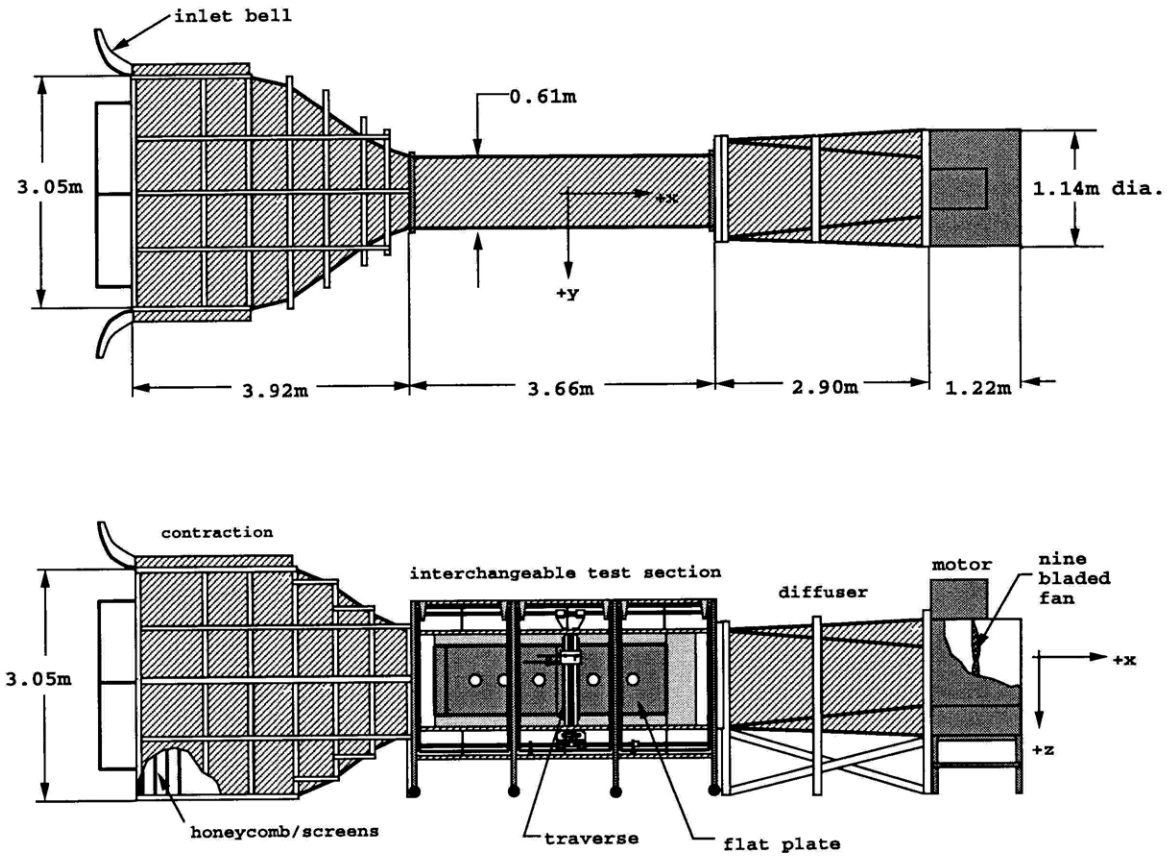

Figure 2-1: Low turbulence wind tunnel. Department of Aeronautics and Astronautics, M.I.T. Figure reproduced from Grimaldi [11].

For the present experiments, the flat plate labeled in Figure 2-1 was removed and the multi-element airfoil system installed through the door farthest upstream to take advantage of a thin boundary layer at the beginning of the test section. Since the airfoil is mounted upside down and through the side of the wind tunnel, the U- and V-velocities are actually directed along the X- and Z-axes as labeled in the diagram, respectively.

Flow measurement instrumentation is placed in the desired position by a programmable traverse mechanism driven by stepper motors. The X and Z traverse axes are used to position the probe with $0.007\,mm$ resolution while the rotation system

described in Section 2.6 is used to change the relative angle of the probe with respect to the horizontal.

2.2 Data Acquisition

Experimental data was obtained by a 12-bit Analog-to-Digital (A/D) converter capable of digitizing up to 16 channels with a $0.0049\,V$ resolution. Four of these channels served as the input from the load measurement system as described in Section 2.5.2 while two channels served as the input from the custom built, constant temperature hot-wire anemometer used to measure flow velocities. The cross-wire probes used in the experiments are described in Section 2.6. Finally, one channel was used as the input from the Baratron used for measuring the difference in total and static pressures as given by the pitot probe.

The data acquisition system was controlled using a 486 personal computer running programs written in C through a user interface with Matlab. The data reduction and plotting, meanwhile, was performed in the Matlab environment both on the PC and on Unix workstations.

2.3 Computational Fluid Dynamics Software

In the present research, comparisons of the experimental data with CFD models are made using version 2.8 of the MSES viscous-inviscid, design/analysis code which is described in greater detail by M. Drela in References [9], [7], and [8]. The code separates the flow into inviscid regions and viscous regions which are fully coupled through the displacement thickness. The inviscid portions are solved using the steady Euler equations in integral form to represent the flow while "a compressible lag-dissipation integral method is used to represent the boundary layer and wakes."[9] MSES has traditionally produced results in excellent agreement with previous experimental data.

The inviscid regions of the flow are modeled using Euler equations "discretized in conservation form on an intrinsic grid in which one family of grid lines corresponds

to streamlines."[9] To account for the viscous layers in the inviscid flow solution, the surface streamlines are displaced normal to the surface by the displacement thickness. The boundary layer formulation is based on a two-equation integral model with dissipation closure while a spatial amplification (e^N) model is used for transition prediction and a lag equation is used to account for the delayed response of turbulent stresses to changing flow conditions. (The calculations discussed in the present work were performed with $N = 10$.) For the multi-element airfoils, the boundary layer formulation is extended to a multi-deck integral form with terms to account for asymmetric wakes [7].

A global, Newton method is used to solve the fully coupled non-linear system. This quadratic convergence of this method allows for efficient parameter sweeps since the good first guess is obtained from the previous solution point. Although MSES was only used in analysis mode in the present research, its Newton solution method is also extremely useful in the design and optimization of multi-element airfoils [8].

2.4 The Multi-Element Airfoil

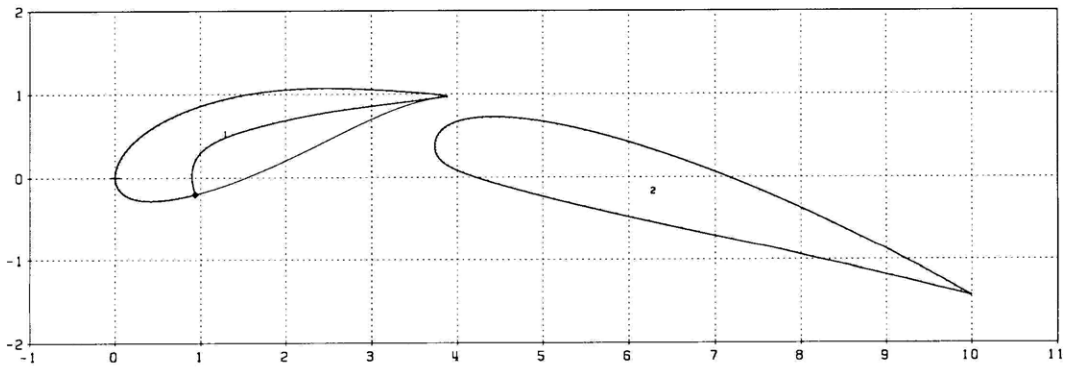

Figure 2-2: Multi-element airfoil plot (dimensions in inches).

The multi-element airfoil used in these experiments is shown in the scale plot in Figure 2-2. The actual airfoil elements are numerically machined from 6061 aluminum and have a total chord, c, of $10\,in$ and a span of $20\,in$ when fixed into the relative position for this experiment. The airfoil dimensions are summarized in Table 2.1 and the coordinates of the airfoil elements are listed in Appendix A as fractions of chord.

span	20.0 in	508 mm
element #1 chord	4.10 in	104 mm
element #2 chord	6.35 in	161 mm
gap	0.31 in	7.9 mm
total reference chord, c	10.0 in	254 mm
total reference area, S	200 in^2	0.129 m^2

Table 2.1: Airfoil Data.

The main airfoil element also has a 0.5 in hole located approximately 1.25 in from its leading edge with three set-screws along the length of the span for mounting to the support system discussed in coming sections. Also, the configuration shown in Figure 2-2 is used as the baseline relative to which the angle of attack, α, is measured.

The leading airfoil element is machined out of two pieces such that more realistic flows with flow separation in a typical cove may be studied when the lower portion is removed. Three flat-head screws are used to hold the two pieces of the leading element together and are covered with putty for smoother flow. Due to machining limitations the trailing edge of the lower element is cut short and the remainder is filled in with a spackling compound to create a smooth overall shape with the upper portion. The leading and trailing elements are fixed into relative position with the $\frac{1}{8}$ in thick aluminum end-plates which also serve to maintain a mostly 2-D flow over the airfoil. Two holes are drilled and tapped into each of the four spanwise ends of the upper portion of the leading element and the main element for the eight flat-head screws used to attach the airfoils to the end-plates through the eight matching holes in those end-plates. The multi-element airfoil system with the $\simeq 0.31$ in gap between airfoils clearly visible is shown in Figure 2-3 as would be seen from downstream of the suction side.

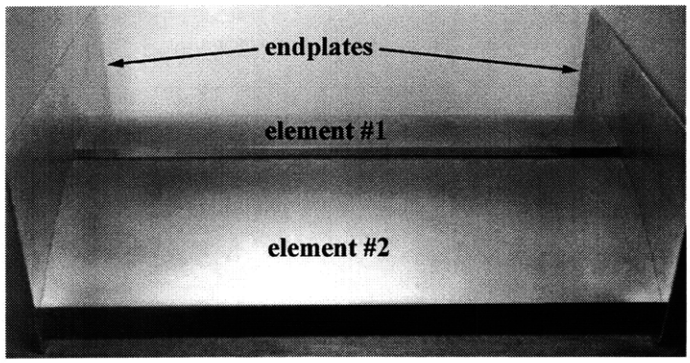

Figure 2-3: Airfoils fixed in relative position with end-plates.

2.5 System Support Structure

The multi-element airfoil system described in Section 2.4 is mounted onto a $0.5\,in$ diameter steel shaft which is cantilevered from the angle of attack adjustment system. This angle of attack adjustment system is then supported at six points by six load cells which allow for the transduction of forces and moments applied to the shaft by the combination of the airfoil itself and its aerodynamic loads as shown in the schematic in Figure 2-4 where lift and weight combination and the drag are as labelled while the moment due to the lift and weight is labelled as T_F. Each load cell is represented by its primary reaction load $(R_1, \ldots, R_6)$ as applied to the angle of attack adjustment system. The load cells themselves are supported by the steel channel section which is then attached to a five foot tall frame to locate the airfoil system in the center of the test section. The assembled support system is shown outside of the wind tunnel in Figure 2-5.

2.5.1 Angle of Attack Adjustment

Once the airfoil system is mounted on the steel shaft, the angle of attack may be adjusted using the system shown in Figure 2-6. The stepper motor drives a double-threaded worm which in turn drives the 72-tooth worm gear. The combination of the stepper motor's resolution of 1.8° per step and the worm gearing ratio of 36 to 1 provide a theoretical resolution of the angle of attack adjustment of 0.05°. The airfoil

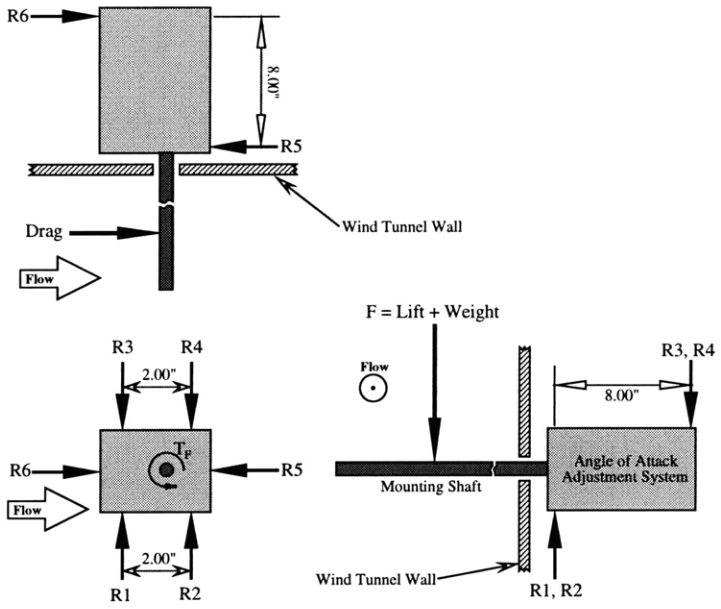

Figure 2-4: Schematic of load measurement system.

itself is supported in rotation solely by the stepper motor and exerts a considerable load on the motor shaft. Since the motor shaft can move along its axis about one millimeter, the angle of attack suffers from some hysteresis. In other words, the uncertainty created by the motion of the stepper motor shaft does not grant the investigator the freedom to simply set an angle of attack displacement and assume that it is correct. Instead, the angle must be verified at each setting with a digital level. The error in prescribed angular displacement and the measured displacement is typically less than the resolution of a standard digital level (0.1°) and still allows for testing within experimental parameters.

2.5.2 Load Measurement System

As previously mentioned, the angle of attack adjustment system is supported at six locations by the six load cells whose positioning allows the weight of the airfoil (mounted upside down), the lift and the drag to support the airfoil itself. The angle of attack adjustment assembly can be seen in place in the wind tunnel in Figure 2-7. The load cell positioning and the load measurement calibration procedure are discussed in the current section along with sample calibration results.

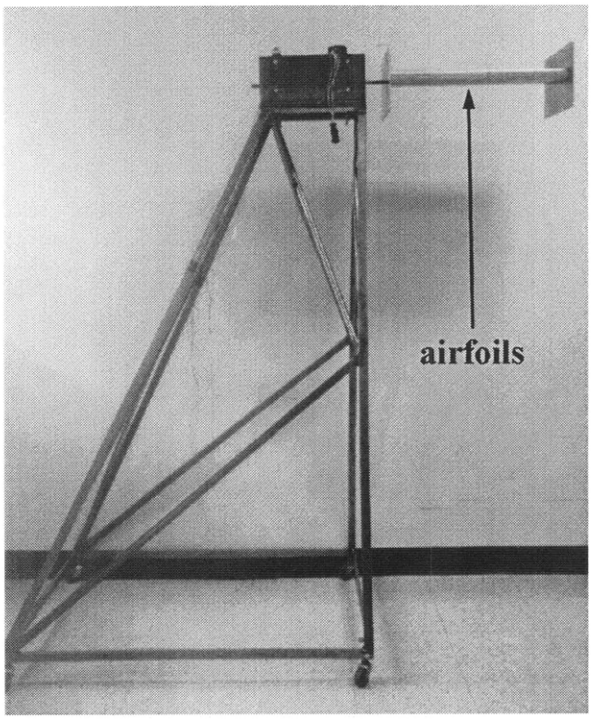

Figure 2-5: Complete airfoil support system shown outside of wind tunnel.

2.5.2.1 Physical Layout

The load cells are positioned such that the moments due to the weight of the airfoil and the lift and drag forces are balanced out. One pair of $50\,lb$ (Sensotec Model 13) load cells (R_1, R_2) is located below the end of the angle of attack system closer to the wind tunnel while another identical pair (R_3, R_4) is located $8\,in$ away from the first two load cells and above the farther end of the system as was shown in Figure 2-4. Similarly, single $10\,lb$ load cells (R_5, R_6) are mounted at the same spanwise locations but in the orientation required to balance the drag force moment. A view along the shaft axis is provided of the load measurement system in Figure 2-8 without the angle of attack adjustment system. (Note that the load cells toward the lower and the right portion of Figure 2-8 are closer to the wind tunnel than those at the top and left.) These load cells are mounted on aluminum blocks which may be moved in or out while support bolts hold the angle of attack system. This set-up gives the investigator the option of taking force data or simply allowing the support bolts to provide the necessary reaction loads.

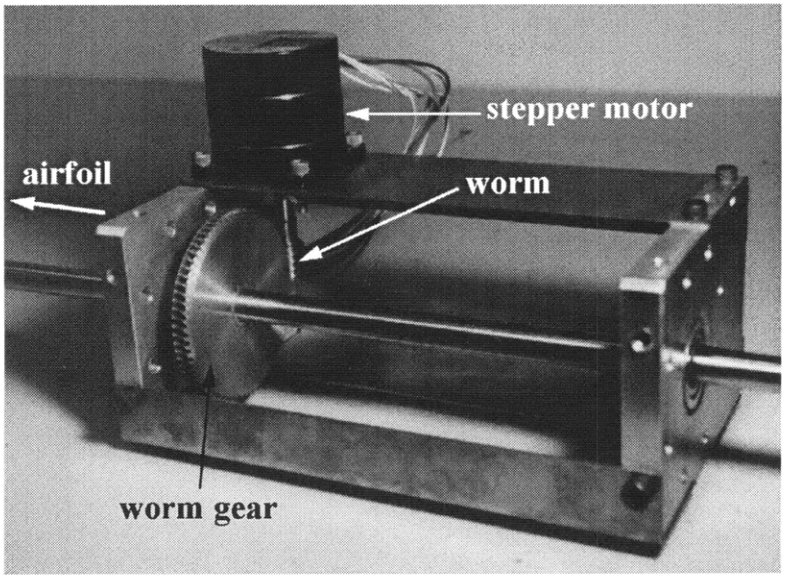

Figure 2-6: Angle of attack adjustment system with one corner support plate removed for better viewing.

The combination of the four $50\,lb$ load cells provides a measure of the lift, the moment due to lift about the shaft axis, and the spanwise location of the lift. Since the smaller capacity load cells are mounted in line with the shaft, those cells can only provide a measure of drag and of the spanwise location of that drag. However, if a conservative friction coefficient of 0.1 is assumed between the load cells and the angle of attack assembly, then the friction forces from the four vertically oriented load cells would be of the same order as the drag force itself. In other words, the interference due to the lift load cells would render the drag load cell signals extremely inaccurate. The drag, therefore, must be measured using a traditional velocity defect approach. Meanwhile, the effect of the drag load cells on the lift measurement is minimal since the drag itself is at least one order of magnitude smaller than the lift while the friction coefficient reduces its effect by another order of magnitude. The following sections will then on the measurement of the larger force quantities including the lift, its moment about the shaft axis, and its spanwise location.

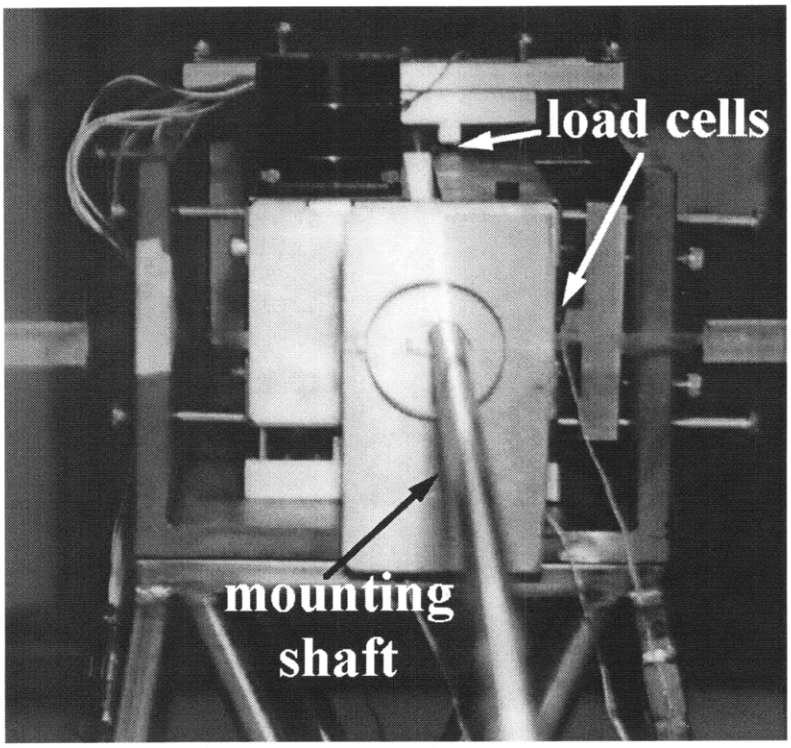

Figure 2-7: Angle of attack adjustment system supported by load cells in place in the wind tunnel.

2.5.2.2 Load Measurement System Calibration

Once the angle of attack assembly is in place and its position is adjusted to the liking of the investigator, the load cells are moved into light contact and the support bolts are moved away leaving only the load cells to provide the necessary reaction loads. In order to avoid overloading the strain gages of the load cells, the initial contact with the angle of attack adjustment system must be light. The calibration of the load measurement system may now be performed using the algorithm and procedure described below. This method allows the investigator to ignore the effect of the angle of attack system in the calibration procedure.

The combination of load cell and system characteristics allow for a calibration procedure based on tabulating and least squares fitting applied loads to the voltage data from each load cell. Since non-linearity of the load cells is only $\pm 0.25\%$ of full scale, the voltage response is considered linearly proportional to the force on the load cell.

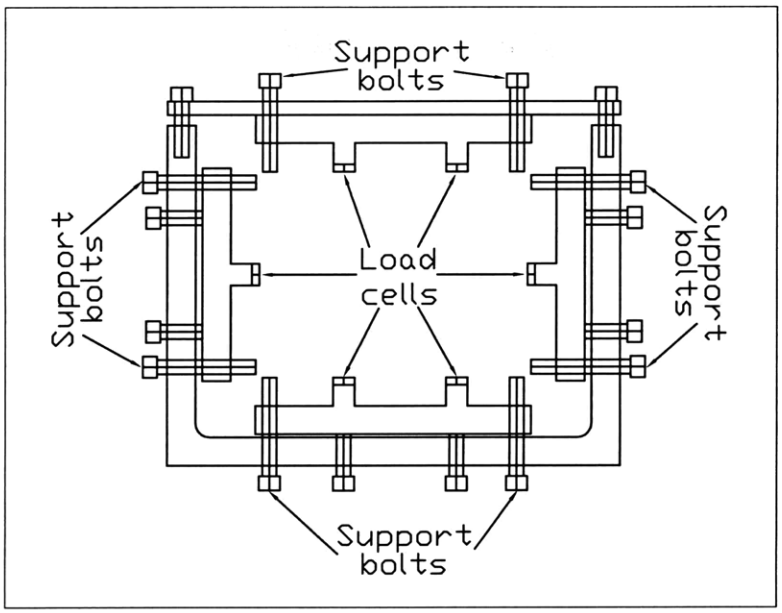

Figure 2-8: Schematic of load measurement system without angle of attack assembly.

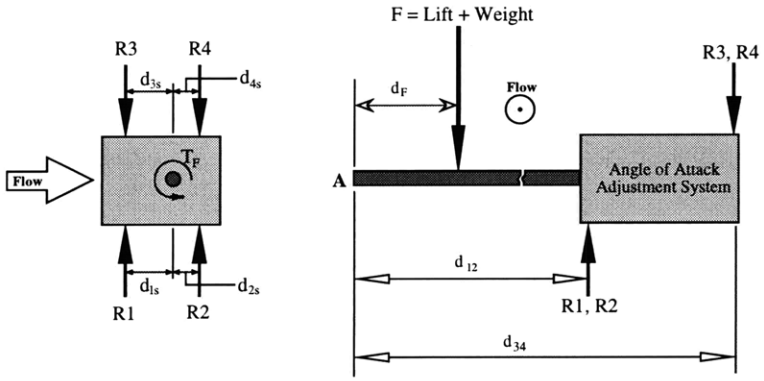

Figure 2-9: Schematic of load measurement system with calibration variables.

We may separate the force F on the mounting shaft into two components; one due to the angle of attack assembly, F_α, and one due to the applied load, F_{ap}, which is representative of the wing weight and lift combination:

$$F = F_\alpha + F_{ap} \tag{2.1}$$

Summing the forces in the vertical direction (as presented in Figure 2-9), we find that

$$F = R_1 + R_2 - R_3 - R_4 \tag{2.2}$$

Replacing the coefficients of each R_i with a_{i_F} and then substituting Equation 2.1 into Equation 2.2, we find that

$$F_\alpha + F_{ap} = \sum_{i=1}^{4} a_{i_F} R_i \tag{2.3}$$

$$F_{ap} = -F_\alpha + \sum_{i=1}^{4} a_{i_F} R_i \tag{2.4}$$

Since the signal conditioner for each load cell provides an output offset so as to fall into the $\pm 5V$ range of the A/D board, each R_i can also be separated into some constant (or gain), b_i, and voltage due to the total load, $E_{i_{ap}}$ (which is the difference between the measured voltage signal, E_i and the offset signal, E_{o_i}):

$$R_i = b_i E_{i_{ap}} \tag{2.5}$$

$$R_i = b_i (E_i - E_{o_i}) \tag{2.6}$$

Substituting Equation 2.6 for R_i into Equation 2.4 and grouping all of the constants into one summation and the variable voltages into another, we see that

$$F_{ap} = -F_\alpha + \sum_{i=1}^{4} a_{i_F} b_i (E_i - E_{o_E}) \tag{2.7}$$

$$= -F_\alpha - \sum_{i=1}^{4} a_{i_F} b_i E_{o_i} + \sum_{i=1}^{4} a_{i_F} b_i E_i \tag{2.8}$$

We can now combine the first two terms of Equation 2.8 into one constant, c_{0_F}, and the $a_{i_F} b_i$ portion of the second summation into one coefficient, c_{i_F}:

$$F_{ap} = c_{0_F} + \sum_{i=1}^{4} c_{i_F} E_i \tag{2.9}$$

$$= c_{0_F} + c_{1_F} E_1 + c_{2_F} E_2 + c_{3_F} E_3 + c_{4_F} E_4 \tag{2.10}$$

A similar derivation may be followed to determine the equations for the two moments. The only difference is that a_{i_M} and a_{i_T} represent the moment arms ("d" in the Figure 2-9) of the particular load cell forces and the proper sign of each load cell

moment. The derivation for M_{F_A} and T_F result in the following equations:

$$M_{F_A} = M_\alpha + M_{ap} \tag{2.11}$$

$$M_{ap} = c_{0_M} + c_{1_M}E_1 + c_{2_M}E_2 + c_{3_M}E_3 + c_{4_M}E_4 \tag{2.12}$$

$$T_F = T_\alpha + T_{ap} \tag{2.13}$$

$$T_{ap} = c_{0_T} + c_{1_T}E_1 + c_{2_T}E_2 + c_{3_T}E_3 + c_{4_T}E_4 \tag{2.14}$$

where the first terms of Equations 2.12 and 2.14 represent the cumulative effect of all constants just as in Equation 2.10 and M_{ap} and T_{ap} are the moments due to the applied loads only (i.e. excluding the effects of the angle of attack adjustment system). As an aside, M_{ap} may be used as a measure of the 2-dimensionality of the flow in the experiments since it is actually just the product of F_{ap} and its moment arm, d_{ap}. For a truly 2-D flow, d_{ap} should be approximately one half of the span of the airfoil.

We can now combine Equations 2.10, 2.12, and 2.14 into matrix form as shown:

$$\begin{Bmatrix} F_{ap} \\ M_{ap} \\ T_{ap} \end{Bmatrix} = \begin{bmatrix} c_{0_F} & c_{1_F} & c_{2_F} & c_{3_F} & c_{4_F} \\ c_{0_M} & c_{1_M} & c_{2_M} & c_{3_M} & c_{4_M} \\ c_{0_T} & c_{1_T} & c_{2_T} & c_{3_T} & c_{4_T} \end{bmatrix} \begin{Bmatrix} 1 \\ E_1 \\ E_2 \\ E_3 \\ E_4 \end{Bmatrix} \tag{2.15}$$

Since there are five calibration coefficients $(c_0, \ldots, c_4)$ for each of the three force and moments, at least 15 different calibration loading conditions should be included using the load cell calibration tool shown in Figure 2-10. These 15 loadings should allow the force and moments to vary independently of each other several times. The calibration tool shown allows the application of various loads at $1.0in$ intervals from the shaft centerline and at the user's choice of spanwise location providing the ability to vary each load independently.

Once the loads have been applied and the voltage signals recorded, the following matrix equation is constructed (with n being the total number of calibration loading

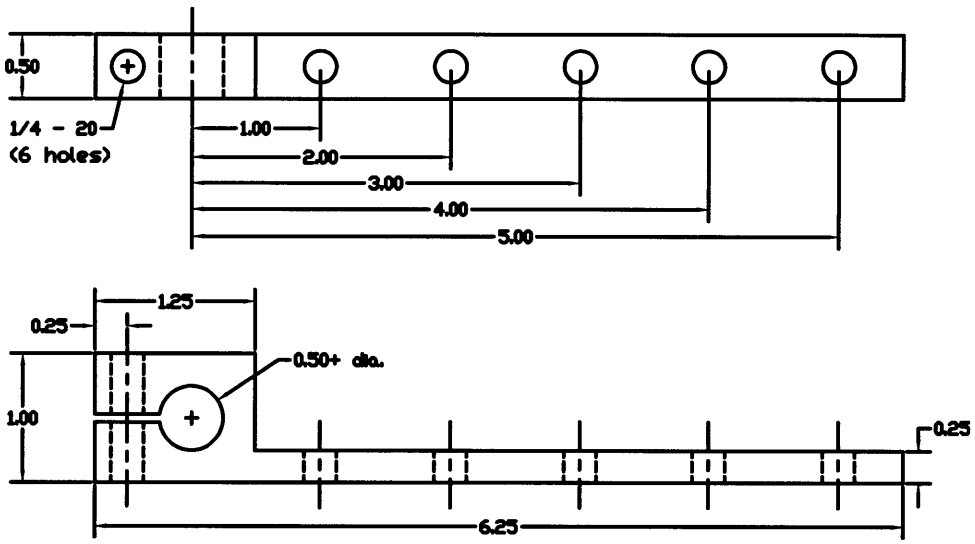

Figure 2-10: Load cell calibration tool.

conditions):

$$\begin{Bmatrix} F_{ap_1} & \cdots & F_{ap_n} \\ M_{ap_1} & \cdots & M_{ap_n} \\ T_{ap_1} & \cdots & T_{ap_n} \end{Bmatrix} = \begin{bmatrix} c_{0_F} & c_{1_F} & c_{2_F} & c_{3_F} & c_{4_F} \\ c_{0_M} & c_{1_M} & c_{2_M} & c_{3_M} & c_{4_M} \\ c_{0_T} & c_{1_T} & c_{2_T} & c_{3_T} & c_{4_T} \end{bmatrix} \begin{Bmatrix} 1 & \cdots & 1 \\ E_{1_1} & \cdots & E_{1_n} \\ E_{2_1} & \cdots & E_{2_n} \\ E_{3_1} & \cdots & E_{3_n} \\ E_{4_1} & \cdots & E_{4_n} \end{Bmatrix} \quad (2.16)$$

Equation 2.16 may now be solved (in the least squares sense) for the calibration coefficient matrix ($[c]$). Once this calibration matrix is determined, any set of measured voltage signals can be converted into the loading condition using Equation 2.15.

There are several guidelines which should be followed in order to obtain acceptable calibration and experimental data. Although the calibration matrix seems to be somewhat robust in terms of repeated airfoil installations and removals, a new calibration matrix should be created whenever the angle of attack assembly shifts position with respect to the load cells. In order to prevent such relative motion, the side support bolts may be brought into light contact with the angle of attach assembly while the spanwise location of the calibration tool is being changed. It is also recom-

mended that the minimum of 15 cases be attained by applying at least five loads at a minimum of 3 spanwise locations. Of those five loads, at least one should be applied at a different distance from the shaft centerline in order to vary independently the lift and moment about the shaft axis. Finally, it is important to calibrate the load cells in the predicted operating region of the airfoils to minimize any least squares fitting errors.

2.5.2.3 Sample Load Cell Calibration Results

After following the previously discussed calibration procedure, it is recommended that the calibration matrix be tested given several known loading conditions before proceeding with wind tunnel testing. Typically, the calibration tool is first used to provide the known loads to avoid unnecessary movement of the airfoil. If the calibration tool provides adequate predictions, the airfoil is mounted and loaded with known weights to simulate lift. The tare load is then subtracted from the total measured load to provide the net measured load. The results of such a test is presented in Figure 2-11 in which the weights were placed at approximately the middle of the span and one inch in front of the mounting shaft.

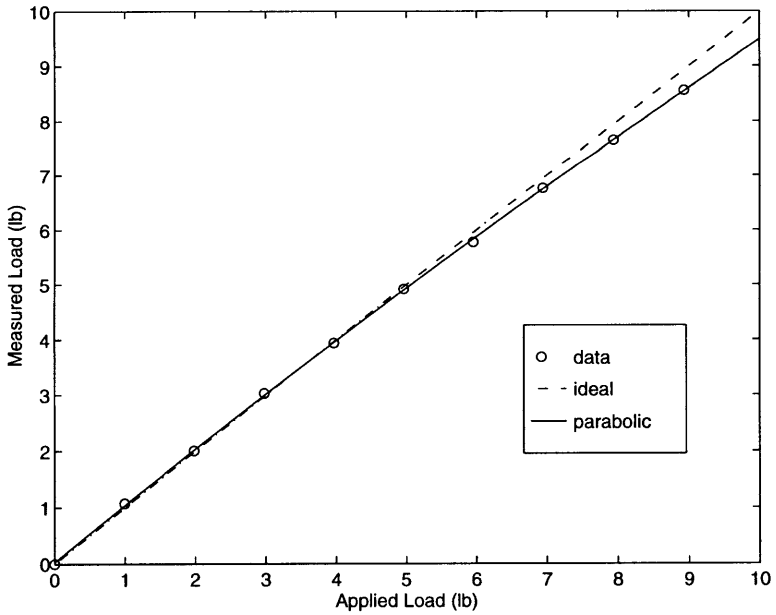

Figure 2-11: Plot of applied and measured loads (in addition to airfoil weight).

Figure 2-11 depicts not only the data points taken but also the ideal calibration curve and a parabolic fit to the data points to account for the tailing off at the higher loadings. It can be seen that the calibration shown is quite close to the ideal case as long as the load due to lift is kept to less than $6\,lb$. A relative error may be computed between the ideal case and the parabolic fit to obtain the curve shown in Figure 2-12. This relative error would then also represent the relative error between the measured and true C_L. There is clearly a range of lift loads that minimizes the load measurement errors. In typical calibration cases, lift loads between 1.4 and $7.5\,lb$ will keep the load measurement errors below 3%. Also shown in Figure 2-12 are the two testing conditions, $8.4\,m/s$ and $10.6\,m/s$, used in the wake–boundary layer profile measurements as discussed in Section 3.2.3 and their respective approximate relative errors in lift, 2.5% and 1.3%.

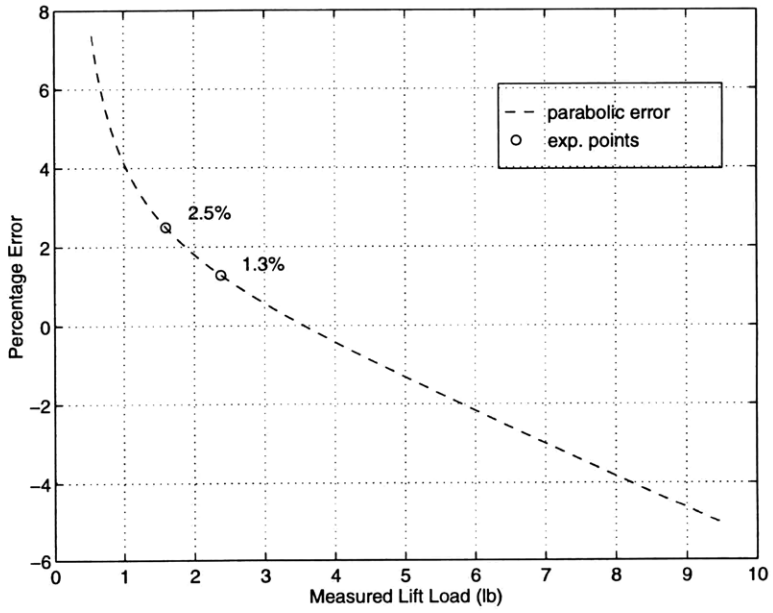

Figure 2-12: Plot of relative error in lift as a function of the load.

2.6 Cross-wire System

A cross-wire system was employed in order to measure the velocity quantities in both the streamwise and normal directions. The two velocity components of interest may be deduced by comparing the effect of convective cooling on each wire. Since the wires are at approximately 90° to each other, large variations in convective cooling occur depending on the relative angle of the flow to the wires. In order both to position the probe and to calibrate it, an assembly was constructed to rotate the probe about a distant pivot. However, through software the probe can be rotated about any point in space including the "x" itself. This section will then focus on the cross-wire system used to measure the mean and *rms* flow velocity quantities for each component as well as the Reynolds shear stress at each data point in each profile. After the physical system is described, a calibration procedure is presented along with some sample calibration results.

2.6.1 Physical Setup

2.6.1.1 The Cross-wire Probe

The cross-wire probe itself consists of two Platinum-10%Rhodium Wollaston-type wires attached between the ends of two pairs of steel broaches/prongs inserted through four holes in a ceramic cylinder. The two $2.54\,\mu m$ diameter wires are spot-welded to the $0.003\,in$ ends of prongs at a relative angle of 90° to each other. When viewed on end, the prongs appear to form the corners of a square box of $\sim 0.5\,mm$ sides while the wires appear to make an "x" when viewed from the side. The relative angle is produced by staggering one prong of each pair by $0.5\,mm$ along the probe axis with respect to the other prong. This places one wire at a $+45°$ and the other wire at $-45°$ with respect to the probe axis. In other words, the prongs at opposite corners of the box are at the same position along the probe axis. A diagram of the probe itself illustrating the wire/prong position is shown in Figure 2-13.

The cross-wire probe dimensions of importance are chosen so as to minimize errors in data caused by end conduction effects, lack of spatial resolution, and crosstalk

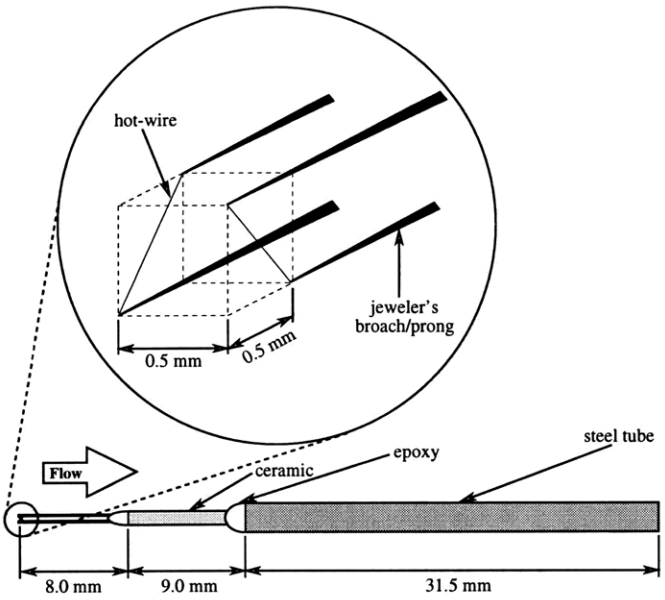

Figure 2-13: A scale diagram of the cross-wire probe.

between the two wires. The combination of wire length ($l \sim 0.7\,mm$), wire diameter ($d = 2.54\,\mu m$), and wire spacing ($\Delta z \sim 0.5\,mm$) along with a typical laboratory Kolmogorov microscale ($\eta \sim 0.2\,mm$) produce the following ratios:

$$l/d \approx 280 \tag{2.17}$$

$$l/\eta \approx 3.5 \tag{2.18}$$

$$\Delta z/\eta \approx 2.5 \tag{2.19}$$

which fall into the acceptable ranges ($l/d > 140$, $l/\eta < 5$, and $\Delta z/\eta < 3$) according to the recommendations of Browne et al. [5] to limit turbulence data errors to less than 4%.

2.6.1.2 The Probe Rotation System

After considering a several rotation system options including a flexible shaft assembly, it was determined that the present lead screw system provided the best compromise of the resolution, stiffness, and low flow profile. The cross-wire probe is rotated using a system consisting of a stepper motor, a lead screw, an aluminum block riding on

the lead screw, a rack, a pinion, and the boom which holds the probe itself in place. The system shown in the diagram in Figure 2-14 converts rotational motion of the stepper motor into translational motion of the aluminum block and the rack and then back into rotational motion of the pinion and the boom-probe assembly about the pivot marked with a "+" in the figure.

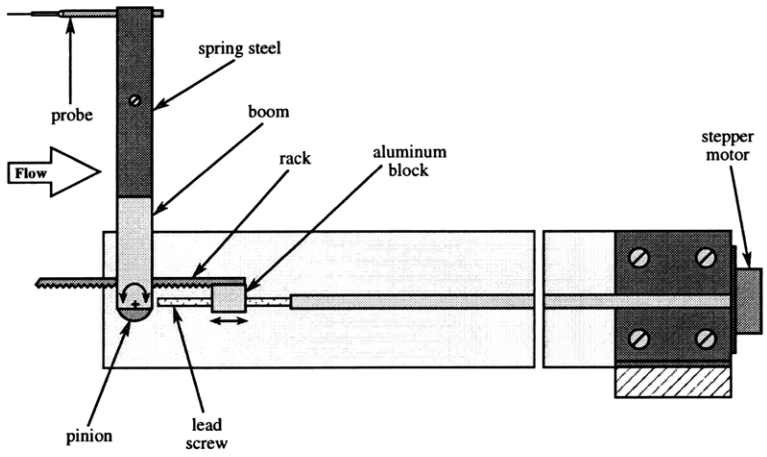

Figure 2-14: A diagram of the cross-wire probe rotation system (not to scale).

A small stepper motor with a resolution of 7.5° per step and located approximately 14 *in* downstream of the probe turns a shaft attached to the 2-56 lead screw. The lead screw then passes through a threaded hole in the aluminum block forcing the block to translate as the lead screw is turned by the stepper motor. The rack attached to the aluminum block is forced to translate as well, thereby turning the matching 0.5 *in* pitch diameter pinion gear and the attached boom holding the probe. The combination of stepper motor resolution, lead screw threading and pinion pitch diameter along with the motor driver operating in half-stepping mode produce an angular resolution of approximately 0.04°. Although the resolution is more than adequate for the applications, angular motion of the probe of less than 0.2° is not recommended due to friction impeding precise movements of the shafts, rack, aluminum block, and ball bearing. In fact, the above resolution should only be treated as a conversion factor between degrees and motor steps on a macroscopic level.

The assembled system is shown below in Figure 2-15 in position to take velocity measurements just behind the leading edge slat. As can be seen in Figure 2-15, the

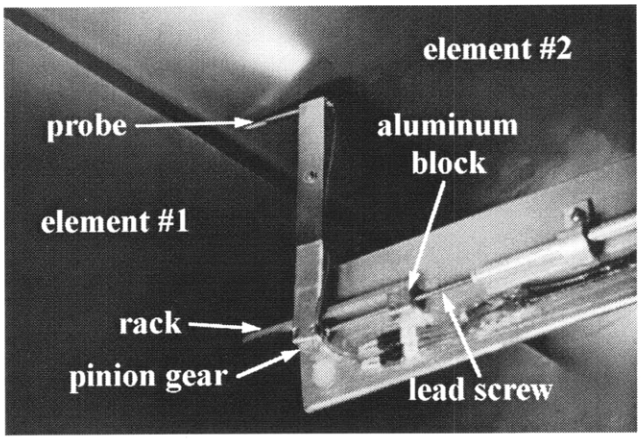

Figure 2-15: Complete cross-wire system shown in data taking position.

cross-wire probe is held in a slot 3.75 *in* from its pivot point by tightening a screw in the middle of the boom extending from the pinion. This screw pulls the aluminum boom and the piece of spring steel together, thereby squeezing down on the steel shell of the probe. Other methods of attachment in this system include two set screws for the shaft-motor combination and tapping the other end of the shaft for the lead screw insertion (along with a tightening nut). The aluminum block is simply turned onto the lead screw using the threaded hole and is free to slide back and forth. The rack is attached to the aluminum block using machine screws while the matching pinion gear turns on a shaft pressed into a ball bearing mounted in the main support structure.

The probe may be rotated about any point in space by computing the distances the two cartesian axes must move and by scaling the speeds of the stepper motors of those axes. However, due to limitations on starting speeds of the traverse motors, the rotation about a particular point is only guaranteed after the entire motion is complete. This limitation of the rotation system does not allow the use of this feature near the airfoils since the lack of correctly scaled speeds may damage the probe by running it into a surface.

2.6.2 System Calibration

Before the cross-wire probe can be used to measure the velocity quantities of interest, the probe must be calibrated in a fairly simple and efficient way. In order to perform

the calibration, a sparse look-up table approach is used along with repeated curve fits and evaluations of those curve fits as described by Lueptow et al.[15] but with a coordinate transformation modification similar to that of Gresko [14]. This look-up table method of cross-wire calibration and some sample calibration results are presented in the current section. It must also be noted that the current system requires that the airfoils be taken off the mounting shaft so as to maintain a horizontal flow at the pitot and cross-wire probe locations.

2.6.2.1 Calibration Method

In order to calibrate the cross-wire probe an entire spectrum of velocities, Q, and relative flow angles, γ, must be presented and data at those conditions taken from both wires of the probe. The probe rotation system described in the previous section provides the necessary flow angle variability while the motor in the wind tunnel allows for flow velocities up to approximately $21.5\,m/s$. For each of the calibration points, the voltage output of each hot-wire is recorded along with the rotation angle and the velocity measured by a pitot probe (located at the same streamwise location and oriented to be parallel to the mean flow). The pitot velocity and the rotation angle then become the reference total velocity and the relative flow angle for the calibration. Rather than converting the voltage counts from the A/D board (0 to 4096) into actual voltages, the counts themselves are stored in order to eliminate an unnecessary mathematical operation which would become cumbersome when a large number of data points is taken. The calibration data looks quite similar to the generic calibration plot in Lueptow et al.[15] when plotted on the E_1–E_2 plane as shown in Figure 2-16. The pattern of the data is also as expected with each arc representing voltage data at the same calibration velocity and each line of constant relative flow angle radiating from the lower left.

The calibration procedure used in these experiments digresses from the one proposed by Lueptow et al.[15] at this point. While the the latter recommends proceeding to spline the data as is, the procedure used takes advantage of the resemblance of the data to polar coordinates as was done by Gresko [14]. In fact, this is not surprising

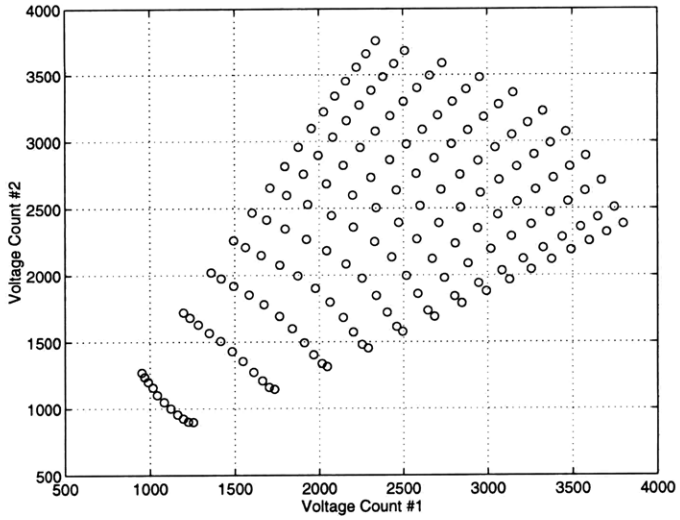

Figure 2-16: Sample cross-wire calibration plane.

since the velocity magnitude should be related to the square of the hot-wire voltage according to the relation implied by King's Law that $Q \propto E^2$. Since the voltage output offset is rather arbitrary for each wire, a nominal origin should be found prior to continuing with the calibration. This origin is approximated as the intersection between a least squares linear fit for the two extreme relative flow angles. Once the nominal origin is found, the voltage offsets (origin coordinates in E_1 and E_2) are subtracted from the measured voltage counts to better approximate the polar coordinate nature being exploited in this version of the look-up table calibration. The next step is to calculate the sums of the squares of the voltage count pairs, $\mathcal{S} = E_1^2 + E_2^2$, as well as the ratio of the voltage count pairs, $\mathcal{R} = E_2/E_1$, the results of which are plotted in Figure 2-17 below.

The most noticeable difference between Figures 2-16 and 2-17 is that the calibration plane of the latter is more efficiently packed in a cartesian manner. Figure 2-16 contains large unused areas of the E_1–E_2 calibration plane in the upper left and lower right portions of the figure. The more efficient packing allows for a much larger portion of the resulting look-up table entries to be useful in the experimental runs. This more efficient data management is the major advantage of the current method over that of Lueptow et al.[15]. An additional step of taking the arctangent of the ratio (as

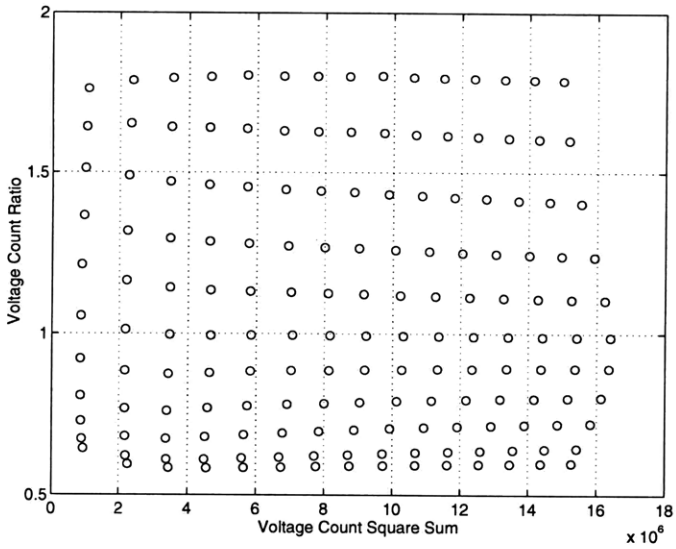

Figure 2-17: Sample polar coordinate cross-wire calibration plane.

performed by Gresko [14]) seems logical but would require the same time consuming mathematical operation to be performed on the thousands of incoming data points during testing. Although it may seem advantageous from a data behavior standpoint to perform the operation, the added time required to process the data for a minimal increase in accuracy likely does not warrant that particular extension. In fact, since the behaviors of the hot-wires are not identical (due to differing resistances), the true benefit of the arctangent operation is not known. Likewise, Gresko [14] takes the square root of $\mathcal{S}$ but this would again add a costly mathematical operation during experimental data collection while not providing any accuracy advantages.

The next step in the calibration procedure is to develop the look-up table from the newly created sum of squares and ratio data. The look-up table comes out of a method similar to that employed by Lueptow et al.[15] but with several modifications to account for the change in variables from E_1, E_2 to $\mathcal{S}$, $\mathcal{R}$:

1. Cubic spline along each flow angle, γ, to obtain $\mathcal{R}$ and Q as functions of $\mathcal{S}$, i.e. $\mathcal{R}(\mathcal{S})|_\gamma$ and $Q(\mathcal{S})|_\gamma$.

2. Evaluate the splines in (1) for each γ at regularly spaced intervals of $\mathcal{S}$.

3. Cubic spline along each $\mathcal{S}$ interval to obtain $\gamma(\mathcal{R})|_\mathcal{S}$ and $Q(\mathcal{R})|_\mathcal{S}$.

4. Evaluate the splines in (3) for each $\mathcal{S}$ at regular spaced intervals of $\mathcal{R}$ to complete the look-up table with each ($\mathcal{S}$, $\mathcal{R}$) pair corresponding to a unique Q and γ.

The above method results in a look-up table with regularly spaced coordinates in $\mathcal{S}$ and $\mathcal{R}$ with more useful entries than in the previous method [15]. Rather than just having a wedge of calibration data as shown in Figure 2-16, the look-up table makes use of the entire calibration plane shown in Figure 2-17. An almost identical look-up table may be obtained by reversing the order of splining such that step (1) occurs along each velocity while the second occurs along each regularly spaced interval ratio of voltage counts. In fact, the choice of splining order may be based on the the number of velocities and relative flow angles such that the lesser number of spline fits need to be made. The time saved by this choice, however, is minimal as compared to the calibration data collection time.

Once the calibration look-up tables are computed, the velocity magnitude and the relative flow angle may be calculated by subtracting the voltage offsets from the measured voltage counts, computing $\mathcal{S}$ and $\mathcal{R}$, and using a bilinear interpolation between entries in the look-up tables. The use of an efficient bilinear interpolation is the motivation behind using regularly spaced intervals in the creation of the look-up tables. The velocity components are then calculated from the following trigonometric relations:

$$U = Q\cos(\gamma) \tag{2.20}$$

$$V = Q\sin(\gamma) \tag{2.21}$$

2.6.2.2 Sample Calibration Results

For the sample calibration results in this section, the velocity was varied from a minimum nominal velocity of $1.5\,m/s$ to the maximum velocity of $21.5\,m/s$ in steps of approximately $1.4\,m/s$. For each of these calibration velocities the probe was pitched through the practical range of relative flow angles of approximately $-30° \leq \gamma \leq +30°$ [15] in approximate steps of 6°. A total of 15 velocities and 11 relative flow angles

were used to create the calibration space of the probe. The voltage counts of both wires and the probe rotation angle were recorded at each of these 165 calibration points while the mean flow velocity as indicated by the pitot probe (located at the same streamwise location) was recorded at the end of each of the 15 nominal velocity runs.

The raw and modified raw calibration data used for the sample calibration results are the same as shown in Figures 2-16 and 2-17. After performing the splining and evaluating as outlined above, the look-up tables ($Q(\mathcal{S},\mathcal{R})$ and $\gamma(\mathcal{S},\mathcal{R})$) may be plotted as either three-dimensional surfaces or in contour plots as presented in Figures 2-18 and 2-19. As can be seen in Figure 2-18, the velocity magnitudes vary almost linearly with the sum of the voltage count squares as the spacing between velocities varies relatively little. The velocity calibration is also very nearly symmetric about $\mathcal{R} = 1$ although it does exhibit a slight dependence on the voltage count ratio but only at the higher velocities.

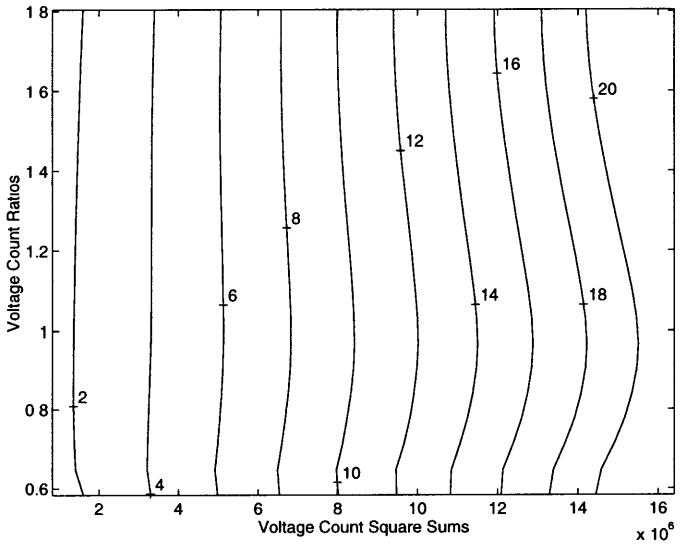

Figure 2-18: Sample velocity magnitude (m/s) contour plot.

The relative flow angle calibration in Figure 2-19 shows the opposite behavior as the velocity magnitude calibration as would be expected. The relative flow angle is almost solely a function of the the ratio of the voltage counts and nearly anti-symmetric about $\mathcal{R} = 1$. Some distortions do appear near the lowest velocities but

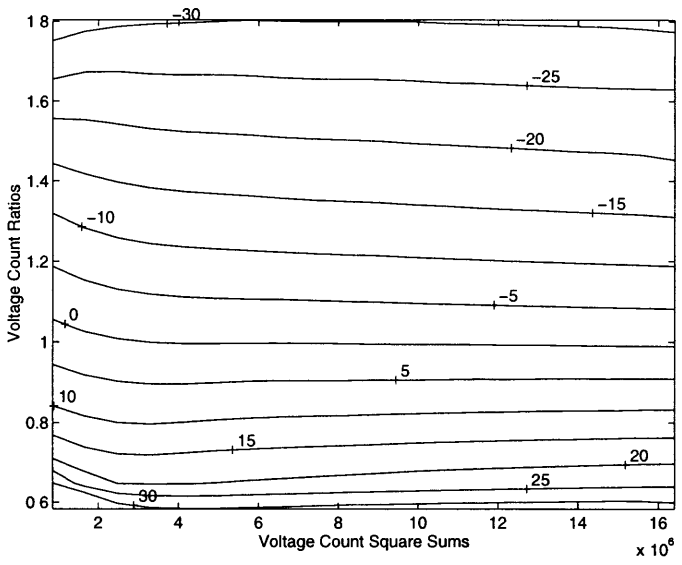

Figure 2-19: Sample relative flow angle (degrees) contour plot.

are likely due to the crosstalk of the wires at low speeds as the thermal wake of one wire interacts with the other wire. Again, these velocities are seldom encountered in the testing meaning that these slight distortions should not effect any experimental results. Also, since only the ratio was used rather than its arctangent, the contours of the relative flow angles tend to pack closer together as the ratio decreases. This concentration, however, would effect the calculated quantities only at the extreme flow angles not often encountered in the experimental runs.

Immediately after the calibration routine, the look-up table should be checked against known velocities and known relative flow angles. Typically, the calibration errors were limited to $\simeq 1\%$ of the pitot-indicated velocities and to within 0.1° of the given probe angles. The calibration errors should be recorded to serve as a baseline for drift errors which are discussed in Section 2.7.

It is important to note that the probe measures the flow angle only relative to its own axis rather than in cartesian or body coordinates. This necessitates the knowledge of the probe angle during the experimental runs since the difference between the probe angle and the relative flow angle will provide the cartesian angle of the flow. Also, given the surface angle of the body being studied the data may be converted into tangential and normal coordinates.

2.7 Experimental Procedure

The procedures for lift, drag, and wake–boundary layer profile data acquisition (using the hardware described in Sections 2.5 and 2.6) are outlined in the current section. In addition, data reduction procedures are given to demonstrate the transformation of raw data into that shown in Chapter 3. Finally, a discussion of cross-wire error and experimental testing conditions is provided. Typically, lift and drag data were taken separately from the wake–boundary layer profile data. For the latter measurements, the airfoil was secured using the support bolts to provide the highest possible system stiffness, with no reliance on the load cell reaction forces.

2.7.1 Lift and Drag Measurement

Lift data from the load cells and drag data from the wake profile velocities were taken simultaneously. The mean velocity profile was obtained at a streamwise distance of approximately 1.2 chord lengths from the trailing edge of the airfoil using the cross-wire system described in Section 2.6. The mean wake profile may also be obtained with a pitot probe, but the cross-wire system was employed since it is readily available and has a much better spatial resolution.

For each angle of attack of interest, a tare loading condition must be determined with no flow so that the aerodynamic loads may be separated from the effect of the airfoil weight. If more than one velocity is to be investigated, it is recommended that the velocity adjustments be performed at each angle of attack to minimize the number of tare loads required.

2.7.1.1 Lift Coefficient Measurement

When lift data (as well as the tare loads) are required, signals from the load cells are digitized, averaged and substituted for the E's into Equation 2.15 which is repeated

in Equation 2.22.

$$\begin{Bmatrix} F_{ap} \\ M_{ap} \\ T_{ap} \end{Bmatrix} = \begin{bmatrix} c_{0_F} & c_{1_F} & c_{2_F} & c_{3_F} & c_{4_F} \\ c_{0_M} & c_{1_M} & c_{2_M} & c_{3_M} & c_{4_M} \\ c_{0_T} & c_{1_T} & c_{2_T} & c_{3_T} & c_{4_T} \end{bmatrix} \begin{Bmatrix} 1 \\ E_1 \\ E_2 \\ E_3 \\ E_4 \end{Bmatrix} \tag{2.22}$$

It is recommended that the lift data be repeated several times and averaged so that any effects of higher frequency vibrations may be minimized.

Once the lift data (F_{ap}, M_{ap}, and T_{ap}) are obtained, the tare loads (F_{tare}, M_{tare}, and T_{tare}) are subtracted from those measured to calculate the aerodynamic loads without the effect of the weight of the airfoil in Equation 2.23.

$$\begin{Bmatrix} F_{aero} \\ M_{aero} \\ T_{aero} \end{Bmatrix} = \begin{Bmatrix} F_{ap} \\ M_{ap} \\ T_{ap} \end{Bmatrix} - \begin{Bmatrix} F_{tare} \\ M_{tare} \\ T_{tare} \end{Bmatrix} \tag{2.23}$$

The lift coefficient, C_L, may now be calculated using the standard formula of Equation 2.24

$$C_L = \frac{F_{aero}}{\frac{1}{2}\rho U_\infty^2 S} \tag{2.24}$$

where ρ, U_∞, and S represent the density, freestream velocity (as determined in Appendix B), and the planform area ($0.129\,m^2$ as noted in Section 2.4), respectively. A measure of the 2-dimensionality of the flow may be obtained by determining the spanwise location of the lift as the ratio, M_{aero}/F_{aero}. Ideally, this ratio should be approximately one half of the span ($10\,in$).

2.7.1.2 Drag Coefficient Measurement

The drag is determined by measuring the mean velocity profile 1.2 chord lengths ($\sim 12\,in$) behind the trailing edge of the airfoil system and calculating the momentum defect. In all of the experimental cases run throughout the course of the current

research, the velocity profiles were obtained by traversing vertically with the probe in equally spaced distance intervals to simplify drag coefficient calculation.

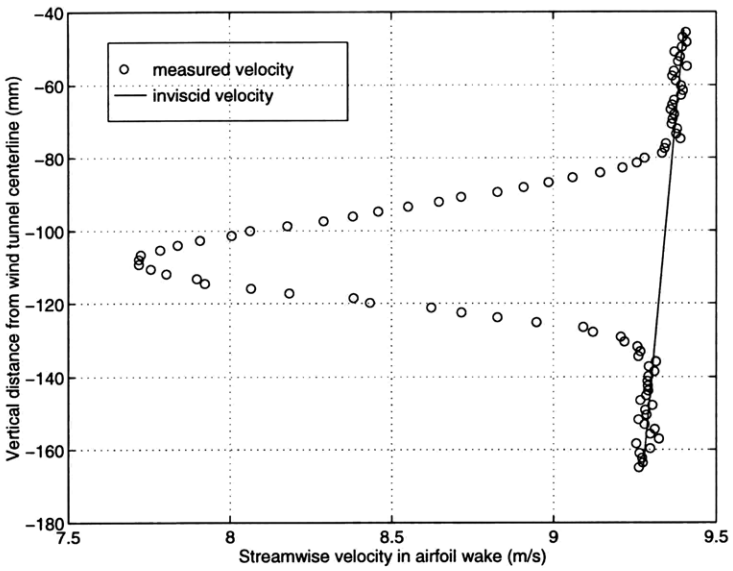

Figure 2-20: Sample wake velocity profile for C_D calculation ($U_\infty = 9.5\,m/s$, $\alpha = 5.1°$).

Once the velocity profile is measured, an "inviscid" velocity is approximated by a straight line fit from the first several data points across the airfoil wake to the last several data points as shown in Figure 2-20. This process also takes into account the slight curvature of the wake. The total pressure coefficient, C_{po}, is then calculated at each probe location from the following equation:

$$C_{po_i} = \left(\frac{U_{meas_i}}{U_{inv_i}}\right)^2 \tag{2.25}$$

where U_{meas_i} represents the velocity as measured by the probe and U_{inv_i} represents the "inviscid" velocity as determined by the linear fit. The drag coefficient, C_D, may then be calculated from the wake momentum thickness θ:

$$C_D = \frac{2\theta}{c} \tag{2.26}$$

$$= 2\int \left(1 - \frac{u}{u_e}\right)\frac{u}{u_e}\,\mathrm{d}\left(\frac{z}{c}\right) \tag{2.27}$$

$$\simeq 2\frac{\Delta z}{c}\sum_{i=1}^{N}\left(\sqrt{C_{po_i}} - C_{po_i}\right) \tag{2.28}$$

In the above equation, Δz is the distance interval between velocity measurement locations, c is the chord as noted in Section 2.4, and N is the total number of velocity measurement locations.

The momentum thickness at the measurement station is typicallly slightly greater than its far-downstream value, since the pressure field of the airfoil still has some small effect there. MSES predicts that the measured θ is about 2.6% greater than the final wake θ. This small difference was ignored here.

2.7.2 Wake and Boundary Layer Profiles

2.7.2.1 Procedure

Measuring the profiles on the airfoil elements themselves involves at least two passes at a given streamwise location. This multiple pass approach allows the profile points to be concentrated in areas of rapid changes of velocity quantities to capture as much of the local flow behavior as possible. Since each profile point is rather costly in terms of data acquisition and especially reduction time, it is important to optimize the locations of those profile points to maximize the usefulness of the data while minimizing the run times. The multiple pass method also allows the probe to traverse approximately normal to the local streamlines. The multiple pass procedure for a given streamwise location becomes the following:

1. The cross-wire probe is brought to within approximately $1\,mm$ of the airfoil surface.

2. A sparse mean-velocity profile is taken of the entire boundary layer and wake region while traversing away from the airfoil element to provide a preliminary idea of the flow.

3. A median flow angle is approximated from the sparse mean-velocity profile.

4. A set of profile locations is tailored to capture the regions of large velocity variation.

5. The probe is moved back to the vicinity of the airfoil and positioned as closely as possible to the surface without any contact.

6. The detailed velocity profile is taken using the acquisition and reduction procedure of Section 2.7.2.2 while traversing normal to the median flow angle determined above.

Several important notes must be made with respect to the above procedure. First, since the sparse velocity profile only measures the mean flow without any fluctuations, less data points may be used and at a lower sampling frequency than that for the detailed profile. Also, the tailored set of profile locations should take into account the traversing angle. Finally and probably most important, the probe should be moved closer to the airfoil with extreme caution since touching the surface could damage the hot-wires and delay further investigation.

2.7.2.2 Data Acquisition and Reduction

For the detailed velocity profile where mean and fluctuating quantities are measured, approximately 600,000 data points are digitized at a sampling frequency of $25\,kHz$ and anti-alias filtered at $10\,kHz$ at each location in the profile. To minimize the memory requirements, the data is processed as it is digitized in blocks of 32,000 points; while one block of data is being processed the next block is digitized. Although this process results in non-continuous data, the statistics of the flow velocities should remain unaffected.

The digitized voltage count data are converted into a velocity magnitude, Q, and a probe-relative flow angle, γ_{probe}, using a bilinear interpolation within the look-up tables developed in Section 2.6.2. It must be noted that the interpolation routine discards data falling outside of the calibration range of the look-up tables. Since the probe itself may be at some angle relative to the horizontal, the true flow angle with respect to the horizontal, γ_{xz}, is then the difference between the probe orientation angle and the probe-relative flow angle. For each of the valid data points, the velocity magnitudes and flow angles relative to the horizontal are then converted into cartesian

velocities, U_{xz} and V_{xz}, using the following formula from Section 2.6.2:

$$U_{xz} = Q\cos(\gamma_{xz}) \tag{2.29}$$

$$V_{xz} = Q\sin(\gamma_{xz}) \tag{2.30}$$

In order to compute the mean velocities ($\overline{U}$ and $\overline{V}$), root-mean-square of the velocities ($(\overline{u^2})^{\frac{1}{2}}$ and $(\overline{v^2})^{\frac{1}{2}}$) and the mean of the product of the velocities ($\overline{uv}$), the data taking routine tracks the following sums (in tunnel coordinates):

1. $\sum U_{xz}$
2. $\sum V_{xz}$
3. $\sum U_{xz}^2$
4. $\sum V_{xz}^2$
5. $\sum U_{xz}V_{xz}$

Also, since the bilinear interpolation routine discards data points falling outside of the calibration plane, the total number of valid data points, N_{valid}, must be recorded. After the 6×10^5 or so data points have been digitized, converted into velocities, and turned into the sums above, statistics may be computed using the following formulas:

$$\overline{U}_{xz} = \frac{1}{N_{valid}}\sum U_{xz} \tag{2.31}$$

$$\overline{V}_{xz} = \frac{1}{N_{valid}}\sum V_{xz} \tag{2.32}$$

$$(\overline{u_{xz}^2})^{\frac{1}{2}} = \left|-\overline{U}_{xz}^2 + \frac{1}{N_{valid}}\sum U_{xz}^2\right|^{\frac{1}{2}} \tag{2.33}$$

$$(\overline{v_{xz}^2})^{\frac{1}{2}} = \left|-\overline{V}_{xz}^2 + \frac{1}{N_{valid}}\sum V_{xz}^2\right|^{\frac{1}{2}} \tag{2.34}$$

$$\overline{uv}_{xz} = -\overline{U}_{xz}\overline{V}_{xz} + \frac{1}{N_{valid}}\sum U_{xz}V_{xz} \tag{2.35}$$

The statistics calculated above along with the probe position are then stored for each point in the particular profile. These statistics may also be rotated through

some prescribed angle, β_{12}, from coordinate frame #1 into coordinate frame #2 by applying Equation 2.36 to the mean and *rms* velocities and Equation 2.37 to the mean of the product of the velocities.

$$\left\{ \begin{array}{c} U \\ V \end{array} \right\}_2 = \left[\begin{array}{cc} \cos\beta_{12} & -\sin\beta_{12} \\ \sin\beta_{12} & \cos\beta_{12} \end{array} \right] \left\{ \begin{array}{c} U \\ V \end{array} \right\}_1 \tag{2.36}$$

$$\overline{uv}_2 = \overline{uv}_1 \left(\cos^2\beta_{12} - \sin^2\beta_{12}\right) + \left(\left(\overline{u_1^2}\right) - \left(\overline{v_1^2}\right)\right) \cos\beta_{12} \sin\beta_{12} \tag{2.37}$$

2.7.3 Cross-wire Measurement Errors

As is common with hot-wire probes, drift error tends to creep into the data after extended periods of testing. Although the hot-wire anemometer was able to prevent the probes from drifting appreciably even overnight, the calibration should still be checked periodically and performed again if the error is not within an acceptable range. In order to facilitate this drift error checking, the calibration check discussed near the end of Section 2.6 should be repeated with the airfoil in place at some known angle of attack. In these experiments the difference between the cross-wire velocity Q_x and the pitot indicated velocity Q_{pitot} typically increased from $\sim 1\%$ to $\sim 2\%$, while the relative flow angle difference changed from $\sim 0.1°$ to $\sim 4.8°$ for $U_\infty = 10.6\, m/s$ and $\alpha = 0°$. These discrepancies are due to the presence of the airfoil disturbing the flow pattern throughout the test section. Although the pitot and the cross-wire probes are at the same streamwise location, they are not at the same vertical position thereby causing the probes to experience flow velocities differing by the additional $\sim 1\%$ as predicted by MSES. The difference in angle is due to the inclination of the flow with respect to the horizontal as caused by the presence of the lifting airfoil. These new calibration "errors" were recorded and used as the new baselines for determining drift error.

Another cause for cross-wire measurement errors is a variation in temperature over the course of the experiment. However, the temperature during the entire course of the experimental investigation remained in the range of $23.5°C$–$24.5°C$ allowing us to

assume that there was no significant temperature effect on the hot-wire measurements and that the kinematic viscosity, ν, was constant and equal to $1.50 \times 10^{-5} m^2/s$.

2.7.4 Experimental Test Conditions

The choice of test conditions for this research was driven primarily by the limitations of the wind tunnel itself. Although the wind tunnel motor is capable of driving the flow at over $20\,m/s$, the velocity during actual testing can only be about half of the maximum due to the cross-wire calibration requirements. The reason behind this limiting condition is illustrated by a brief investigation of typical computational flow predictions in the experimental Reynolds number range. As can be seen in Figure 2-21, according to MSES the typical pressure coefficient peaks at approximately $C_p = -3$ along the surface of the leading element. This minimum value of pressure coefficient can be used to approximate the maximum magnitude of velocity that is likely to be encountered in the experiments by applying Equation 2.38.

$$\frac{U}{U_\infty} = \sqrt{1 - C_p} \tag{2.38}$$

This produces an estimate of $U/U_\infty \simeq 2$ at the point of highest expected velocity. Since the maximum wind tunnel velocity is approximately $21.5\,m/s$, the maximum cross-wire calibration velocity is limited to this same value of $21.5\,m/s$. This implies that the maximum freestream velocity during airfoil testing not exceed one half of the maximum cross-wire calibration velocity or $\sim 11\,m/s$ thereby limiting the Reynolds number to a maximum of 1.86×10^5.

The freestream test velocities, therefore, were chosen based on this limitation. As high a velocity as possible was chosen to maximize the Reyolds number ($\Re = 1.8 \times 10^5$, $U_\infty = 10.6\,m/s$) as well as a slightly lower velocity for comparison purposes ($\Re = 1.4 \times 10^5$, $U_\infty = 8.4\,m/s$).

For each velocity in the boundary layer – wake profile portion of the investigation, seven streamwise locations were chosen based on several criteria. Two points ($x/c = 0.20$ and $x/c = 0.30$) were placed on the first element to provide a measure of the

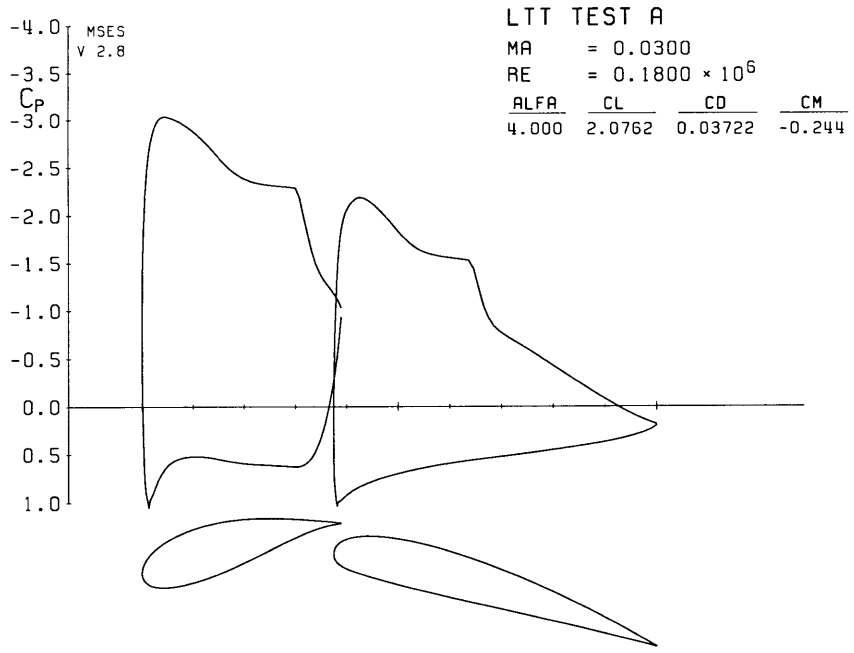

Figure 2-21: Pressure coefficient ($\Re = 1.8 \times 10^5$, $\alpha = 4°$).

initial conditions of the element's wake. A profile was also taken directly behind the leading element ($x/c = 0.40$)for a measure of the near wake flow properties. Finally, four more streamwise locations ($x/c = 0.48, 0.54, 0.60, 0.70$) are taken to track the flow evolution. Although it would have been preferrable to obtain measurements at other angles of attack besides the $\alpha = 0°$ case, wind tunnel time limitations did not permit this next step of the experimental investigation.

Chapter 3

Results and Discussion

Using the procedures described in Section 2.7, data was obtained for both lift and drag as well as for boundary layer – wake profiles, the main motivation behind this research. The present chapter focuses on this obtained data. After a presentation and discussion of characteristic lift-drag data, the velocity profile data is shown and compared to computational predictions. The two Reynolds number cases of experimental boundary layer – wake velocity profile data are also compared.

3.1 Lift and Drag

Before proceeding to the detailed study and comparison of the interacting shear layers in Section 3.2.3, we must first establish that the gross flow around the airfoil in the experiment is similar to that determined with the computational code MSES. This is accomplished by building several lift-drag polars for the airfoil system at several velocities and, therefore, Reynolds numbers. However, since the purpose of this section is merely to verify the gross similarity of the experimental flow with that of the computational flow, the complete lift-drag curve and polar of only one test condition is shown. The presence of massive separation at the extreme angles of attack and at the lower Reynolds numbers and its absence at the higher Reynolds numbers is also presented and discussed.

3.1.1 Typical Lift and Drag Data

Using the procedure outlined in Section 2.7.1, lift and drag data sets were collected for Reynolds numbers ranging from 1.05×10^2 ($U_\infty = 6.2\,m/s$) to 1.80×10^2 ($U_\infty = 10.6\,m/s$). To illustrate the conditions at both of the test Reynolds numbers of the boundary layer – wake profiles, the drag and lift data of a median Reynolds number ($\Re = 1.61 \times 10^5$) are presented.

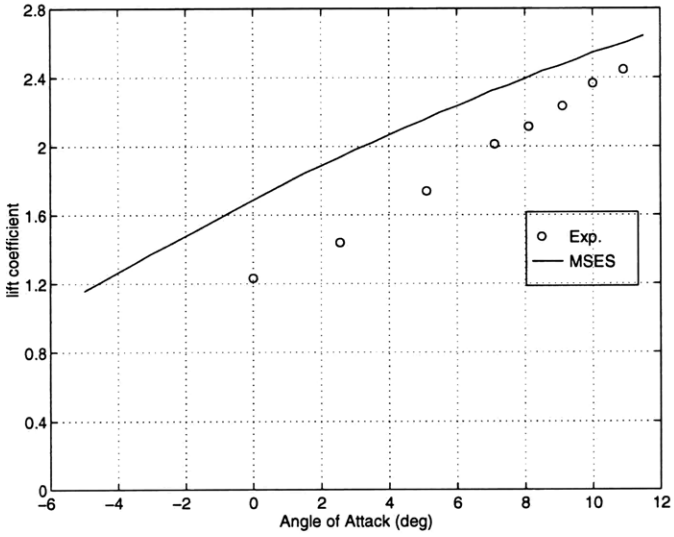

Figure 3-1: Lift curve for $\Re = 1.61 \times 10^5$.

Figure 3-1 shows the lift as a function of the angle of attack as measured relative to the airfoil position described in Section 2.4. There appears to be an offset in the angle of attack between the experimental and computational results. If this were a constant offset throughout the range of α, it could be attributed to an error in angle measurement. However, there is also a mismatch in the curvature of the lift curve; the experimental lift appears to be increasing at a faster rate than the computationally predicted lift. This implies that other effects besides positioning errors are present. One possibility is the end-plate effect. Since the load cells measure the lift for the entire wing rather than just at the center airfoil section, the experimental lift coefficient is actually an average across the span and includes the likely lower lift coefficients at the outer sections caused by the boundary layer of the end-plates. The boundary layer effect would also serve to explain the decreasing difference in C_L at the higher

angles of attack since the local velocities on the suction sides of the airfoil are higher at these higher angles creating a thinner boundary layer and decreasing the affected flow region. It is also possible that the end-plates themselves may be too small to contain most of the pressure field caused by the airfoil. This would cause a spanwise leakage of flow and a reduction in local lift coefficient at the outer edges of the span thereby lowering the overall lift.

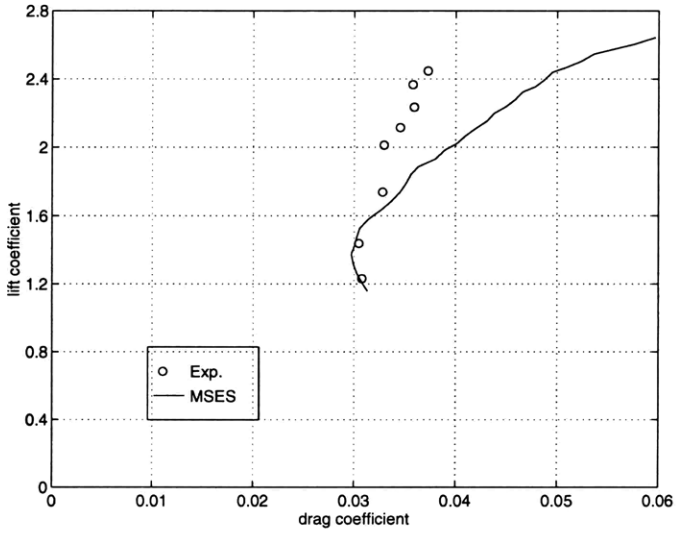

Figure 3-2: Lift-drag polar for $\Re = 1.61 \times 10^5$.

Figure 3-2 shows the lift-drag polar corresponding to the lift curve of Figure 3-1. The most noticeable feature of this plot is the deviation of data at the higher lift coefficients. Again, the end-plates may play a role by confining the shear layer to the span over the airfoil and then allowing it to expand to the full width of the test section by the mean wake profile location. This expansion and, therefore, smearing of the wake shear layer may reduce the momentum deficit measured for drag calculation. However, these lift and drag end-plate effects are difficult to quantify and require further study. Another source of error may be spanwise variation in the flow at such low Reynolds numbers. As Guglielmo and Selig[12] discovered, spanwise variations of profile drag at $\Re = 2 \times 10^5$ typically run on the order of 5–40% in nominally two-dimensional flow.

Overall, there appears to be a low-Reynolds number effect present with the "bowing" effect of the lift-drag polar in the 1.5–2.0 range of C_L. In this range, the drag

rise slows as compared to the rise in lift with the higher angles of attack. This effect also appears to be more prevalent in the experimental data as it occurs over a larger range of lift coefficients. Fortunately, however, the lift and drag do match well at the boundary layer – wake profile test conditions ($1.2 \leq C_L \leq 1.3$) although the actual angles of attack may suffer from an offset error.

3.1.2 Reynolds Number Effects at High Angle of Attack

The Reynolds numbers in these experiments is actually marginal for studying some of the flow phenomena. Not only is it typically difficult to obtain good computational data for this range, but the experimental data also illustrates the flow's sensitivity to the Reynolds number — especially at the higher angles of attack. This effect at higher angles of attack can be seen by comparing velocity profiles in Figures 3-3 and 3-4.

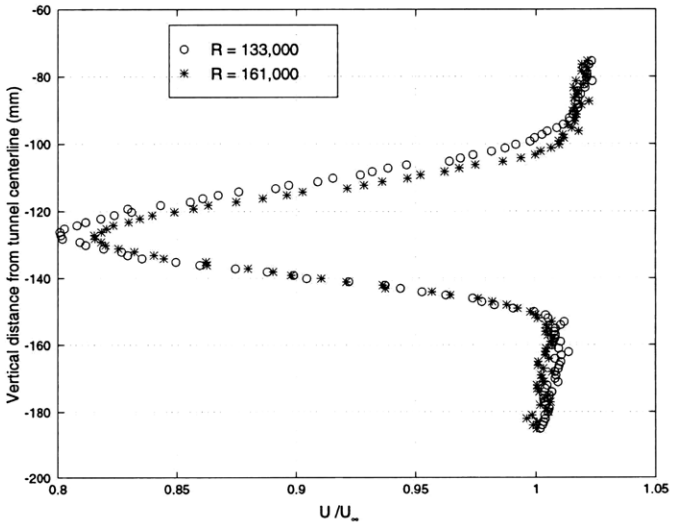

Figure 3-3: Far-wake mean velocity profile for $\alpha = 10°$.

While the non-dimensional wake velocities are nearly identical for the $\alpha = 10°$ case, there is an enormous difference in wakes for the $\alpha = 11°$ case. The higher Reynolds number ($U_\infty = 9.5\,m/s$) condition produces a similar wake at both angles of attack whereas the lower Reynolds number condition ($U_\infty = 7.9\,m/s$) creates a much larger wake at $\alpha = 11°$. In fact, comparing the airfoil location and height as shown in Figure 3-4, we see that the wake produced at the lower Reynolds number and

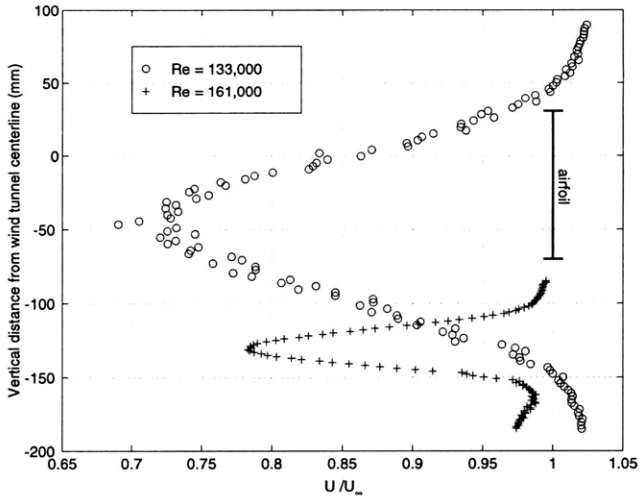

Figure 3-4: Far-wake mean velocity profile for $\alpha = 11°$.

higher angle of attack is almost three times larger than the airfoil height itself. The appearance of this extremely large wake with only a 1° change in α points towards some sort of massive and likely laminar separation of the flow. This sudden wake "burst" also indicates that measurements near $C_{L_{max}}$ at these Reynolds numbers would not produce results of typical interest as the C_L-limiting flow separation would not be turbulent.

3.2 Boundary Layer – Wake Profiles

As noted in Section 2.7.4, boundary layer and wake profiles were taken at seven streamwise locations along the suction (top) side of the airfoil assembly at a nominal angle of attack of 0° as measured relative to the positioning described in Section 2.4. All profiles were taken at two freestream velocities, $U_\infty = 8.4m/s$ and $U_\infty = 10.6m/s$, corresponding to the two Reynolds numbers of $\Re = 1.4 \times 10^5$ and $\Re = 1.8 \times 10^5$, respectively. While the higher Reynolds number case is shown in the present section, the velocity profiles for the lower Reynolds number case appear in parallel order in Appendix C.

Before the velocity data is presented and discussed, the flow predicted by MSES is shown to provide an overall picture of the flow. After the velocity profiles are

discussed, the Reynolds shear stress results are shown and compared to the computational predictions at both flow Reynolds numbers. Finally, the two Reynolds number cases are compared to each other.

3.2.1 MSES Predicted Outer Flow

In order to discuss some of the flow features found in the velocity profiles of Section 3.2.3 a general snapshot of the overall flow is examined. A better model of the flow is obtained by matching the lift coefficient of the simulation to that of the experiment ($C_L = 1.22$) rather than matching the angles of attack. Figure 3-5 illustrates the overall flow with the pressure coefficient distribution along the airfoil as well as the viscous–inviscid boundary representative of the surface streamlines as displaced by the local displacement thickness.

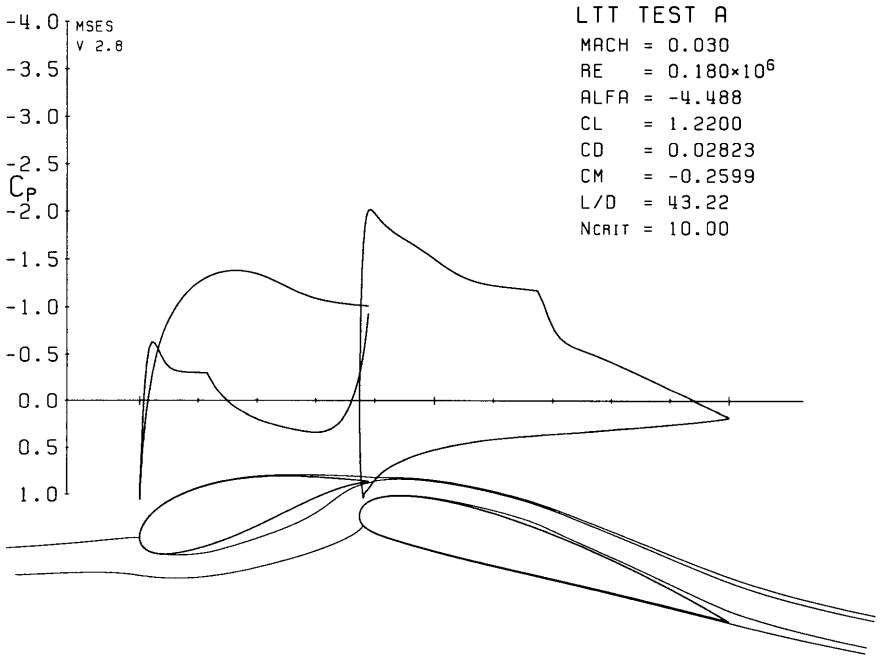

Figure 3-5: Pressure coefficient ($\Re = 1.8 \times 10^5$).

The most noticeable features of Figure 3-5 include the two laminar separation regions: a small laminar bubble on the top surface of the second element ($x/c \simeq 0.65$) and a large separated region on the lower surface of the first element ($x/c \simeq 0.35$). As will be apparent in Section 3.2.3, evidence of the larger separated region from below

the leading element can be detected in the flow emanating from the gap between the airfoils.

3.2.2 Data Rotation and Non-Dimensionalization

The wake–boundary layer results obtained using the equipment and methods discussed in Sections 2.6 and 2.7.2 are presented in body and shear layer coordinates rather than in the wind tunnel coordinate system. The velocity data measured in the wind tunnel "xz" axis system has been rotated through the angle β normal to the airfoil surface to obtain streamline, s, and normal, n, velocity data. These angles are shown in Figure 3-6 at their locations along the airfoil and listed in Table 3.1. Also listed in Table 3.1 are the ratios of shear layer edge velocity to freestream velocity (U_e/U_∞) and of the shear layer height to the reference chord (δ/c) used to non-dimensionalize the velocity and distance data. This particular non-dimensionalization is chosen to correspond to that of Adair and Horne[2].

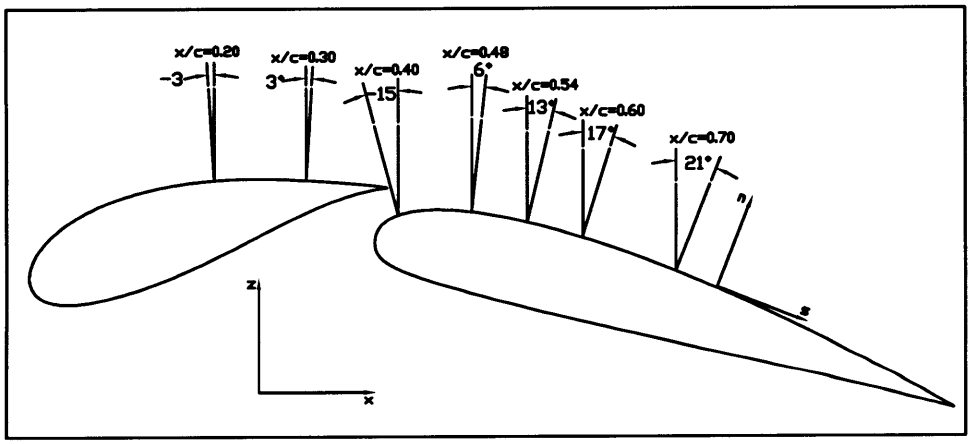

Figure 3-6: Rotation angles, β, of data at each streamwise location.

To determine both the shear layer edge velocity and the shear layer height, the mean streamwise velocity component was first plotted as a function of the distance moved by the probe. The actual origin (wall location) of the data is unknown and difficult to measure due to the deflection of the cantilevered airfoil system and to the construction of the probe itself. The deflection of the system (due to lift) with the wind tunnel on does not allow for the measurement before or after testing since

x/c	0.20	0.30	0.40	0.48	0.54	0.60	0.70
β	$-3°$	$3°$	$-15°$	$6°$	$13°$	$17°$	$21°$
U_e/U_∞	1.50	1.32	1.35	1.54	1.49	1.39	1.26
δ/c	0.0078	0.0091	0.052	0.048	0.057	0.064	0.076

Table 3.1: Profile location data for $\Re = 1.8 \times 10^5$.

the deflection is unknown as well. The cross-wire probe meanwhile averages the local velocity across the entire hot-wire length causing errors in the near-wall measurements and only allowing the centers of the wires to within one half of the cross-wire box-side length (0.25 mm) at best. A likely origin (or offset) was, therefore, deduced from the plots based on data extrapolation and other, more subjective factors such as comparisons to previous data and simple approximation.

The edge of the shear layer (outside edge of viscous layer of the leading airfoil element) was then approximated as the position above the airfoil where the mean streamwise velocity becomes more or less constant and the turbulence quantities tend to zero. It then follows that the shear layer edge velocity be assigned the velocity measured at the location of the shear layer edge. Unless otherwise noted, the data presented in the following sections has been non-dimensionalized with the shear height δ and with the shear layer edge velocity U_e.

3.2.3 Velocity Data Profiles

After rotating and non-dimensionalizing the data as described in Section 3.2.2, the mean and rms velocity data are shown in the current section as a function of n/δ where n is the normal coordinate and δ is the shear layer height. The experimental data are divided according to the locations of the profiles: the two profiles starting at the first airfoil element to illustrate the wake initial conditions followed by the five profiles starting on the second element to illustrate the wake development. Also, the mean streamwise velocity profiles are compared to the profiles predicted by MSES.

3.2.3.1 Element #1 Boundary Layer

As Weygandt and Mehta[23] showed, the boundary layer conditions at the trailing edge serve as the initial conditions for the wake of the airfoil element and, therefore, significantly affect the properties of the airfoil wake. According to Weygandt and Mehta[23], a laminar boundary layer creates substantial spanwise variations in mean velocity and Reynolds stresses due to well organized streamwise vortical structures whereas turbulent boundary layers produce much less spanwise flow variation. Before proceeding to the wake and the boundary layer of the second airfoil element we must examine the boundary layer of the leading airfoil element as it may indicate possible explanations of the wake–boundary layer data.

Figures 3-7 and 3-8 depict the mean streamwise and normal velocities, respectively, at the first two profile locations non-dimensionalized according to Section 3.2.2. While the mean velocities at the edge of the shear layer $x/c = 0.20$ has reached a constant level, it appears that the profile at $x/c = 0.30$ is somewhat incomplete and would have benefited from additional profile points. Although the normal velocity increases with the distance from the airfoil surface, the streamwise velocity maintains nearly the same pace thereby keeping the actual flow angle nearly constant ($\pm 2^\circ$ for $x/c = 0.20$ and $\pm 3^\circ$ for $x/c = 0.30$) throughout the boundary layer.

These mean streamwise velocities have also been plotted on the airfoil along with the MSES velocity profile as shown in Figure 3-9. Although the first profile location appears to be in good agreement with the predicted flow, the second MSES profile suggests the onset of separation which does not seem to be the case in the experiment at this particular streamwise location. Again, it must be noted that there is an unknown error in vertical positioning of the profiles since the distance from the airfoil surface is unknown.

The non-dimensionalized versions of the turbulence quantities $(\overline{u_s^2})^{\frac{1}{2}}$, $(\overline{u_n^2})^{\frac{1}{2}}$, and $-\overline{u_s u_n}$ are plotted for the boundary layer of the first element in Figures 3-10, 3-11, and 3-12, respectively. Although the streamwise root-mean-square velocity appears to be rising in the middle portion of the shear layer, the low magnitude of the *rms*

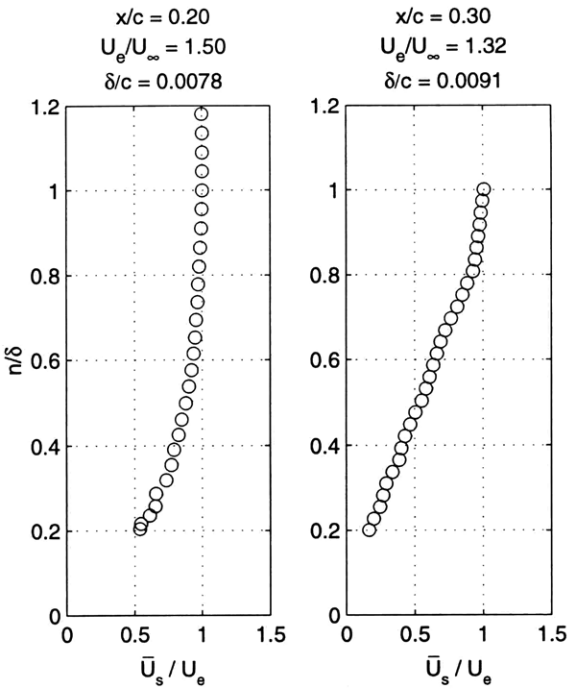

Figure 3-7: Mean streamwise velocity on Element #1 ($\Re = 1.8 \times 10^5$).

velocity (less than 1.5% of the edge velocity) indicates that the flow is still laminar along the upper portion of the leading element. Qualitatively, the same holds true for the cross-stream *rms* velocity as well as for the Reynolds shear stress; the magnitudes grow downstream but the flow appears to remain laminar. This laminar boundary layer may then cause organized streamwise vortical structures to form in the wake as observed by Weygandt and Mehta[23]. The presence of such structures, however, was not observed or even investigated due to the lack of a spanwise traverse degree of freedom.

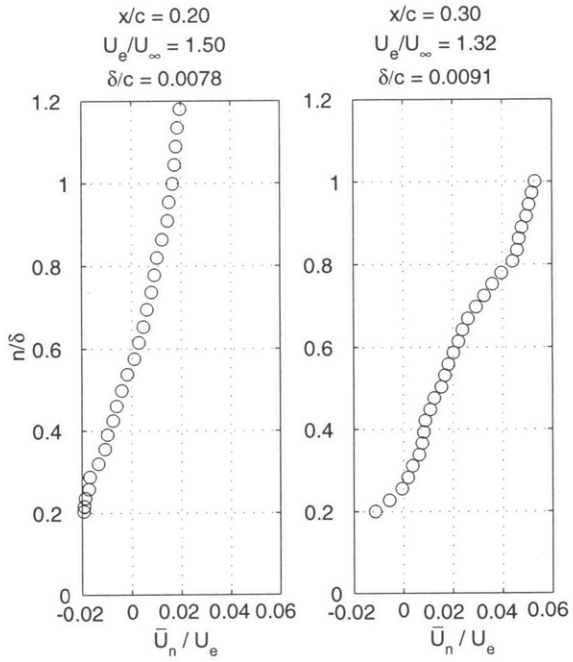

Figure 3-8: Mean normal velocity on Element #1 ($\Re = 1.8 \times 10^5$).

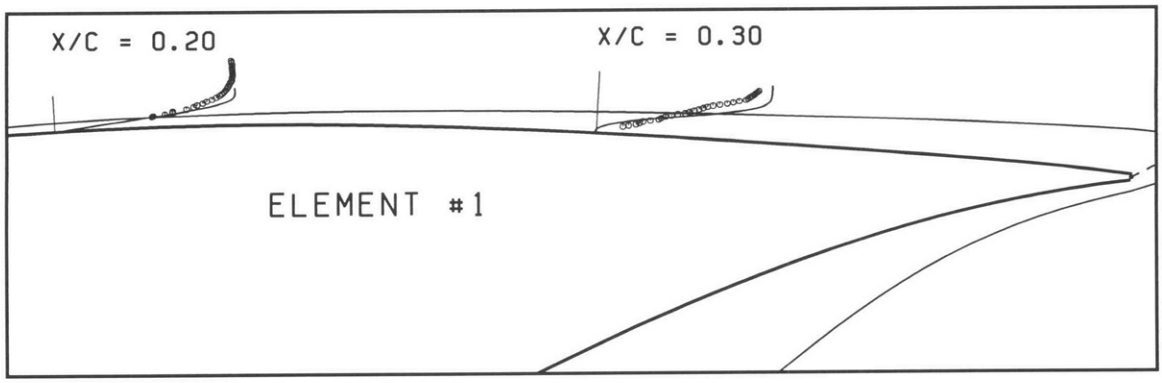

Figure 3-9: Mean streamwise velocity profiles (○) on Element #1 with MSES predictions (—). ($\Re = 1.8 \times 10^5$)

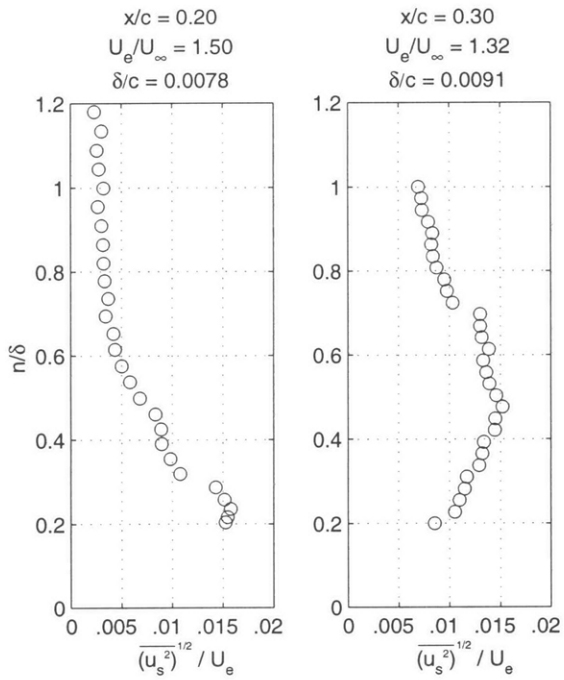

Figure 3-10: *RMS* streamwise velocity on Element #1 ($\Re = 1.8 \times 10^5$).

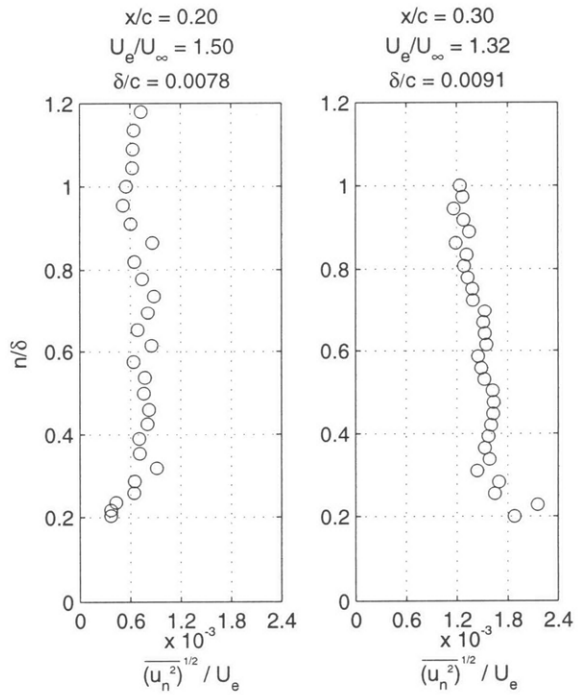

Figure 3-11: *RMS* normal velocity on Element #1 ($\Re = 1.8 \times 10^5$).

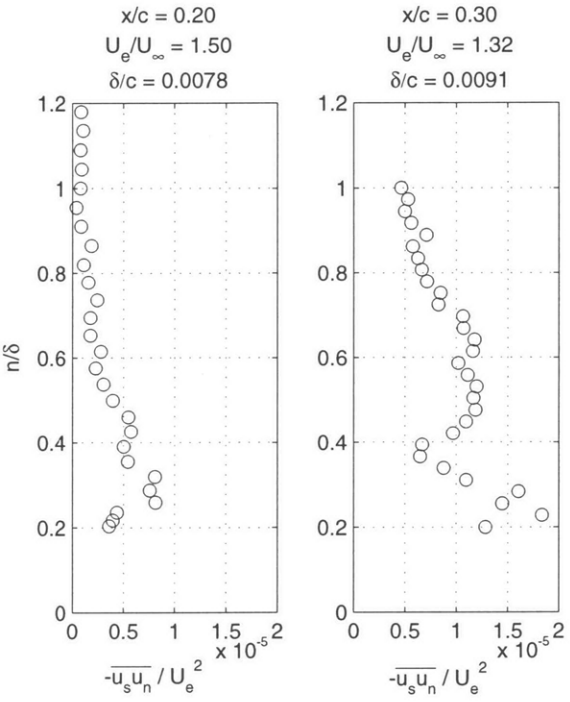

Figure 3-12: Reynolds shear stress on Element #1 ($\Re = 1.8 \times 10^5$).

3.2.3.2 Element #1 Wake and Element #2 Boundary Layer

Having a picture of the boundary layer conditions just before the trailing edge of the leading airfoil element, we can proceed to an examination of the mean velocities and turbulence quantities in the wake of Element #1 and the boundary layer of Element #2. Figures 3-13 and 3-14 show the five mean velocity profiles starting in the boundary layer of the second airfoil element and traversing through the wake of the first element. At $x/c = 0.40$ in Figure 3-13, we can see the jet-like effect of the gap as the velocity below $n/\delta \simeq 0.4$ reaches values substantially higher than the outer edge velocity. And to a lesser extent, the jet-like effect is also observable in the $x/c = 0.48$ profile. Several observations may be made looking at the mean cross-stream velocity of Figure 3-14. At $x/c = 0.40$, there is a large jump in the flow direction across the wake of the leading element. The lower portion of the plot shows the flow as relatively parallel to the surface of the second airfoil element while the flow in the upper portion is at a substantially different flow angle as the boundary layers from the top and bottom surfaces of the first airfoil element begin to merge. By the next measurement station, however, the normal velocity has already smoothed out. Farther downstream, the mean cross-stream velocity tends to continue to rise as opposed to approaching a final value indicating that the streamlines are drifting away from the airfoil surface. Also at the downstream profile locations, the streamwise velocity in the boundary layer of Element #2 appears to be stretching in the normal direction such that $\partial U_s/\partial n$ decreases from the near wake profiles illustrating the adverse pressure gradient developing over the second half of the airfoil.

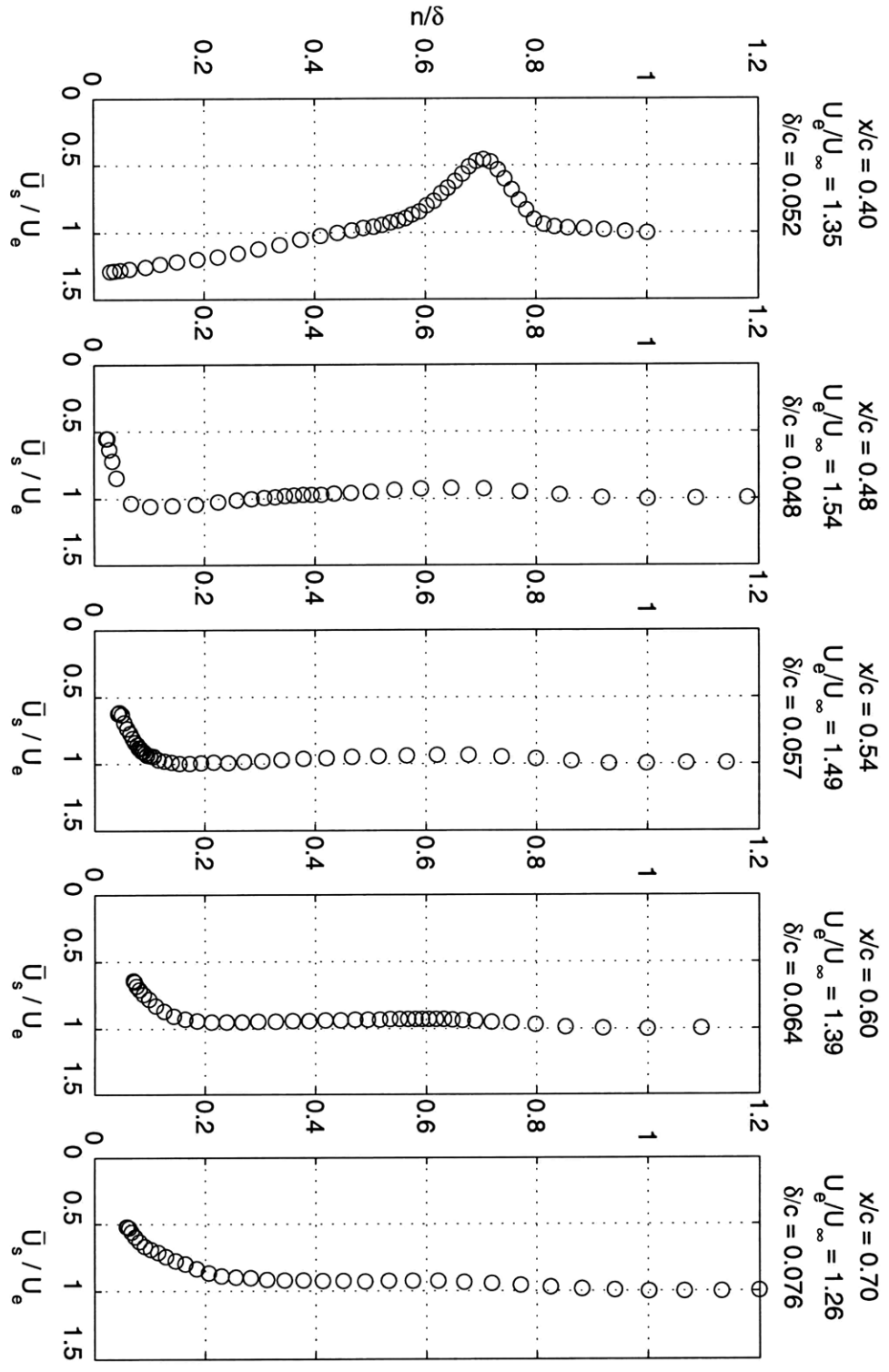

Figure 3-13: Mean streamwise velocity behind Element #1 ($\Re = 1.8 \times 10^5$).

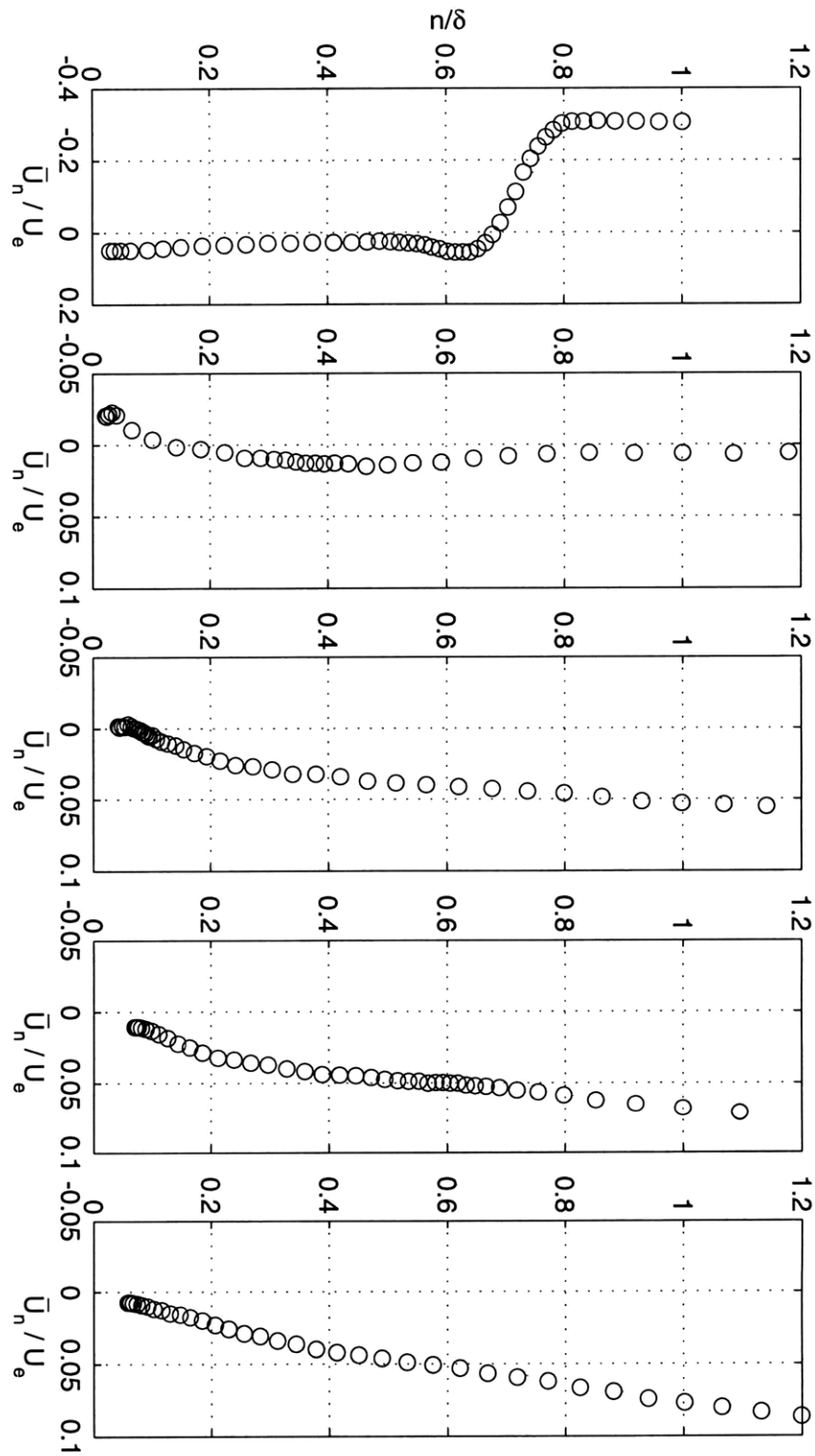

Figure 3-14: Mean normal velocity behind Element #1 ($\Re = 1.8 \times 10^5$).

We can also compare the measured streamwise velocities to those predicted by MSES as shown in Figures 3-15 and 3-16. There appears to be good agreement between the experimental data and the computational data toward the boundary layer of the second airfoil element in the near-wake cases of Figure 3-15. The computational model and the experimental data even appear to capture the same inviscid slope of the mean streamwise velocity on the lower portion of the $x/c = 0.40$ profile. The wake mixing, however, appears to be underestimated in the computational model as demonstrated by the noticeably flatter wake profile at $x/c = 0.48$. By the farther-wake profile locations of Figure 3-16 the computational model appears to overestimate the velocities in the region which may be due to the model's separate treatment of the shear layer as a wake and a boundary layer rather than the entire region as a confluent shear layer. Although MSES predicts a laminar separation bubble in the $x/c \simeq 0.50$ to $x/c \simeq 0.75$ range, the existence of such separation was not immediately evident in the velocity profile data. In fact, detection of such small laminar separation bubbles would prove difficult because of the prohibitive size of the cross-wire probe. Again, there exists the uncertainty in probe position as the initial location of the probe is not known with any degree of certainty. This means that we may be able to find a better match between the computational and experimental data simply by varying the distance from the airfoil surface to the first profile point.

In the examination of the turbulence quantities of $(\overline{u_s^2})^{\frac{1}{2}}$, $(\overline{u_n^2})^{\frac{1}{2}}$, and $-\overline{u_s u_n}$ in Figures 3-17, 3-18, and 3-19, we can observe many typical features of curved shear layers as well as several features of interest as predicted by the computational model. While high in the near-wake region (upwards of 15% of U_e), the *rms* velocities decay rapidly farther downstream (to approximately 5% of U_e) and become spread out across the entire shear layer. Similarly, the Reynolds shear stress exhibits a strong rate of decay as well as the smearing across the entire shear layer. By the final profile location hardly any large normal gradients of the plotted quantities can be observed implying the confluence of the shear layers into almost one large boundary layer.

As expected, the turbulence intensities are larger in magnitude on the inside of curved wake than on the outside since the streamwise curvature of the inside portion

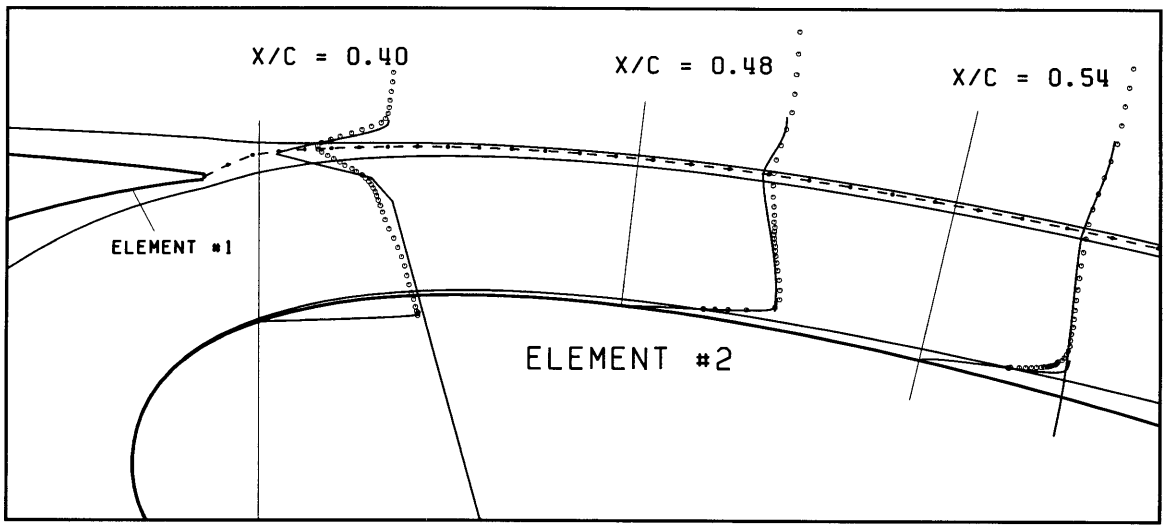

Figure 3-15: Near-wake mean streamwise velocity profiles (o) behind Element #1 with MSES predictions (—). ($\Re = 1.8 \times 10^5$)

is a destabilizing concave while the outside is a stabilizing convex. This result is consistent with earlier airfoil experiments such as those of Adair and Horne[2] and Ramjee et al.[19] as well as the more recent work of Weygandt and Mehta[23] and Absil and Passchier[1]. Although Adair and Horne[2] found that the wake and boundary layer remain distinct shear layers downstream of the second airfoil, the differences in experimental set-up itself may account for the discrepancy. The present experiment uses airfoil elements of similar size with the leading element smaller than the trailing whereas Adair and Horne[2] utilized a more realistic main element – single-slotted flap arrangement. The considerable difference in size of their airfoil elements produced a much larger gap blowing effect creating a stronger and more distinct inviscid region between the shear layers. These observations of higher turbulence intensities on the concave side of the wake and lower turbulence intensities on the convex side are also consistent with curved boundary layer studies such as those of Hoffmann et al.[13] and Muck et al.[17].

In addition to qualitative similarities of the data to previous experimental evidence, we can also observe flow phenomena predicted by MSES. For example, MSES predicts a large region of separated flow on the lower surface of the leading airfoil element as shown in Figure 3-5. Evidence of this region can be seen in the plots

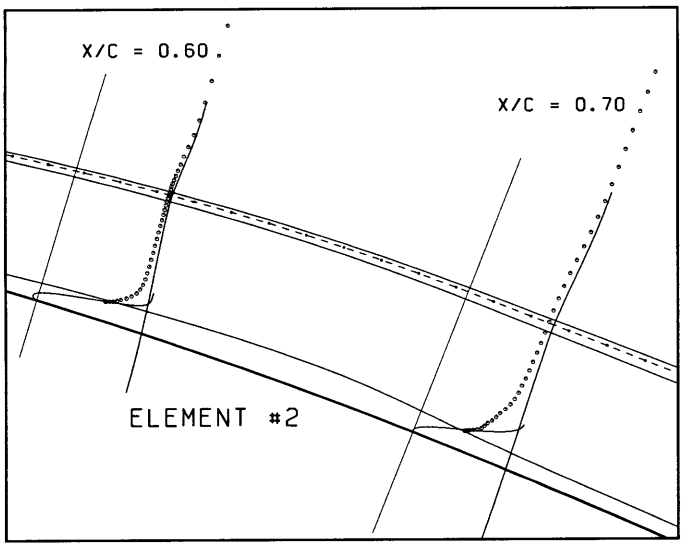

Figure 3-16: Farther-wake mean streamwise velocity profiles (o) behind Element #1 with MSES predictions (—). ($\Re = 1.8 \times 10^5$)

of turbulence quantities at $x/c = 0.40$. Local maxima of $(\overline{u_s^2})^{\frac{1}{2}}$, $(\overline{u_n^2})^{\frac{1}{2}}$, and $-\overline{u_s u_n}$ at $n/\delta \simeq 0.45$ (which does not correspond to the wake center as can be seen from Figure 3-13) indicate an area of high mixing in a region that is supposed to be inviscid. This seeming contradiction points toward a flow phenomenon upstream of the first wake profile and on the lower surface of the leading airfoil element. A region of separated flow at $x/c \simeq 0.35$ on the lower surface of the leading airfoil element as discussed in Section 3.2.1 would provide just such downstream evidence. This high mixing region in the ideally inviscid "gap jet" would also serve to flatten out the wake faster than may have been predicted. As we can see from the high rms normal velocity, $(\overline{u_n^2})^{\frac{1}{2}}$, at $x/c = 0.40$ in Figure 3-18, the fluctuations are actually higher in the convecting separated region (at $n/\delta = 0.45$) than in the wake itself ($n/\delta = 0.70$). This result indicates that higher momentum fluid from the "gap jet" and lower momentum fluid from the wake are being mixed at a high rate which would tend to smear out the velocity profiles quickly into one larger viscous region. By the next measurement station (at $x/c = 0.48$), even the turbulence intensities show little sign of a distinct region corresponding to the once separated flow.

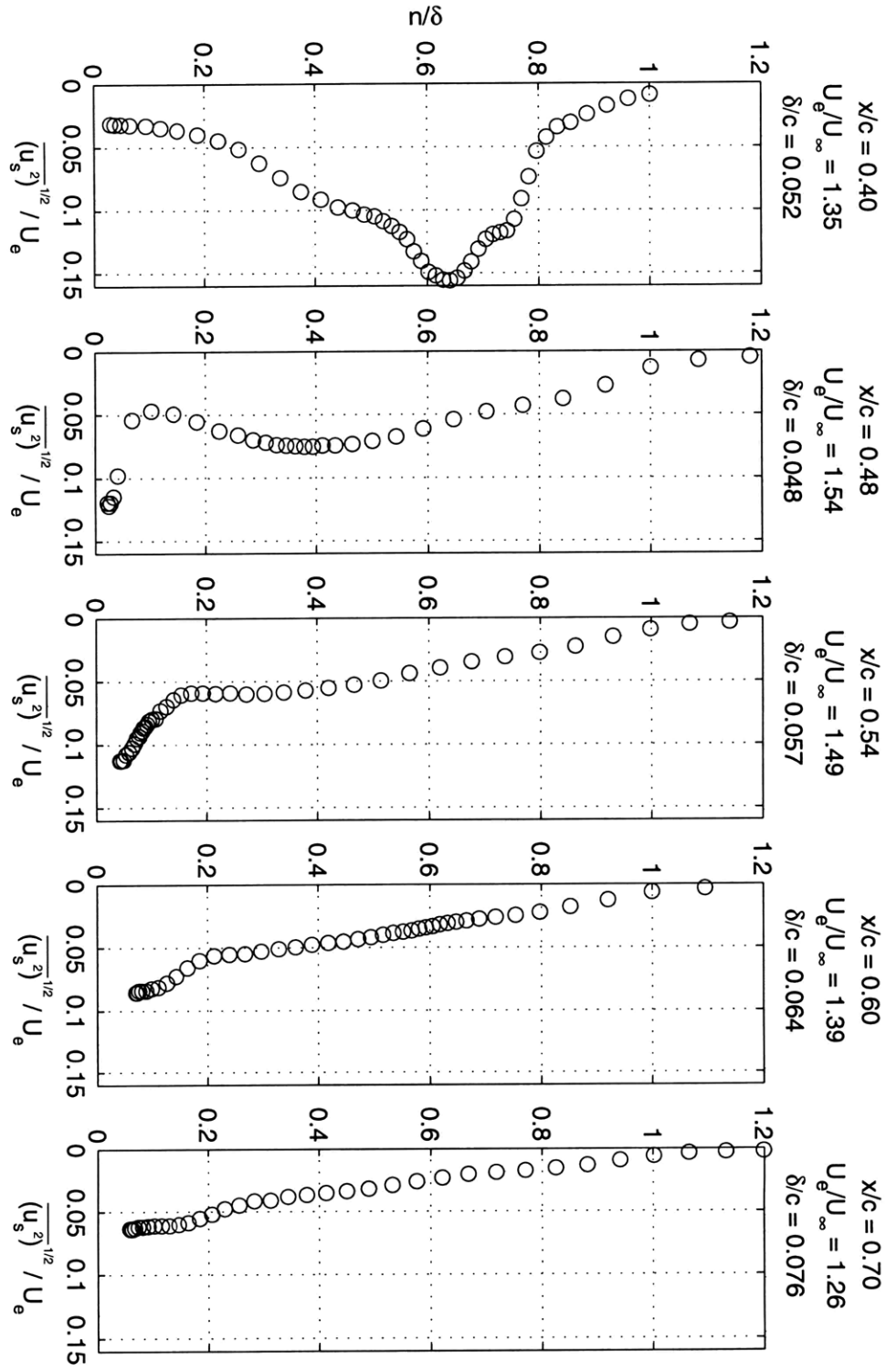

Figure 3-17: *RMS* streamwise velocity behind Element #1 ($\Re = 1.8 \times 10^5$).

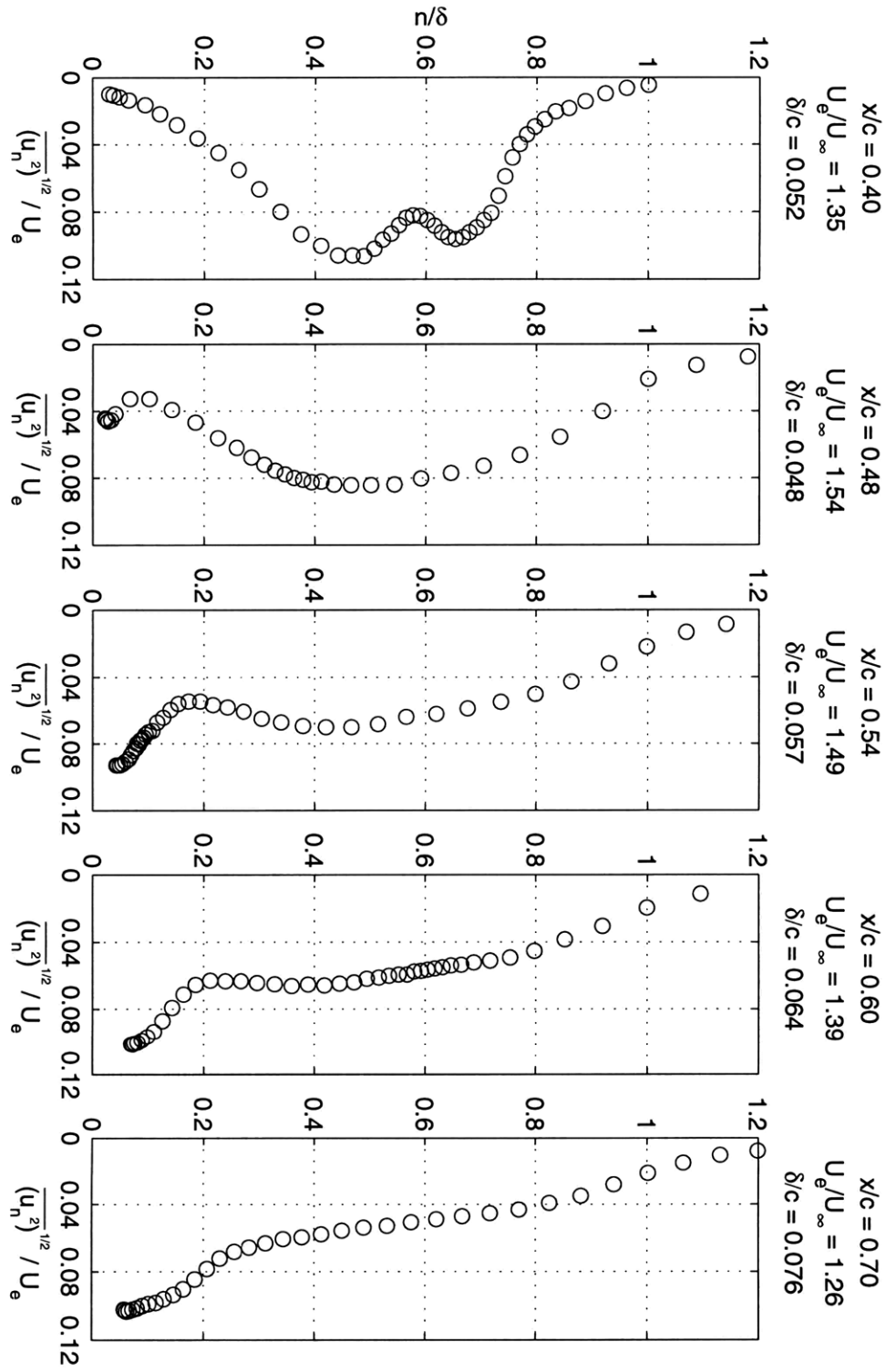

Figure 3-18: *RMS* normal velocity behind Element #1 ($\Re = 1.8 \times 10^5$).

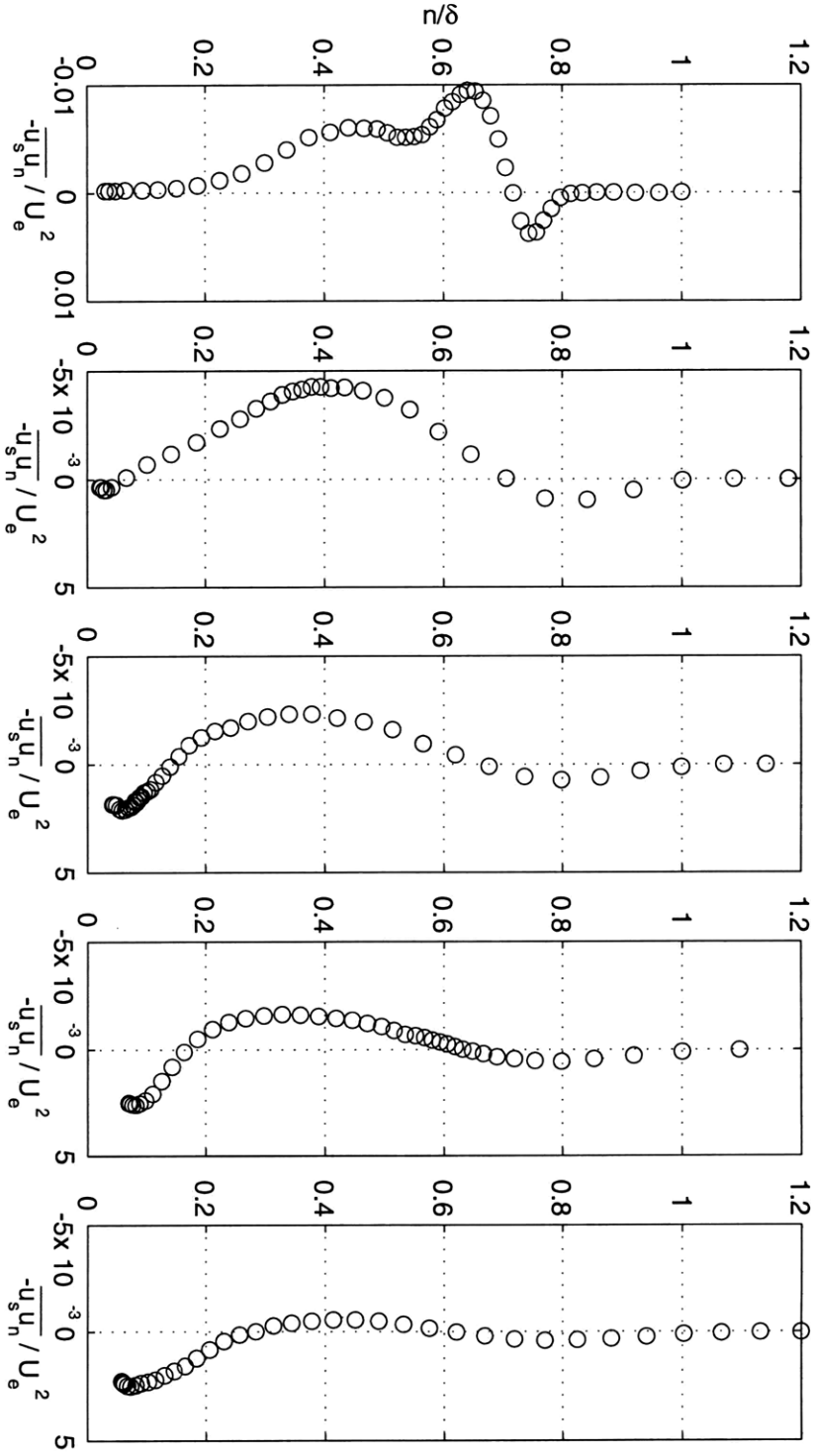

Figure 3-19: Reynolds shear stress behind Element #1 ($\Re = 1.8 \times 10^5$).

3.2.4 Wake Reynolds Shear Stress Comparison

Having an overall picture of the flow over the suction side of the airfoil surface, we may compare the experimental Reynolds shear stress data to that of the computational model. In order to compare similar quantities, however, we must examine and reconcile the non-dimensionalization used both in the experiment and in the computational model. The experimental Reynolds shear stress data, $-\overline{u_s u_n}$, in Section 3.2.3.2 was non-dimensionalized by the outer edge velocity of the wake while the computational model uses a Reynolds shear stress coefficient, $\sqrt{C_\tau}$, as defined by Equation 3.1 to capture the product of the streamwise and cross-stream velocity fluctuation information.

$$\sqrt{C_\tau} = \frac{\pi}{4} \frac{\sqrt{|-\overline{u_s u_n}|_{max}}}{U_e} \tag{3.1}$$

MSES, therefore, tracks the value of $\sqrt{C_\tau}$ for both the upper and the lower portions of the wake with the difference between the two serving as a measure of the wake asymmetry. In so doing, MSES actually tracks the maximum value of $|-\overline{u_s u_n}|$. To compare this tracking of $|-\overline{u_s u_n}|_{max}$ to the experimental data, we must compute the experimental $\sqrt{C_\tau}$ for both the upper and the lower portion of the wake. One important ambiguity arises: which edge velocity, U_e, to use? First, we must choose whether to compare the actual values of $\sqrt{C_\tau}$ or the measure of the velocity fluctuations, $-\overline{u_s u_n}$. We have decided to compare the fluctuations since the edge velocities have, in effect, been compared in the previous section. To compare the fluctuation quantities as opposed the actual values of $\sqrt{C_\tau}$, the same non-dimensionalizing edge velocity should be used. Therefore, we can either use the edge velocity of the experiment or the edge velocity of the MSES model. Since the MSES data is a continuous curve while the experimental data is simply ten points, the more convenient choice is to use the MSES edge velocity to ease the conversion of the data. Figure 3-20 shows the MSES predicted edge velocity ratios (U_e/U_∞) for the leading element with the diamonds ($\diamond$) representing the edge velocity used for the non-dimensionalization of the experimental data. These MSES edge velocity ratios at the experimental profile locations are also summarized in Table 3.2.

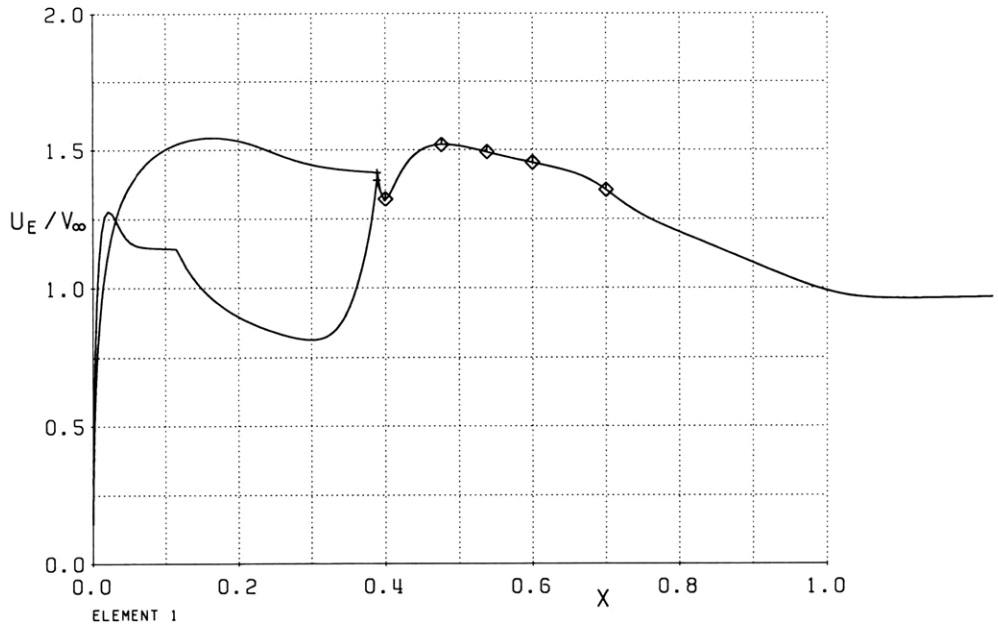

Figure 3-20: MSES edge velocity in wake of Element #1 ($\Re = 1.8 \times 10^5$).

x/c	0.40	0.48	0.54	0.60	0.70
U_e/U_∞	1.322	1.518	1.492	1.454	1.355

Table 3.2: MSES edge velocities for $\Re = 1.8 \times 10^5$.

After locating the maximum values of $|-\overline{u_s u_n}|$ on both sides of the wake, the above values of U_e/U_∞ are used in conjunction with Equation 3.1 to compute the experimental values of $\sqrt{C_\tau}$. These experimental values of $\sqrt{C_\tau}$ are shown in Figure 3-21 along with the predicted MSES curves from which initial shear layer conditions and wake asymmetry observations may be made. Although the general trends of decreasing $\sqrt{C_\tau}$ and similar wake asymmetry ($\sqrt{C_\tau}|_{top} < \sqrt{C_\tau}|_{bot}$) hold true in both cases, a more quantitative examination reveals several likely MSES shortcomings.

First, MSES drastically overestimates the initial $\sqrt{C_\tau}$ on the upper surface of the leading element trailing edge (at the transition location of the upper surface) while somewhat underestimating the near wake $\sqrt{C_\tau}$ on the lower portion of the wake. Since the flow is predicted to be laminar on the upper surface of the leading element up until the trailing edge and the wake is always computed as turbulent, the poor initial

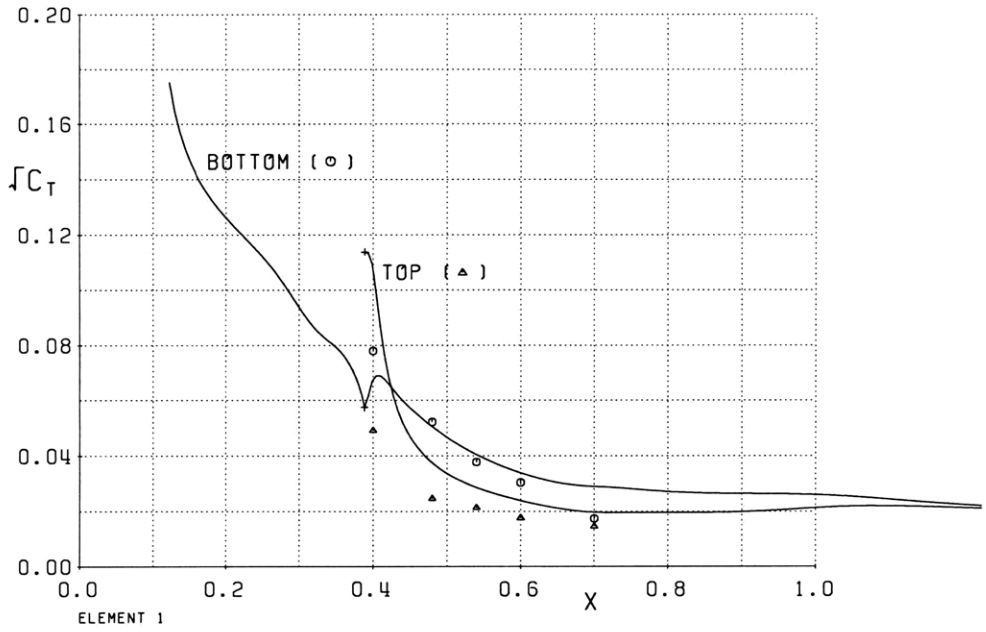

Figure 3-21: Reynolds shear stress coefficient in wake of Element #1 ($\Re = 1.8 \times 10^5$).

$\sqrt{C_\tau}$ prediction may be caused by the shear layer being forced to transition instantaneously at the trailing edge without benefit of any upstream transition mechanism or turbulent history development. In fact, just behind the trailing edge of Element #1, the computational model predicts the reverse asymmetry with the convex side having the higher fluctuations. The lower portion of the wake, however, does have a prior turbulent history which may allow the predicted initial $\sqrt{C_\tau}|_{bot}$ to be much closer to the detected $\sqrt{C_\tau}|_{bot}$ at the beginning of the wake.

Fortunately, the experimental and computational near-wake $\sqrt{C_\tau}$ of the destabilizing, concave side are close in value since flow re-organization in such shear layers[13] tends to place a higher importance on the flow history. The rate of decay of the concave portion of the wake, however, is visibly higher in the experimental data than in the computational data eventually (by $x/c = 0.70$) leading to practically the same $\sqrt{C_\tau}$ for the top and bottom of the wake. Meanwhile, the attenuation of turbulence history[17],[10] in stabilizing, convex curvature flow contributes to the decreasing difference between computational and experimental $\sqrt{C_\tau}|_{top}$ as the rates of decay even begin to match beyond $x/c \approx 0.5$.

In addition to the differences in initial wake conditions, there are also discrepancies between the computational and experimental data in the degree of wake asymmetry as measured by the difference between $\sqrt{C_\tau}|_{top}$ and $\sqrt{C_\tau}|_{bot}$. While MSES predicts a nearly constant difference in $\sqrt{C_\tau}$ for $0.48 < x/c < 0.70$, the experimental data shows an initially much larger difference and then a continuously decreasing $\Delta\sqrt{C_\tau}$ until the two values are nearly identical at the last measurement station. It is difficult to compare the measured values of $\sqrt{C_\tau}$ at the farther wake locations to the MSES values because the downstream $\sqrt{C_\tau}$ values are likely affected by the confluence of the boundary layer of Element #2 which is not accounted for in MSES. However, an examination of the near-wake profile stations (unaffected by the shear layer confluence) reveals an inadequate computational representation of the degree of wake asymmetry.

The main discrepancies between the computational model and the experimental data begin with a substantial mismatch of initial Reynolds shear layer coefficient. Although the general trends are consistent between the two methods, the decay rate of $\sqrt{C_\tau}|_{bot}$ is considerably different from the observed to the computed which may be accounted for by the presence of the confluent boundary layer. Finally, the degree of wake asymmetry appears to be underestimated by MSES implying the inadequate computational modeling of the streamwise curvature effects. It must also be noted that although the exact accuracy of the comparison to computational results is not known due to the unknown effects of the 3-dimensionality of the flow, comparisons to lift coefficients of up to 10% higher did not show any significant variation of data nor did they show any change in the resulting conclusions.

3.2.5 Near-Wake Reynolds Number Comparison

In addition to comparing the experimental data to computational models, we can also compare the data shown above ($\Re = 1.8 \times 10^5$) to the lower Reynolds number ($\Re = 1.4 \times 10^5$) data shown in parallel in Appendix C. Rather than comparing all of the velocity data at all of the velocity profiles, we will instead focus on the most interesting profile location, $x/c = 0.40$. This near-wake velocity profile illustrates the various flow features observed in the experiment and contains some of the most

complex flow phenomena including the convection of the separated region from the lower surface of the first airfoil element and the high degree of wake asymmetry. For a more complete picture of the flows at the two Reynolds numbers, a comparison of $\sqrt{C_\tau}$ in the wake of the leading element is presented as well.

The mean and root-mean-square data for both the streamwise and normal velocities are non-dimensionalized as described in Section 3.2.2 and presented in Figure 3-22. The figure is simply the overlay of data from Figures 3-13, 3-14, 3-17, and 3-18 with the corresponding plots (Figures C-8, C-9, C-13, and C-14) found in Appendix C. Similarly, the Reynolds shear stress profiles are shown in Figure 3-23 as the overlaying of data from Figures 3-19 and C-15.

Although the arrangement of profile data points could have been better chosen in terms of concentration in the airfoil wake, the data sets in all of the plots in Figures 3-22 and 3-23 very nearly appear to collapse onto the same curve. One distinction between the two Reynolds number cases appears in the turbulence quantities in the region corresponding to the once separated flow on the lower surface of the leading airfoil element as discussed in Section 3.2.3.2. Not surprisingly, the lower Reynolds number case exhibits stronger turbulence intensities in the formerly separated region ($n/\delta \approx 0.45$). Since lower Reynolds flows typically exchange fluid momentum less efficiently, it is expected that the flow would separate sooner and the separation region would be larger as compared to their higher Reynolds number counterparts. This flow characteristic can be seen in the C_p and streamline plots found in Figure 3-5 and the corresponding lower Reynolds number plot in Figure C-1. It also follows that the larger separated region would also contain more violent mixing characteristics as exhibited by higher fluctuation quantities of $(\overline{u_s^2})^{\frac{1}{2}}$, $(\overline{u_n^2})^{\frac{1}{2}}$, and $-\overline{u_s u_n}$. With the exception of a higher $(\overline{u_s^2})^{\frac{1}{2}}$, this expected result is present in the current comparison.

To provide an overall picture of the sensitivity of the flow to Reynolds number variation, we examine the streamwise development of the Reynolds stress coefficient $\sqrt{C_\tau}$ non-dimensionalized in the manner described in Section 3.2.4. Figure 3-24 shows the experimental data from Figure 3-21 together with the corresponding lower Reynolds number experimental data from Figure C-17. With the exception of the first point

at $x/c = 0.40$, the values of $\sqrt{C_\tau}$ on the convex side of the wake all practically fall on top of each other. The lack of agreement at the first point may be attributed to the poor concentration of profile points as the data may not have captured the true maximum magnitude of the Reynolds shear stress, $|-\overline{u_s u_n}|_{max}$, on the outer portion of the wake. The other possible discrepancy between the two Reynolds number flows may be the slightly faster decay rate of the concave $\sqrt{C_\tau}$ of the lower Reynolds number case as can be seen at the last two measurement stations. This is likely due to the more advanced stages of confluence of the boundary layer with the wake at the lower Reynolds number.

All in all, the two Reynolds number cases compare quite favorably to each other with no inexplicable discrepancies. The comparison in this section of the near-wake profile and the overall wake $\sqrt{C_\tau}$ data provides the confidence necessary to accept the previously presented experimental results as at least repeatable and consistent.

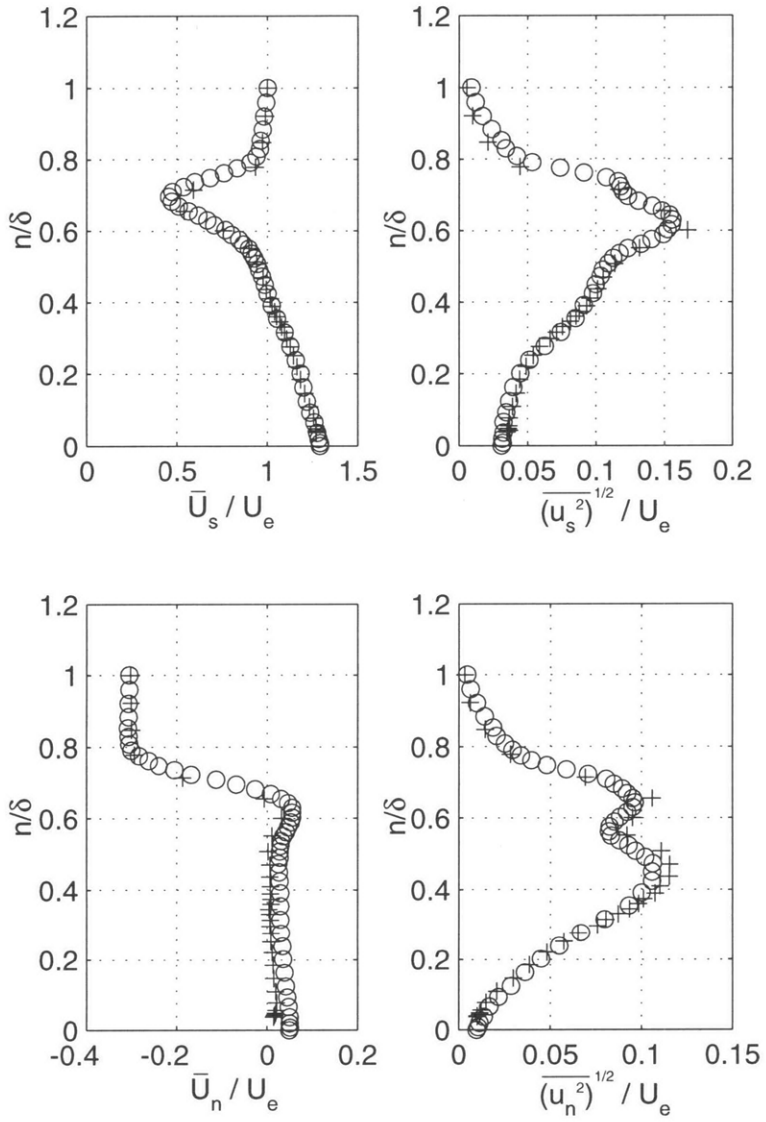

Figure 3-22: Comparison of mean and *rms* velocities for $\Re = 1.4 \times 10^5$ (+) and $\Re = 1.8 \times 10^5$ ($\circ$) at $x/c = 0.40$.

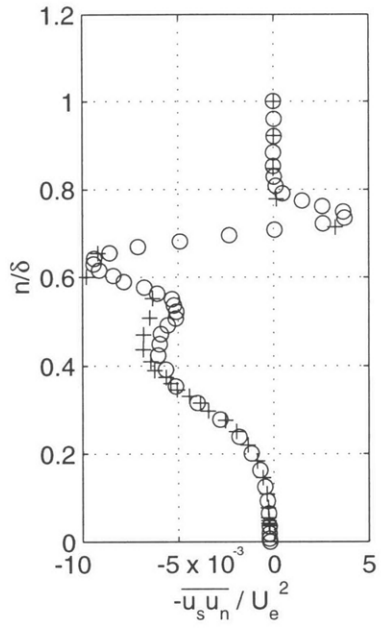

Figure 3-23: Comparison of Reynolds shear stress for $\Re = 1.4 \times 10^5$ (+) and $\Re = 1.8 \times 10^5$ (○) at $x/c = 0.40$.

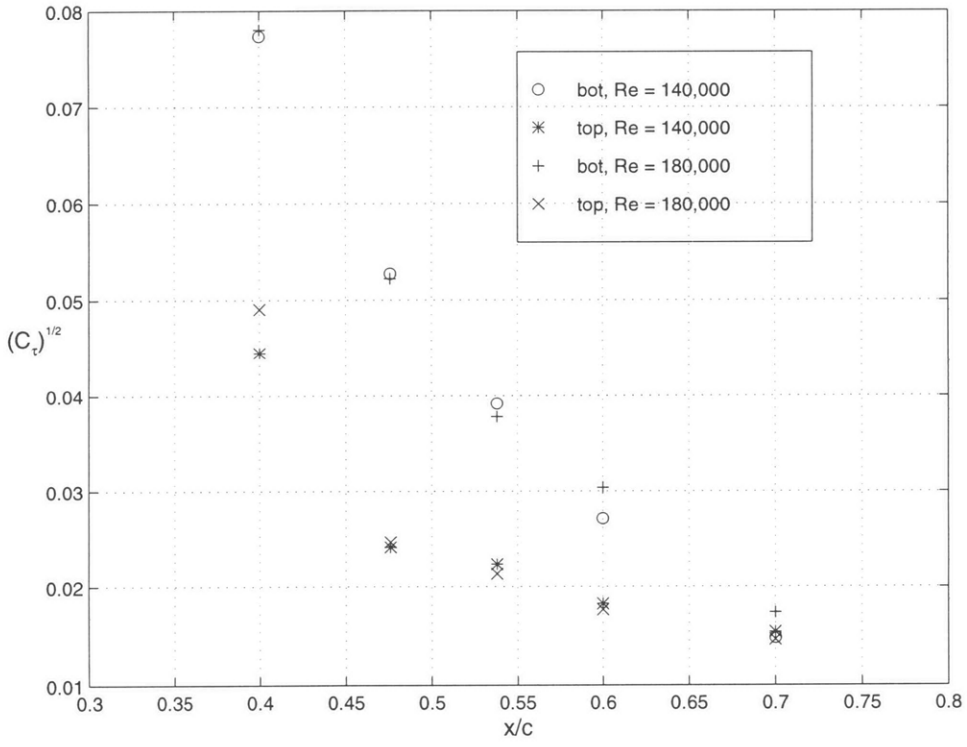

Figure 3-24: Comparison of Reynolds shear stress coefficient in wake behind Element #1.

Chapter 4

Future Work and Conclusions

4.1 Future Work

To improve and to expand on the current experimental data, several recommendations are made for future work including improvements to the experimental hardware and additional experimental runs and conditions. Ideally, both the additional experimental runs and the hardware improvements would include an increase of the flow Reynolds number out of the currently marginal range. Since the current database is limited to only two Reynolds numbers at only one angle of attack, suggestions for computational model improvements would be premature at this time and are, therefore, not explored.

4.1.1 Improvements in Experimental Set-up

Recommendations for experimental set-up modifications are primarily geared toward the improvement of the quality of the data, toward more efficient experimental procedures, and toward raising the upper limit on experimental Reynolds numbers. It must be reiterated that the limit on the experimental Reynolds number arises from requirement that the cross-wire be calibrated up to the highest expected experimental velocities (occurring on the upper surface of one of the airfoil elements). Improvements are proposed for all of the systems involved in the experimental set-up including the

low-turbulence wind tunnel facility, the data acquisition system, the multi-element airfoil, the support system, and the cross-wire system of Sections 2.1, 2.2, 2.4, 2.5, and 2.6, respectively.

The simplest way to raise the experimental Reynolds number is to modify the low-turbulence wind tunnel. Specifically, two things can be done to raise the maximum hot-wire calibration velocity. First, an additional, larger diffuser section may be installed behind the fan motor to more efficiently slow the exit flow. A more economical alternative may be a method of uniformly increasing the local velocity at the cross-wire and pitot probes to accomplish the same end of calibrating the cross-wire probe at higher flow velocities. A common version of the latter is a jet installed in the wind tunnel test section during hot-wire calibration and later removed during testing.

Although improvements to the data acquisition system do not directly impact the quality of the data, a more efficient means of data collection limits the total run time which may avoid possible drift errors. If the voltage data is to be converted into velocity data and subsequently velocity statistics during the experimental runs as opposed to storing all of data points, then an upgrade in the computer hardware is recommended. Simply by switching from the existing 486-based (16 MB RAM) computer to a newer, modestly priced 586-based (24 MB EDO RAM) computer, the computational processing time associated with the typical 32,000 point data block would be cut by 73%. Since the data reduction time is the main driving force behind the extensive time (currently 2 minutes) involved per profile data point, the above gains in computational efficiency would cut the typical 45-point profile data collection time from 90 minutes to 24 minutes allowing substantially more expedient velocity profile measurements. In fact, the data obtained using an upgraded computer would be nearly continuous since the data digitization and reduction are done in parallel and would be performed in nearly the same time frame (24 seconds vs. 26 seconds). By upgrading further, the data reduction time can be reduced below the digitization time to limit the discontinuity of data to the transfer time from the A/D board to the computer memory.

The airfoil assembly itself may be modified to improve the quality of the data and

to limit the unknowns involved. First, larger end-plates may limit possible spanwise leakage and may increase the 2-dimensionality of the flow. To limit spanwise smearing of the airfoil wake for drag calculation, "phantom" end-plates may be attached to the sides of test section to provide boundary layer dumping capability from the airfoil end-plates onto the "phantom" end-plates rather than allowing the wake to spread to the entire width of the test section. This option must be further studied to examine other, potentially detrimental side effects. Another possible improvement to the airfoil assembly is more precise machining of end-plate holes to provide more precise airfoil positioning. Finally, the boundary layer may be artificially tripped on the upper surface of the leading airfoil to provide a turbulent initial condition (and, therefore, less spanwise flow variation) for the wake development.

As far as the airfoil support system is concerned, several improvements may be made with respect to more precise angle of attack adjustment and to more accurate and efficient load measurement as well as to a general structural stiffening of the entire system. First, the hysteresis noted in Section 2.5.1 may be curtailed by stiffening the pieces supporting the stepper motor. The load measurement system may be improved by improving the accuracy and efficiency of the calibration of the system. Ideally, the calibration of the system would be performed with the airfoil mounted on the shaft avoiding any errors due to motion of the entire assembly with respect to the load cells during airfoil mounting and dismounting. Together with a new calibration tool, a more accurate calibration matrix may be created by focusing on the neighborhood of predicted loads. In general, the system would likely benefit from some form of support (presumably with additional load cells) at the cantilevered end of the mounting shaft in order to increase the system's natural frequency and to further reduce the vibrational amplitudes.

Finally, the cross-wire system may also be improved by more efficient resource management. The probe itself caused many significant problems and delays because of the difficulty of hot-wire re-attachment. This problem may be overcome by an attachment method less sensitive to wire-prong relative position such as soldering. Also, by simply building more probes, the investigator may practically guarantee a

functioning cross-wire probe at all times assuming that a secure method of storing the probes exists. As in the case of the load measurement system, a calibration method involving the presence of the airfoil in the wind tunnel would increase the efficiency of the experimental procedure and would avoid the errors due to motion relative to the load cells. A method of measuring the actual distance from the probe to the airfoil surface would avoid the unknown of position offset in the velocity profiles. One such possible method might be to connect the aluminum airfoil and an extension from one of the prongs in some form of electrical circuit so that when the extension contacts the airfoil surface, the circuit closes and triggers a switch turning the motors off and noting the current probe position and the known distance from the surface.

Clearly, this experimental set-up is not in optimal condition for airfoil testing but it is also quite feasible to dramatically improve the hardware efficiency and accuracy. More difficult but not impossible, however, is achieving the desired higher Reynolds number flows.

4.1.2 Additional Experimental Testing

Considerably more experimental runs are required in order to build up a useful database on the interaction of wakes and boundary layers in multi-element airfoils. Ideally, most of these additional runs would be performed at more realistic Reynolds numbers since the current Reynolds numbers are marginal for the study of wake–boundary layer interaction. Higher Reynolds numbers would not only provide more realistic results but would also avoid some of the pitfalls associated with extensively laminar flow such as streamwise vortical structures and laminar bubbles.

However, before any more experimental data may be obtained, the degree of 2-dimensionality of the flow must be investigated and any significant deviations must be accounted for. Not only is the 2-dimensionality of the flow important to the local uniformity at the spanwise location of the velocity profiles but the degree of 2-dimensionality also affects the matching conditions in terms of α, C_L, and C_D applied to the computational model for outer flow data comparisons. An idea of the 2-dimensionality of the experimental set-up may be obtained by using a single-wire

probe with the standard X-Y-Z traverse to investigate the entire flow-field around (or at least behind) the airfoil assembly and to compare the resulting velocity field across spanwise locations.

Once either the 2-dimensionality of the flow is verified or the 3-dimensionality is accounted for, the following additional experimental runs are recommended be performed. First, additional streamwise profile locations should be added to include at least one more position on the second airfoil element as well as one location behind the trailing edge of the airfoil assembly. Also, profiles should be taken at several locations on the opposite (pressure) side of the airfoil, especially on the leading element to gain a better understanding of the initial "gap jet" conditions including the verification of a region of separated flow. These additional profile locations provide a better overall picture of the flow which is necessary for a better understanding of the flow specifics at each test condition.

To complete the experimental database, additional angles of attack must be studied to determine the quantitative effects of the various pressure gradients created by the airfoil system. It is recommended that an additional five angles of attack be added to the database including one near $C_{L_{max}}$. Also, to capture the Reynolds number effects, at least two but preferably three freestream velocities should be included in a comprehensive experimental database.

Finally, the construction of the leading airfoil element out of two pieces as described in Section 2.4 allows for the examination of a more realistic leading edge device with pronounced flow separation in the cove region. The entire database would ideally be repeated for this "cove configuration". However, with a comprehensive database of the "whole" leading element configuration in hand, it is likely that the flow behavior due to the separated region in the cove would be understood after a handful of test conditions.

4.2 Conclusions

The major goal of the present work, the development of a multi-element airfoil wind tunnel testing system, has been met with encouraging results. Although the system in its current configuration appears to suffer from a number of low-Reynolds number effects, the early data still appears to be promising in its qualitative agreements with previous experiments and current computational models. Several important preliminary results have been found which would lead to modifications in the computational model for better wake curvature and wake asymmetry modeling along with improved shear layer confluence representation in MSES. The preliminary data suggest that the computational model does not adequately predict the initial Reynolds shear stress coefficient at the transition location nor does it adequately represent the wake asymmetry.

The test system development included the design, construction, testing, and validation of both the airfoil support system and the cross-wire probe system. The total system has been used to study the interaction between the wake of the leading airfoil element and the boundary layer of the trailing element through the measurement of velocity profiles at seven streamwise locations along the upper surface of the airfoil including two beginning at the leading element surface and five from the trailing element surface.

Although several additional steps are recommended be taken to optimize the test system as discussed in Section 4.1, the preliminary data obtained using the existing set-up are self-consistent and repeatable if not completely accurate. Clearly, however, many more velocity profiles at numerous other testing conditions must be obtained to create a comprehensive database for computational model modification and validation.

In the long term, new airfoils may be tested using the same facility to focus on additional flow features. In fact, much of the experimental set-up may be moved to other facilities for additional testing. This current wind tunnel test-bed may provide the necessary groundwork for a comprehensive small airfoil hot-wire testing program

to study any number of flow features in addition to the wake – boundary layer interactions of the current research.

In terms of the real-world application to the analysis and design of high-lift airfoil systems for large aircraft, the understanding of interactions between leading element wakes and trailing element boundary layers is an important piece in efficient and accurate modeling of the complex flows involved and subsequent model use in industrial airfoil design applications. Improvements in high-lift system design would then lead to lighter, more efficient wings, thereby, improving the overall aircraft design.

Appendix A

Airfoil Coordinates

Element #1:

x/c	y/c	x/c	y/c	x/c	y/c
0.388807	0.097857	0.036924	0.055291	0.074760	-0.024333
0.385040	0.098364	0.030949	0.050735	0.083864	-0.022423
0.378667	0.099154	0.025596	0.046178	0.093536	-0.020092
0.371285	0.099945	0.020849	0.041656	0.103677	-0.017352
0.362748	0.100732	0.016684	0.037200	0.114182	-0.014225
0.352977	0.101552	0.013071	0.032837	0.124949	-0.010734
0.342056	0.102421	0.009976	0.028586	0.135904	-0.006901
0.330238	0.103321	0.007364	0.024463	0.146997	-0.002741
0.317844	0.104206	0.005197	0.020479	0.158205	0.001729
0.305162	0.105029	0.003440	0.016642	0.169518	0.006492
0.292391	0.105746	0.002063	0.012956	0.180939	0.011533
0.279647	0.106325	0.001038	0.009423	0.192474	0.016835
0.266993	0.106738	0.000344	0.006046	0.204134	0.022378
0.254455	0.106963	-0.000035	0.002825	0.215924	0.028136
0.242047	0.106984	-0.000105	-0.000236	0.227842	0.034074
0.229771	0.106787	0.000127	-0.003130	0.239861	0.040139
0.217630	0.106359	0.000651	-0.005843	0.251898	0.046242
0.205625	0.105689	0.001473	-0.008438	0.263815	0.052258
0.193757	0.104768	0.002613	-0.011007	0.275509	0.058082
0.182029	0.103588	0.004083	-0.013512	0.286924	0.063636
0.170449	0.102142	0.005901	-0.015913	0.298024	0.068855
0.159025	0.100424	0.008071	-0.018172	0.308784	0.073688
0.147769	0.098431	0.010601	-0.020249	0.319176	0.078090
0.136698	0.096160	0.013495	-0.022109	0.329171	0.082026
0.125833	0.093611	0.016755	-0.023731	0.338736	0.085469
0.115203	0.090788	0.020383	-0.025102	0.347833	0.088407
0.104842	0.087695	0.024395	-0.026216	0.356421	0.090844
0.094790	0.084341	0.028815	-0.027063	0.364451	0.092806
0.085090	0.080736	0.033680	-0.027636	0.371875	0.094340
0.075787	0.076898	0.039033	-0.027933	0.378659	0.095506
0.066931	0.072850	0.044922	-0.027934	0.384792	0.096370
0.058569	0.068626	0.051399	-0.027604	0.388532	0.096807
0.050755	0.064267	0.058512	-0.026908		
0.043530	0.059811	0.066297	-0.025824		

Element #2:

x/c	y/c	x/c	y/c	x/c	y/c
0.999237	-0.143755	0.487314	0.069180	0.478298	-0.017004
0.995186	-0.141350	0.473711	0.070875	0.494926	-0.021559
0.988280	-0.137275	0.461086	0.072007	0.512304	-0.026174
0.980189	-0.132539	0.449519	0.072606	0.530192	-0.030796
0.970709	-0.127045	0.439033	0.072714	0.548428	-0.035386
0.959702	-0.120735	0.429595	0.072375	0.566905	-0.039934
0.947174	-0.113648	0.421133	0.071632	0.585559	-0.044437
0.933301	-0.105917	0.413559	0.070526	0.604354	-0.048899
0.918383	-0.097738	0.406784	0.069103	0.623264	-0.053328
0.902735	-0.089306	0.400731	0.067395	0.642271	-0.057735
0.886612	-0.080773	0.395338	0.065409	0.661356	-0.062130
0.870185	-0.072243	0.390564	0.063135	0.680491	-0.066524
0.853563	-0.063777	0.386387	0.060566	0.699636	-0.070921
0.836810	-0.055409	0.382814	0.057696	0.718759	-0.075330
0.819966	-0.047163	0.379858	0.054547	0.737854	-0.079760
0.803064	-0.039057	0.377519	0.051176	0.756926	-0.084217
0.786122	-0.031110	0.375802	0.047651	0.775979	-0.088702
0.769146	-0.023335	0.374669	0.044033	0.795009	-0.093212
0.752137	-0.015742	0.374018	0.040234	0.814006	-0.097748
0.735097	-0.008337	0.373885	0.036277	0.832951	-0.102305
0.718028	-0.001128	0.374370	0.032230	0.851811	-0.106875
0.700938	0.005874	0.375575	0.028188	0.870514	-0.111439
0.683834	0.012659	0.377622	0.024293	0.888938	-0.115966
0.666726	0.019214	0.380549	0.020671	0.906878	-0.120406
0.649630	0.025522	0.384287	0.017342	0.924019	-0.124676
0.632564	0.031565	0.388768	0.014222	0.939967	-0.128674
0.615553	0.037321	0.394005	0.011228	0.954342	-0.132299
0.598623	0.042760	0.400075	0.008282	0.966921	-0.135488
0.581809	0.047856	0.407108	0.005317	0.977705	-0.138235
0.565157	0.052574	0.415282	0.002254	0.986871	-0.140579
0.548731	0.056879	0.424797	-0.001003	0.994670	-0.142580
0.532615	0.060731	0.435839	-0.004539	0.999237	-0.143755
0.516916	0.064089	0.448502	-0.008412		
0.501766	0.066914	0.462723	-0.012595		

Appendix B

Nominal to Freestream Velocity Correlation

The "freestream" velocity needed to non-dimensionalize the data is not easily measured (or even defined for that matter) for several reasons. First, the airfoil itself changes the flow field in the entire test section in a manner dependent on the angle of attack of the system. Second, the blockage of the growing boundary layer on the tunnel walls accelerates the flow between the streamwise location of the leading edge and the streamwise location of the pitot probe even without the presence of the airfoil. The one thing that did remain almost constant was the nominal velocity set by the investigator. Therefore, a correlation was developed to convert from the nominal velocity to the freestream velocity which would be observed at the airfoil leading edge (without its presence).

The correlation was determined with an investigation of the flow using the crosswire probe in the absence of the airfoil. After calibrating the crosswire probe as described in Section 2.6, the probe was moved to the would-be streamwise location of the airfoil leading edge. Then the nominal wind tunnel velocity was varied through the entire spectrum (within the calibration range of the crosswire probe) up until the motor limitations. The data collected for both the nominal velocity and the velocity indicated by the probe is shown in Figure B-1 along with a spline fit. The dotted line represents the nominal velocity itself.

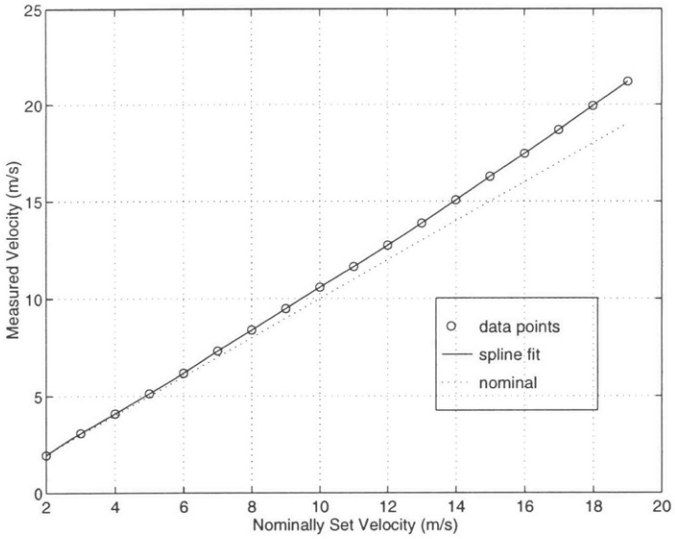

Figure B-1: Nominal to freestream velocity correlation.

The spline fit of the data is used to convert from the nominally set velocity to that which would be found at the leading edge of the airfoil. This converted velocity then becomes U_∞. Although there is an appreciable difference between the nominal velocity and that actually measured at the leading edge, the trend of the measured velocity is still more or less linear with the nominally set velocity as would be expected.

Appendix C

Velocity Data for $\Re = 1.4 \times 10^5$

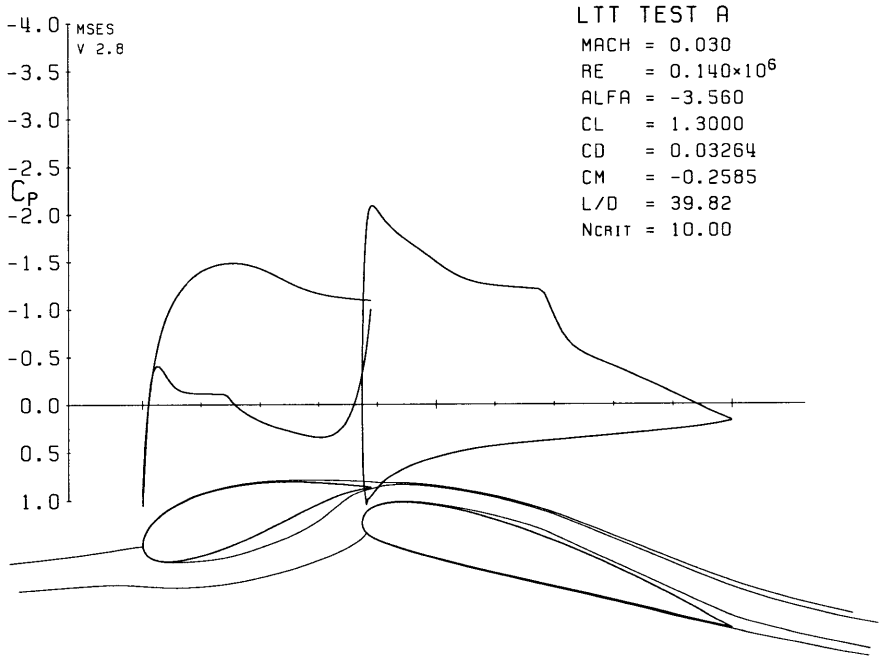

Figure C-1: Pressure coefficient and inviscid streamline ($\Re = 1.4 \times 10^5$).

x/c	0.20	0.30	0.40	0.48	0.54	0.60	0.70
β	$-3°$	$3°$	$-15°$	$6°$	$13°$	$17°$	$21°$
U_e/U_∞	1.52	1.41	1.34	1.40	1.47	1.37	1.26
δ/c	0.0071	0.0078	0.053	0.048	0.055	0.066	0.079

Table C.1: Profile location data for $\Re = 1.4 \times 10^5$.

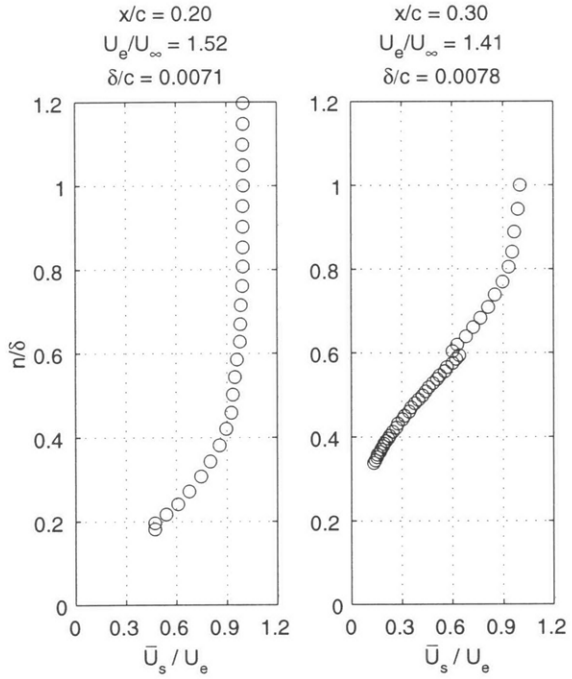

Figure C-2: Mean streamwise velocity on Element #1 ($\Re = 1.4 \times 10^5$).

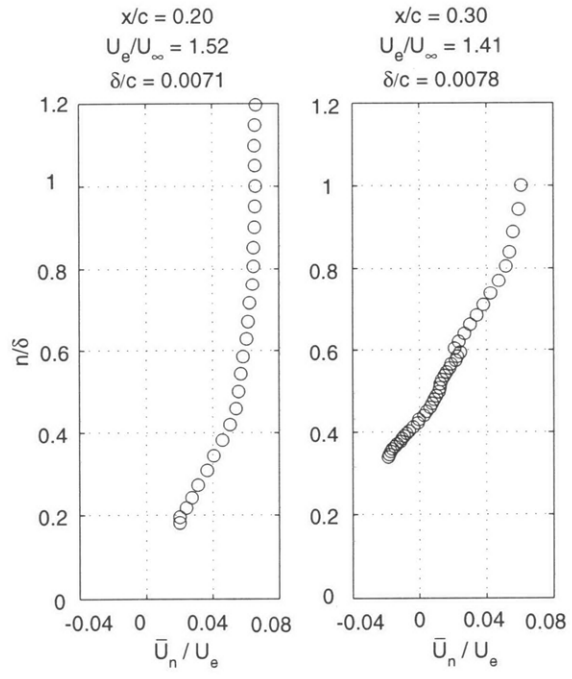

Figure C-3: Mean normal velocity on Element #1 ($\Re = 1.4 \times 10^5$).

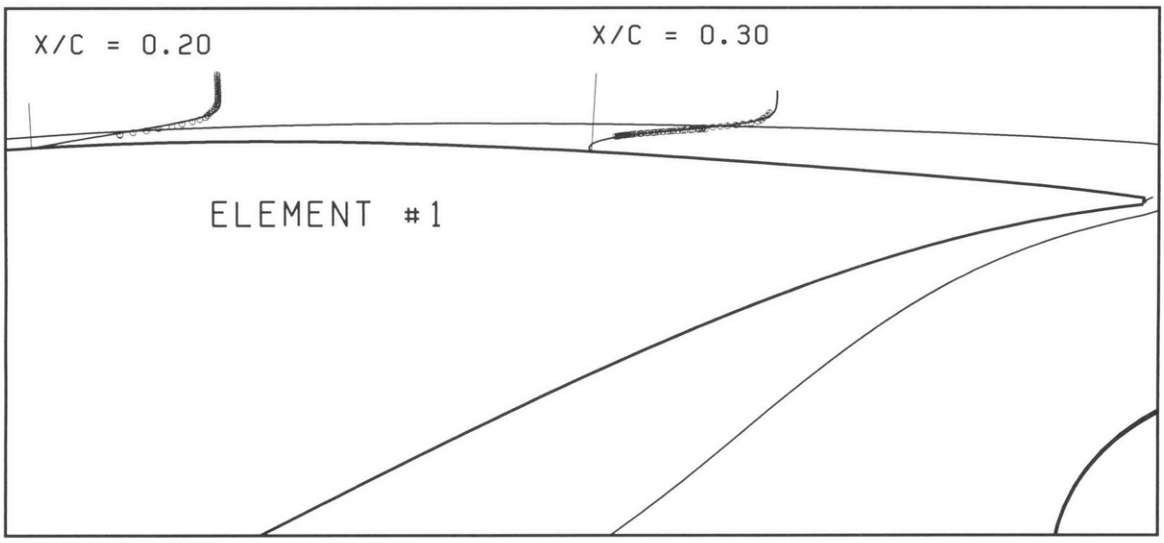

Figure C-4: Mean streamwise velocity profiles (○) on Element #1 with MSES predictions (—). ($\Re = 1.4 \times 10^5$)

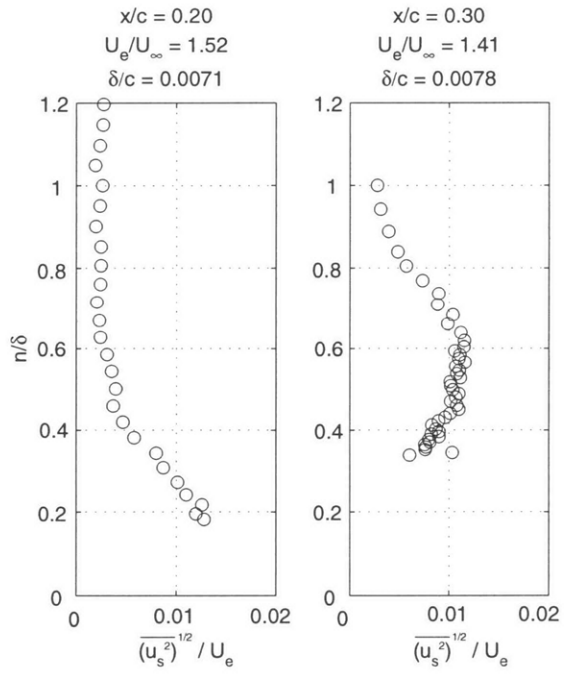

Figure C-5: RMS streamwise velocity on Element #1 ($\Re = 1.4 \times 10^5$).

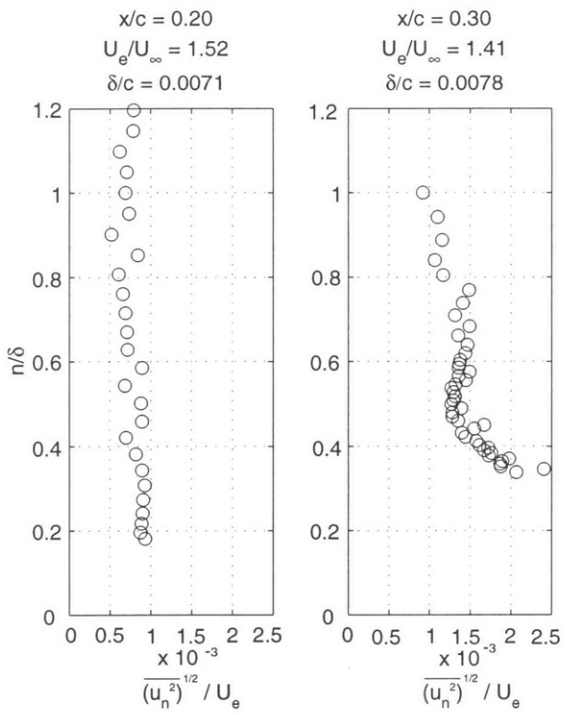

Figure C-6: RMS normal velocity on Element #1 ($\Re = 1.4 \times 10^5$).

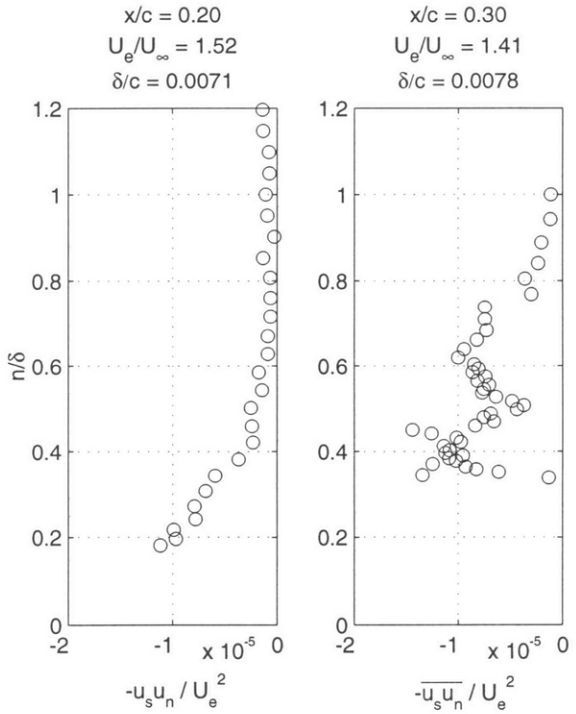

Figure C-7: Reynolds shear stress on Element #1 ($\Re = 1.4 \times 10^5$).

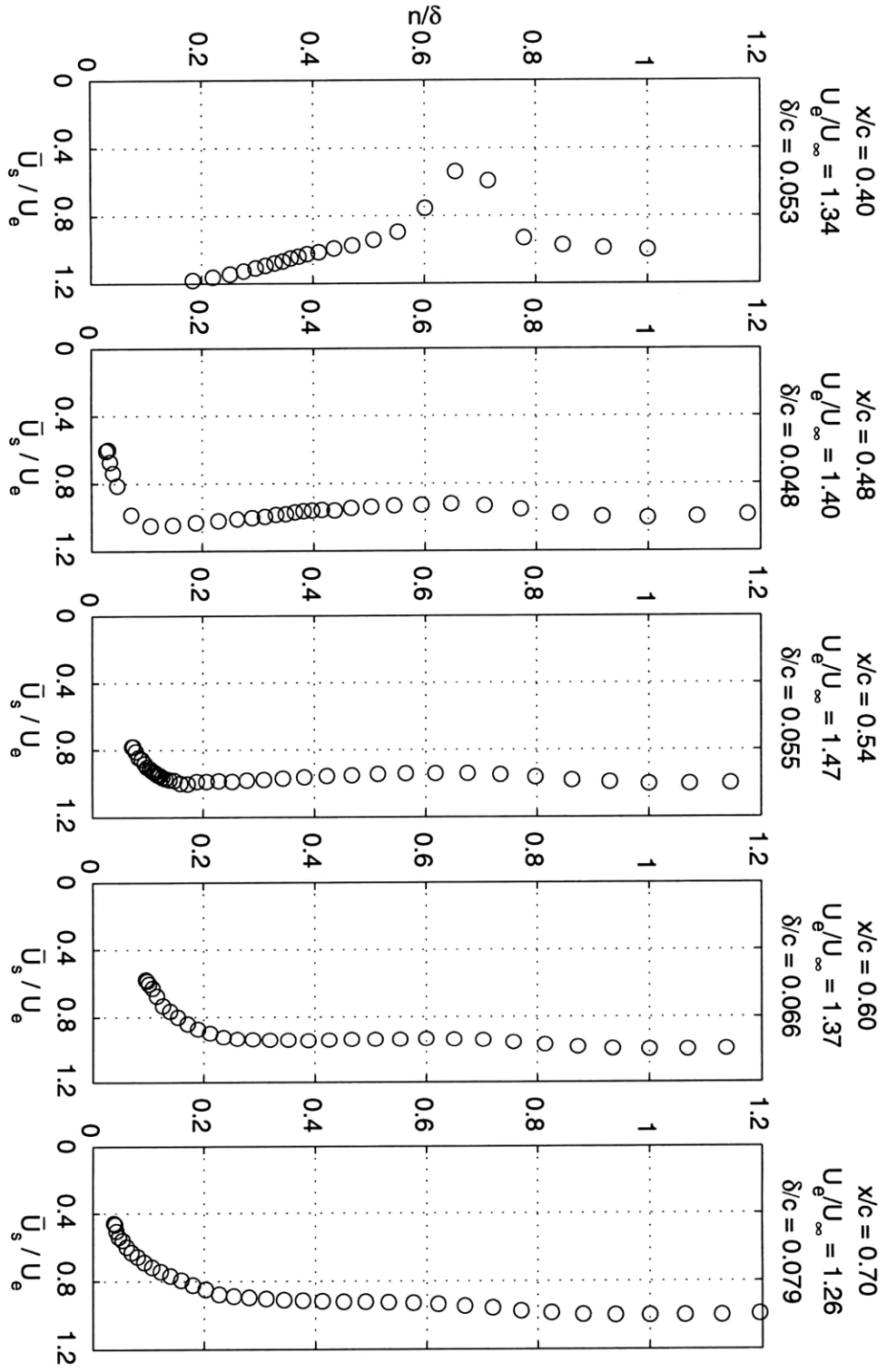

Figure C-8: Mean streamwise velocity behind Element #1 ($\Re = 1.4 \times 10^5$).

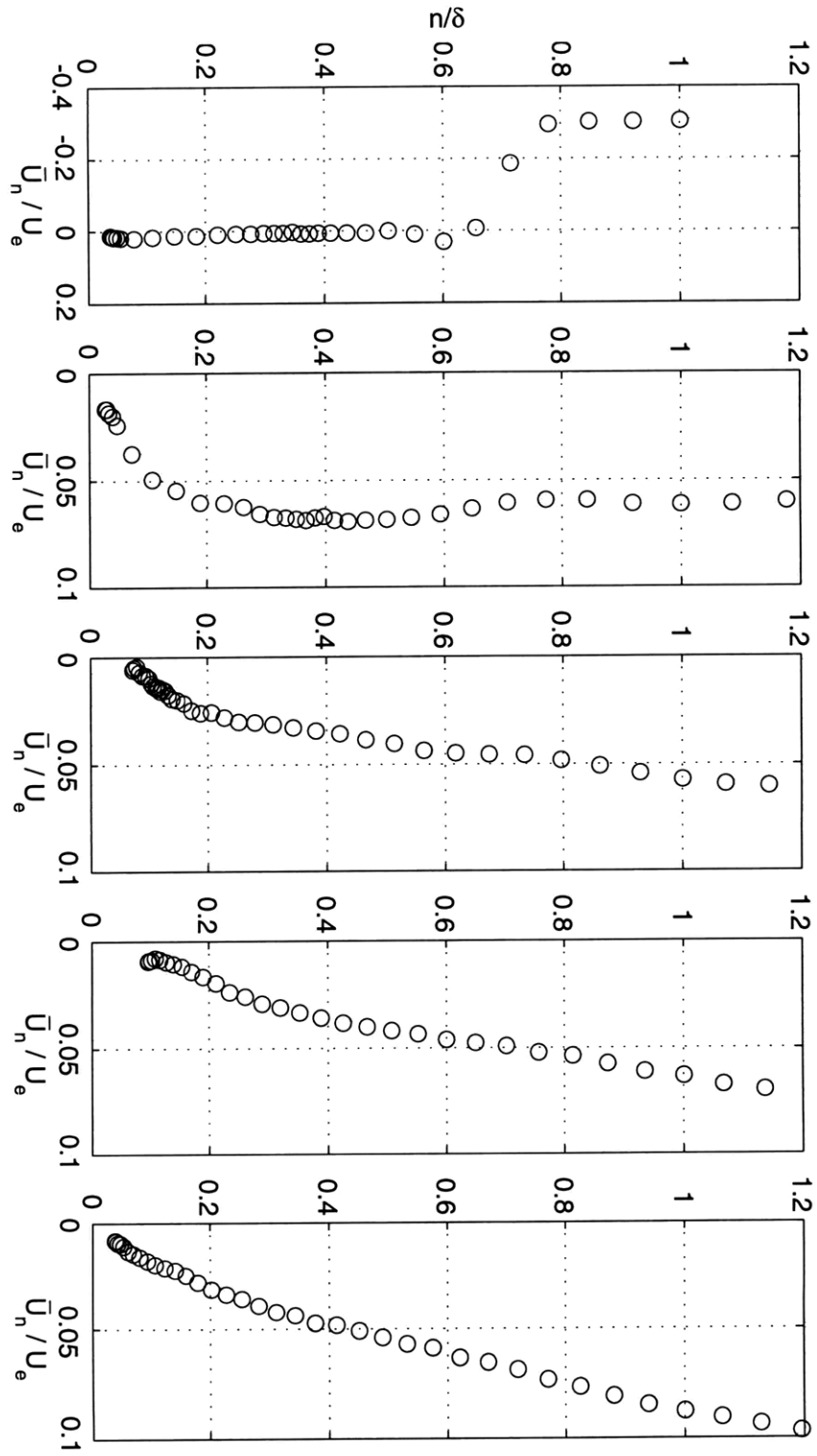

Figure C-9: Mean normal velocity behind Element #1 ($\Re = 1.4 \times 10^5$).

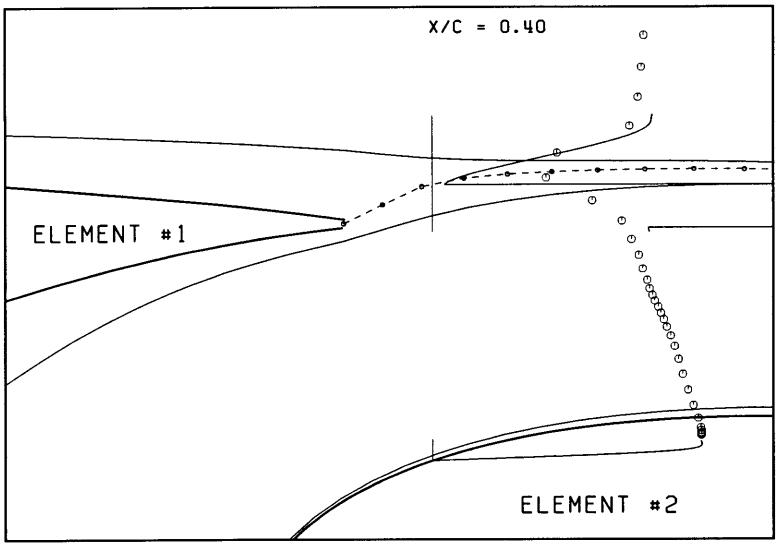

Figure C-10: Very near-wake mean streamwise velocity profile (o) behind Element #1 with MSES predictions (—). ($\Re = 1.4 \times 10^5$)

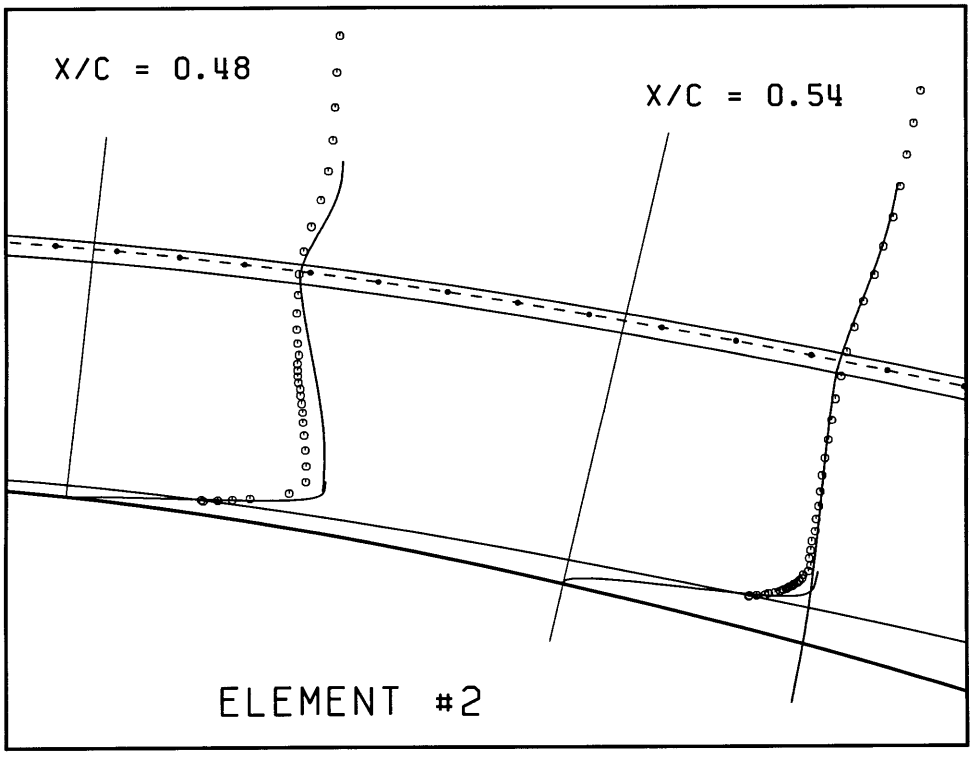

Figure C-11: Mid-wake mean streamwise velocity profiles (o) behind Element #1 with MSES predictions (—). ($\Re = 1.4 \times 10^5$)

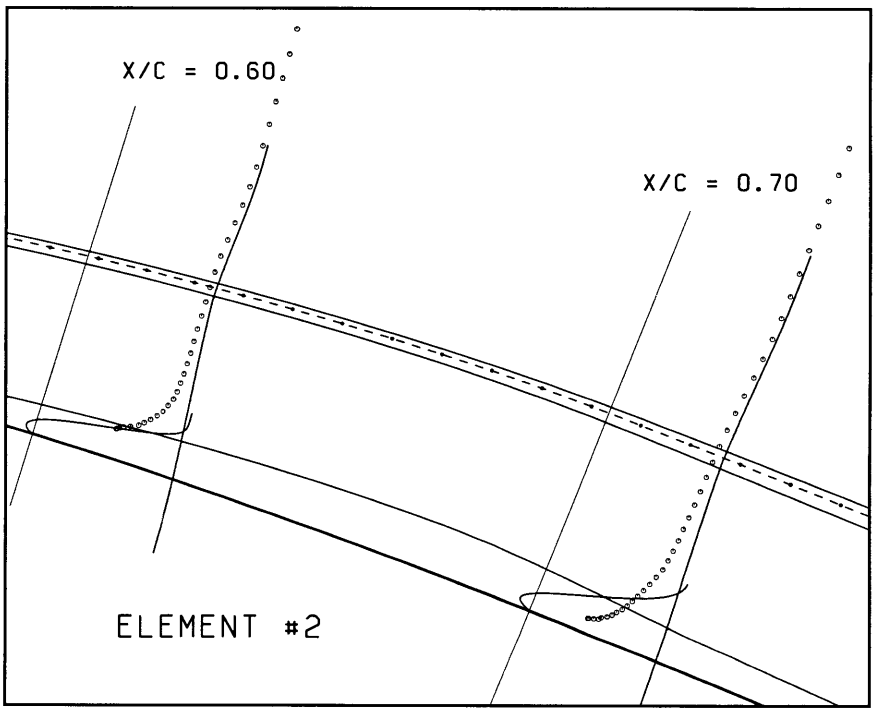

Figure C-12: Farther-wake mean streamwise velocity profiles (o) behind Element #1 with MSES predictions (—). ($\Re = 1.4 \times 10^5$)

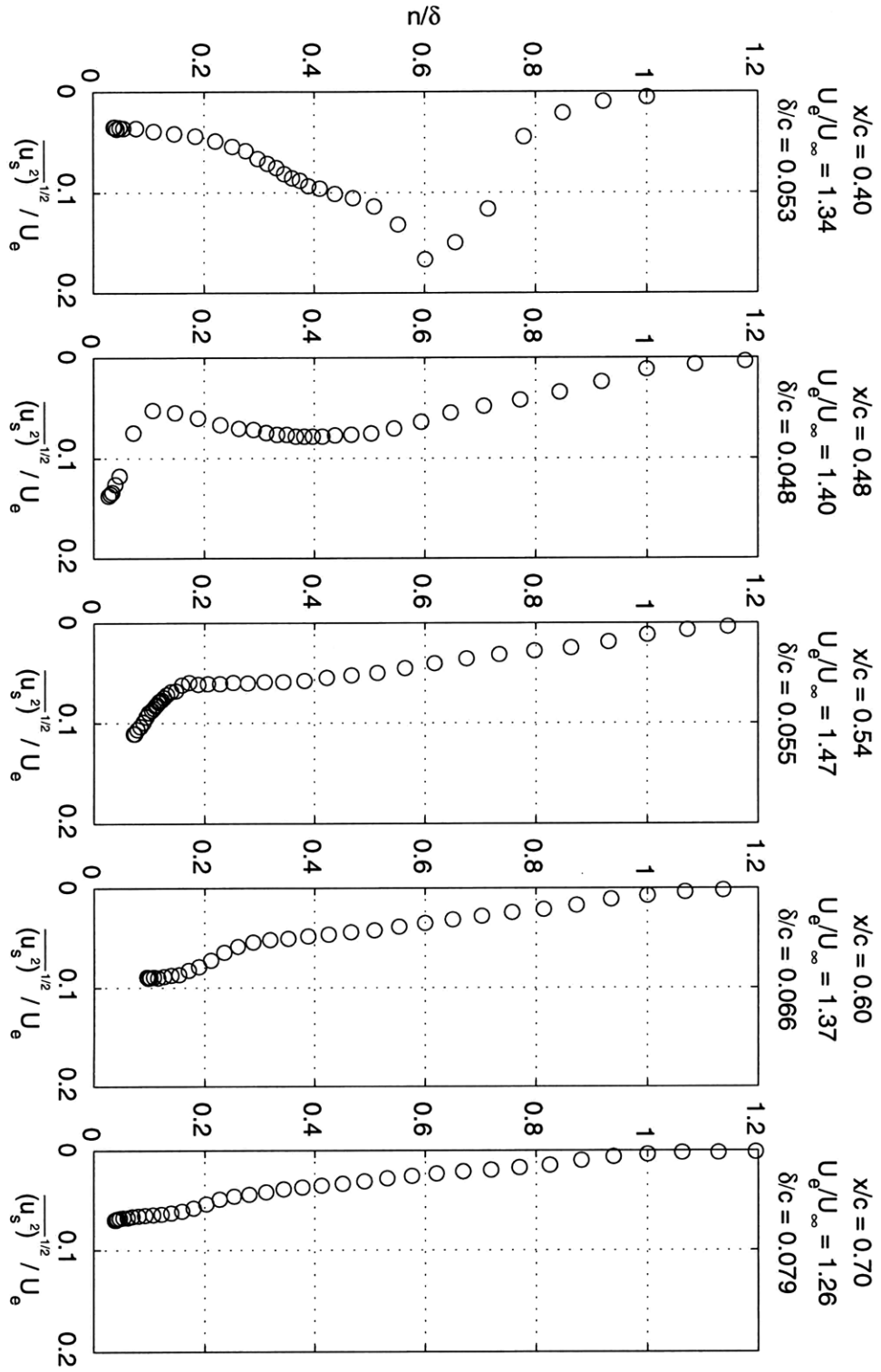

Figure C-13: RMS streamwise velocity behind Element #1 ($\Re = 1.4 \times 10^5$).

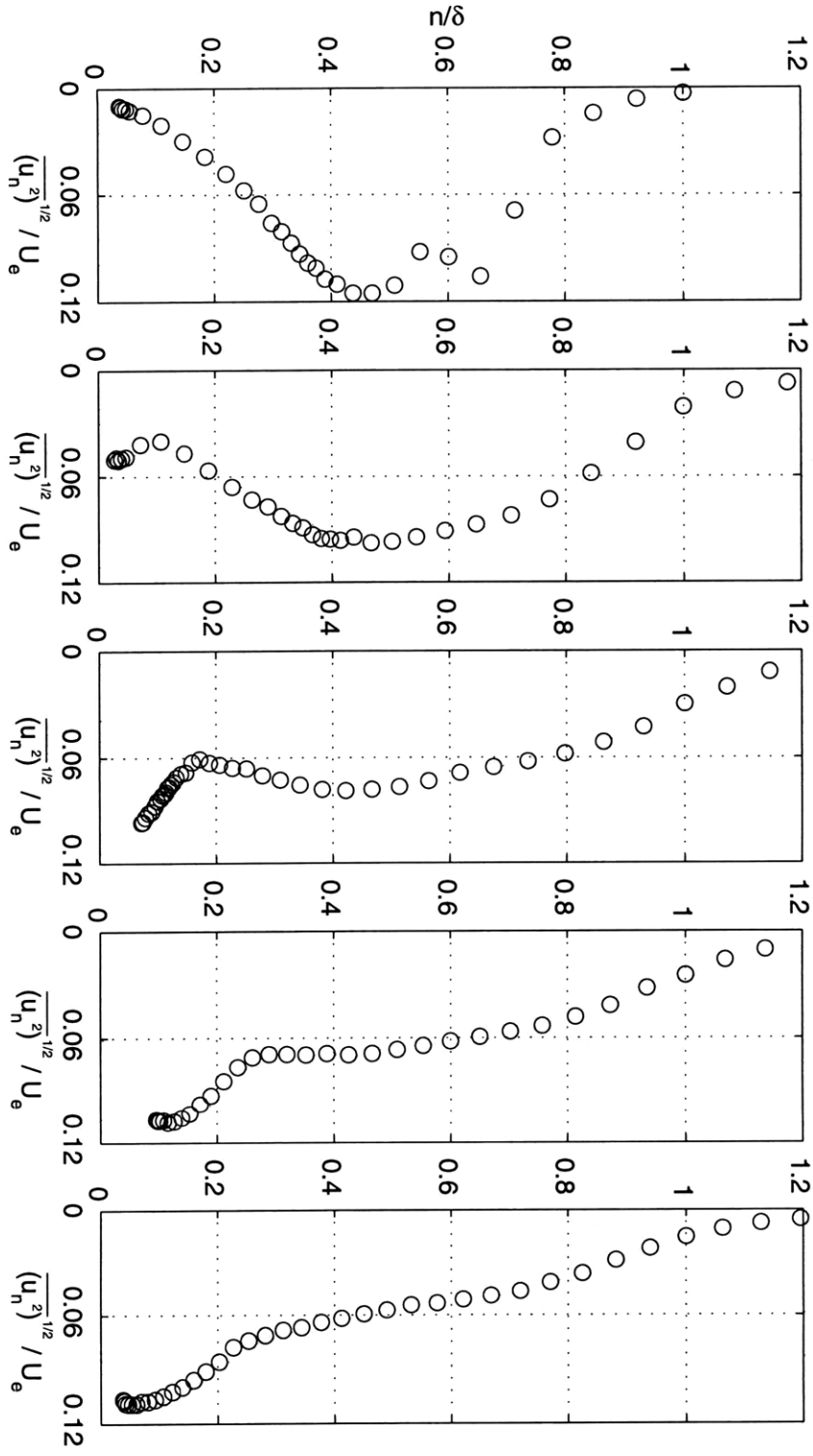

Figure C-14: RMS normal velocity behind Element #1 ($\Re = 1.4 \times 10^5$).

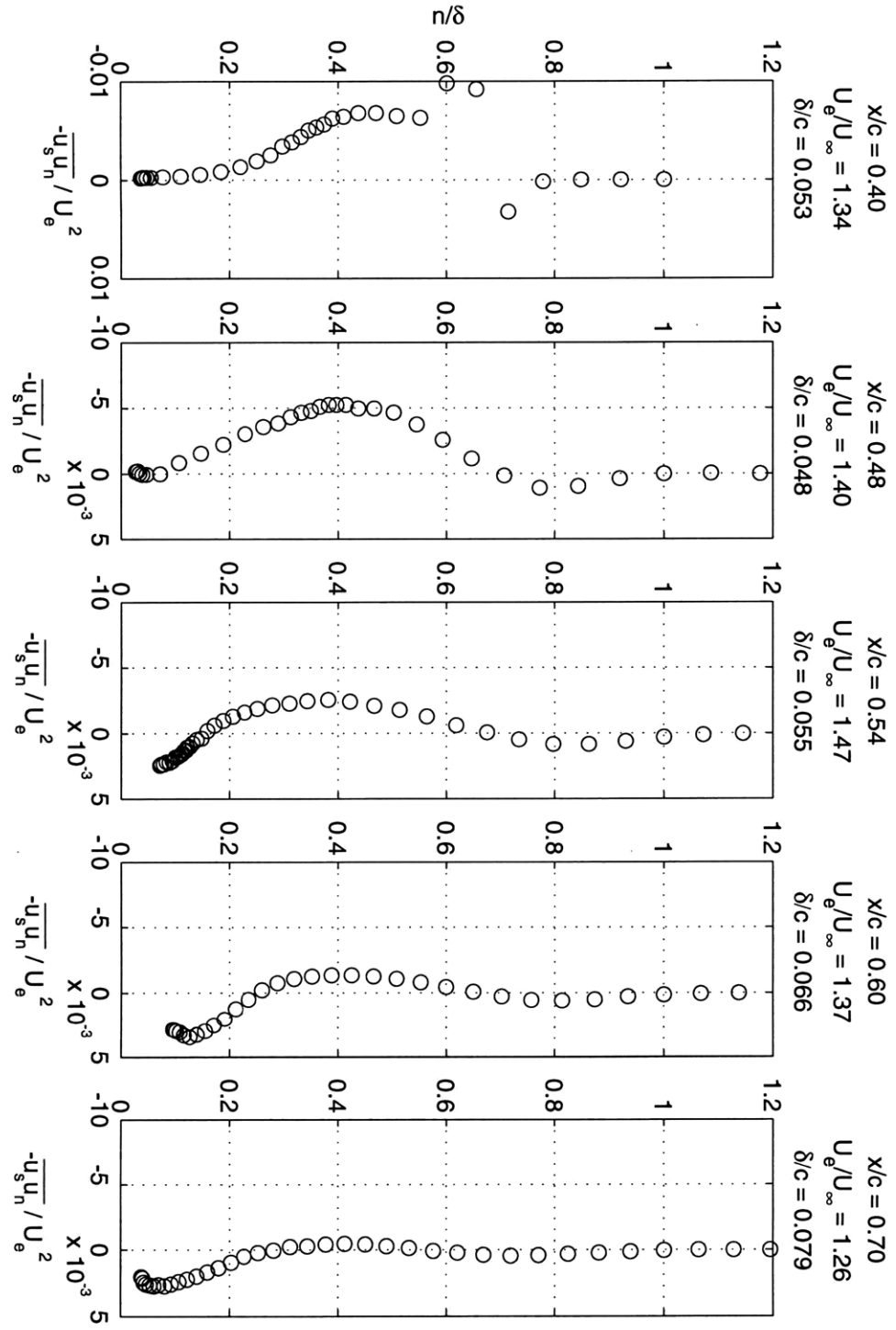

Figure C-15: Reynolds shear stress behind Element #1 ($\Re = 1.4 \times 10^5$).

x/c	0.40	0.48	0.54	0.60	0.70
U_e/U_∞	1.349	1.522	1.493	1.461	1.372

Table C.2: MSES edge velocities for $\Re = 1.4 \times 10^5$.

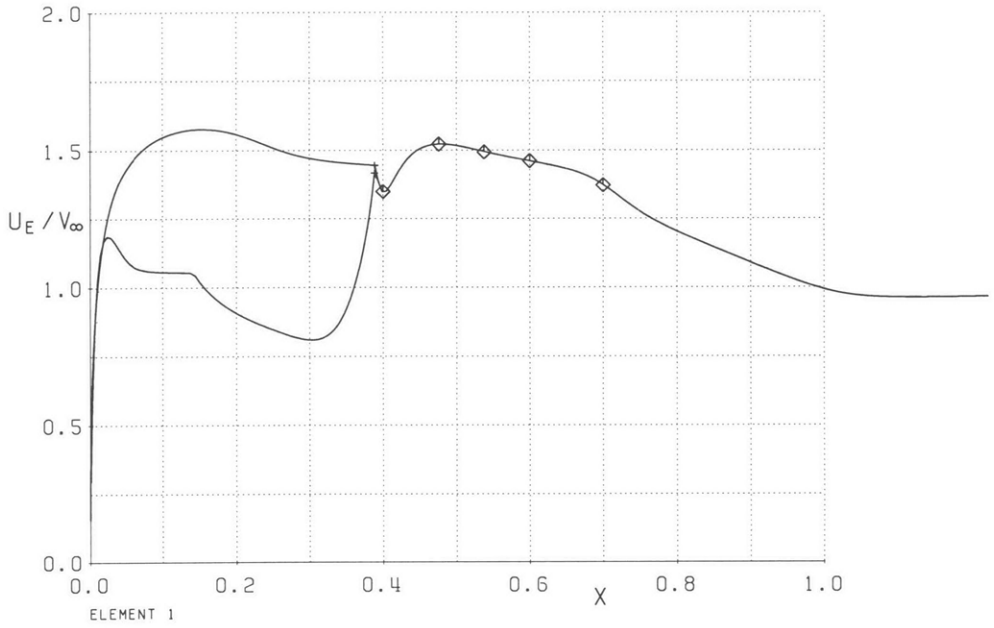

Figure C-16: MSES edge velocity in wake of Element #1 ($\Re = 1.4 \times 10^5$).

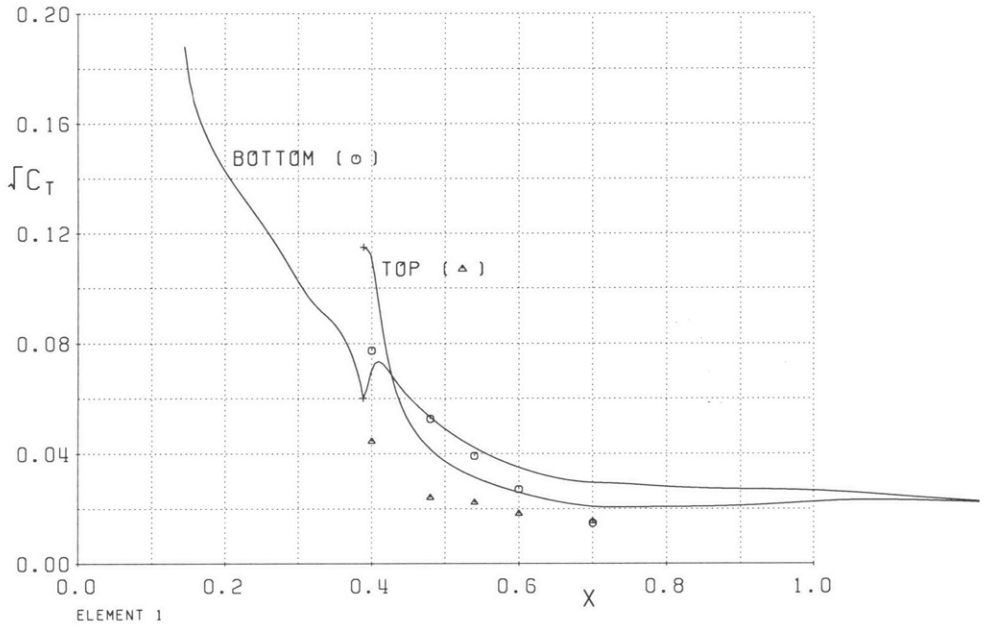

Figure C-17: Reynolds shear stress coefficient in wake of Element #1 ($\Re = 1.4 \times 10^5$).

Bibliography

[1] L.H.J. Absil and D.M. Passchier. An experimental study of the trailing edge flow of an nlr 7702 airfoil, using laser-doppler anemometry. *Experimental Thermal and Fluid Science*, 9(2):174–185, Aug 1994.

[2] D. Adair and W.C. Horne. Characteristics of merging shear layers and turbulent wakes of a multi-element airfoil. NACA TM-100053, February 1988.

[3] D. Agoropoulos and L.C. Squire. Interactions between turbulent wakes and boundary layers. *AIAA Journal*, 26(10):1194–1200, Oct 1988.

[4] P. Bradshaw. Effect of streamline curvature on turbulent flow. *AGARDograph*, 169, 1973.

[5] L.W.B. Browne, R.A. Antonia, and D.A. Shah. Selection of wires and wire spacing for x-wires. *Experiments in Fluids 6*, pages 286–288, 1988.

[6] P.G. Drazin and W.H. Reid. *Hydrodynamic Stability.* Cambridge University Press, 1993.

[7] M. Drela. Newton solution of coupled viscous/inviscid multielement airfoil flows. AIAA 21st Fluid Dyn., Plasma Dyn. and Lasers Conf., Paper AIAA-90-1470, June 1990.

[8] M. Drela. Design and optimization method for multi-element airfoils. AIAA Paper 93-0969, Feb 1993.

[9] M. Drela and M.B. Giles. Viscous-inviscid analysis of transonic and low Reynolds number airfoils. *AIAA Journal*, 25(10):1347–1355, Oct 1987.

[10] J.C. Gillis and J.P. Johnston. Turbulent boundary-layer flow and structure on a convex wall and its redevelopment on a flat plate. *Journal of Fluid Mechanics*, 135:123–153, 1983.

[11] M.E. Grimaldi. Roughness induced boundary layer transition. Master's thesis, Massachusetts Institute of Technology, 1994.

[12] J.J. Guglielmo and M.S. Selig. Spanwise variations in profile drag for airfoils at low Reynolds numbers. *Journal of Aircraft*, 33(4):699–707, 1996.

[13] P.H. Hoffmann, K.C. Muck, and P. Bradshaw. The effect of concave curvature on turbulent boundary layers. *Journal of Fluid Mechanics*, 161:371–403, 1985.

[14] L.S. Gresko Jr. Characteristcs of wall pressure and near-wall velocity in a flat plate turbulent boundary layer. Master's thesis, Massachusetts Institute of Technology, 1988.

[15] R.M. Leuptow, K.S. Breuer, and J.H. Haritonidis. Computer-aided calibration of x-probes using a look-up table. *Experiments in Fluids 6*, pages 115–118, 1988.

[16] P.T. Meredith. Viscous phenomena affecting high-lift systems and suggestions for future cfd development. In AGARD, High Lift System Aerodynamics, September 1993.

[17] K.C. Muck, P.H. Hoffmann, and P. Bradshaw. The effect of convex curvature on turbulent boundary layers. *Journal of Fluid Mechanics*, 161:347–368, 1985.

[18] R.C. Nelson, F.O. Thomas, and H.C. Chu. Experiments on the flow field physics of confluent boundary layers for high-lift systems. NASA CR-197318, 1994.

[19] V. Ramjee, E.G. Tulapurkara, and R. Rajasekar. Development of airfoil wake in a longitudinally curved stream. *AIAA Journal*, 26(8):948–953, Aug 1988.

[20] Hermann Schlichting. *Boundary Layer Theory.* McGraw-Hill Publishing Company, New York, New York, third edition, 1979.

[21] A.M.O. Smith. High-lift aerodynamics. *Journal of Aircraft*, pages 501–530, June 1975.

[22] J. Sullivan, S. Schneider, B. Campbell, G. Bucci, R. Boone, S. Torgerson, R. Erausquin, and C. Knauer. High lift aerodynamics. NASA CR-195183, March 1994.

[23] J.H. Weygandt and R.B. Mehta. Effects of initial conditions on the development of curved wakes. AIAA 31st Aerospace Sciences Meeting and Exhibit Paper AIAA-93-0655, January 1993.